POLYTECHNIQUE MONTRÉAL

affiliée à l'Université de Montréal

Development of Water-based High Barrier Coatings for Recyclable Paper Packaging Applications

EMRE VATANSEVER

Département de génie chimique

Thèse présentée en vue de l'obtention du diplôme de *Philosophiæ Doctor*

Génie chimique

Janvier 2025

POLYTECHNIQUE MONTRÉAL

affiliée à l'Université de Montréal

Cette thèse intitulée :

Development of Water-based High Barrier Coatings for Recyclable Paper Packaging Applications

présentée par **Emre VATANSEVER**

en vue de l'obtention du diplôme de *Philosophiæ Doctor*

a été dûment acceptée par le jury d'examen constitué de :

Charles DUBOIS président
Abdellah AJJI, membre et directeur de recherche
Amir SAFFAR, membre et codirecteur de recherche
Ebrahim JALALI DIL, membre
Chul B. PARK, membre externe

DEDICATION

To my beloved mother

ACKNOWLEDGEMENTS

I would like to express my sincere gratitude to Professor Abdellah Ajji for giving me the opportunity to work on this project. His invaluable guidance and support have contributed significantly to my professional growth as a researcher.

I am also sincerely grateful to Dr. Amir Saffar for his exceptional mentorship. His insights and encouragement have greatly influenced my development. I am genuinely thankful for his time and commitment to helping me succeed.

I sincerely thank my Ph.D. committee members, Professor Charles Dubois, Professor Chul B. Park, and Dr. Ebrahim Jalali Dil, for their valuable feedback and dedicated time to review my thesis.

Endless gratitude goes to amazing people in our department, Claire Cerclé and Matthieu Gautier. Thank you for helping me with so many aspects of this project. I also thank Wendell Raphael for fluorescence microscope characterizations and Olivier Sioui-Latulippe for pole figure measurements.

To my friends and colleagues in the 3S Pack Chair group, Maryam S., Maryam A., Omid, Shiva, Azadeh, Muhsin, and Tahmineh, it’s been a pleasure working with you and sharing this experience.

To the wonderful people I met in Montreal—Adam, Talwinder, Molly, Luc, Helene, Graham, Ilgin, and Nazli—you have all made my time here truly special. And a special thanks to Asli, Dogan, and Deniz, who have walked similar paths with me and made me feel understood. A big thanks to my friends from Turkey, Yagmur, Murat, Burcu, Ugur, Hakan, and Murat B. for their constant support.

Finally, I want to express my sincere thanks to my mother and sisters. Their love, care, and unwavering support have been the foundation of my success. I dedicate this work to my mother, who has always been my greatest source of happiness.

RÉSUMÉ

L'industrie de l'emballage utilise souvent le laminage multicouche, des cires, des latex, des composés fluorés ou la métallisation pour améliorer la performance barrière du papier ou des plastiques. Cependant, la plupart de ces approches ou matériaux posent des difficultés en termes de recyclabilité ; ils utilisent des ingrédients toxiques indésirables ou nécessitent des étapes de préparation sophistiquées pour la production. Les revêtements barrières à base d'eau peuvent atteindre une performance barrière élevée avec un apport minimal de matériaux, ce qui facilite le recyclage. L'objectif principal de cette thèse est de développer un revêtement à base d'eau qui améliore la performance barrière du papier tout en minimisant la perte de sa recyclabilité.

Dans le premier objectif de cette étude, nous avons cherché à synthétiser un hydroxyde double lamellaire (LDH) à haut rapport d'aspect en utilisant de la glycine aqueuse comme milieu dans une approche de traitement hydrothermal. Nous avons examiné comment les paramètres du traitement hydrothermal — température, durée et pH — influencent le rapport d'aspect du MgAl-LDH en présence de glycine. Nous avons mené des expériences à pH 6 et 9,5, à 100°C et 140°C, avec des durées de reconstruction changeantes (1, 3 et 5 jours). Nous avons constaté que ces conditions modifient la structure dans deux directions différentes : dans la direction d'empilement (direction de l'épaisseur) et dans la direction latérale (direction du planaire). En raison de son état zwitterionique à pH 6, la glycine stabilise des LDH plus fins avec un rapport d'aspect de 132 ± 35, tandis qu'un pH plus élevé entraîne plus d'empilement et un rapport d'aspect plus faible à mesure que l'état de la glycine change. L'augmentation de la température à 140°C a favorisé un empilement supplémentaire dans la direction de l'épaisseur, tandis que la prolongation du temps de reconstruction à 5 jours a réduit cet empilement, résultant en un rapport d'aspect d'environ 200. Des rapports d'aspect plus élevés dans les LDH ont considérablement amélioré les propriétés barrière des films de PET, abaissant l'OTR de 129 cc/m²·jour·atm à 0,25 cc/m²·jour·atm.

Dans la deuxième partie de cette étude, nous avons combiné le LDH synthétisé à haut rapport d'aspect avec des nanofibres de cellulose oxydées TEMPO (TCNF) dans une matrice d'alcool polyvinylique (PVA). Comme le LDH est chargé positivement, il interagit de manière électrostatique avec le TCNF, renforçant la performance barrière aux gaz en modifiant la structure du nanocomposite. Les mesures de sédimentation et de rhéologie ont montré que la combinaison de nanoparticules LDH-TCNF chargées opposées dans le PVA crée un réseau interconnecté dans

le mélange de revêtement. Cette dispersion hybride PVA-LDH-TCNF a été appliquée sur un substrat de polyéthylène téréphtalate (PET) à l'aide d'une simple méthode de revêtement à la barre. Le revêtement hybride PVA-LDH-TCNF a montré de meilleures performances barrière à l'oxygène par rapport aux revêtements PVA-LDH et PVA-TCNF. Les propriétés barrières améliorées sont principalement dues au réseau interconnecté PVA-LDH-TCNF, facilité par des interactions électrostatiques et des liaisons hydrogène, comme confirmé par FTIR. La présence de TCNF a également amélioré l'orientation (~90%), la stabilité et réduit les défauts des LDH, contribuant à la reduction de l'OTR des revêtements. Les revêtements finaux PVA-LDH-TCNF ont montré un taux de transmission d'oxygène faible de 0,04 cc/m²·jour, ce qui représente une réduction de 99,9 % par rapport au PET.

Le troisième objectif de ce projet est de développer des revêtements PVA-LDH-TCNF offrant une barrière élevée à l'oxygène et à la vapeur d'eau, tout en assurant leur recyclabilité. Nous nous concentrons sur les différentes caractéristiques que le LDH-TCNF hybride peut apporter au revêtement à base d'eau, telles que la rétention d'eau et la modification de la rhéologie. Les revêtements ont été appliqués sur du papier avec un poids de revêtement faible de 5,2 g/m² à l'aide d'un enrobeur automatique à barre intégrant un séchoir IR pour un séchage rapide. La combinaison de LDH et de TCNF dans le PVA améliore la résistance au cloquage et réduit la pénétration du revêtement dans le papier, ce qui se traduit par de meilleures propriétés barrière aux gaz. L'OTR du revêtement PVA-LDH-TCNF est mesuré à 10,1 et 31 cc/m²/jour à 0 % et 50 % d'humidité relative, respectivement. Après un traitement thermique à 130°C pendant 90 minutes, l'OTR a diminué à 9,5 cc/m²/jour à 50 % d'humidité relative, ce qui est attribué à une hydrophobicité et une cristallinité accrues. Le taux de transmission de vapeur d'eau (WVTR) a suivi une tendance similaire, avec la valeur la plus basse enregistrée à 10 g/m²·jour pour le revêtement PVA-LDH-TCNF traité thermiquement. Les tests de repulpabilité ont indiqué des taux de repulpabilité élevés de 82 % pour le PVA et 83 % pour les revêtements PVA-LC. Ces revêtements sont solubles dans l'eau et ont des poids de revêtement faibles, ce qui les rend faciles à éliminer lors du processus de repulpage. L'analyse FTIR n'a détecté aucun résidu de PVA ou de PVA-LDH dans la pâte recyclée.

Dans l'ensemble, le revêtement PVA-LDH-TCNF offre une excellente performance barrière à l'oxygène et à la vapeur d'eau avec une utilisation minimale de revêtement, ce qui en fait une option pratique et recyclable pour les applications d'emballage.

ABSTRACT

The packaging industry often uses multilayer lamination, waxes, latexes, fluorochemicals, or metallization to improve the barrier performance of paper or plastics. However, most of these approaches or materials create difficulties in recyclability; they use non-desirable toxic ingredients or require sophisticated preparation steps for production. Water-based barrier coatings can achieve a high barrier performance with minimum material input, which ensures easier recyclability. The main objective of this doctoral dissertation is to develop a water-based coating that enhances the barrier performance of paper while minimizing the loss of its recyclability.

In the first objective of this study, we aimed to synthesize a high aspect ratio of layered double hydroxide (LDH) using aqueous glycine as a medium in a hydrothermal treatment approach. We examined how hydrothermal treatment parameters—temperature, time, and pH—affect the aspect ratio of MgAl-LDH in the presence of glycine. We conducted experiments at pH 6 and 9.5, at 100°C and 140°C, with varying reconstruction times (1, 3, and 5 days). We found that changing conditions affect the structure in two directions: the stacking direction (thickness direction) and the lateral direction. Due to its zwitterionic state at pH 6, glycine stabilized thinner LDHs with an aspect ratio of 132 ± 35, while higher pH led to more stacking and a lower aspect ratio as the glycine state changed. Increasing the temperature to 140°C promoted further stacking along the thickness direction while extending the reconstruction time to 5 days reduced stacking, resulting in an aspect ratio of ~200. Higher aspect ratios in LDH significantly enhanced the barrier properties of polyethylene terephthalate (PET) film, lowering the oxygen transmission rate (OTR) from 129 cc/m^2·day·atm to 0.25 cc/m^2·day·atm.

In the second part of this study, we combined synthesized high-aspect-ratio LDH with TEMPO-oxidized cellulose nanofiber (TCNF) within a polyvinyl alcohol (PVA) matrix. Since LDH is positively charged, it interacts electrostatically with TCNF, reinforcing the gas barrier performance by altering the nanocomposite structure. Sedimentation and rheological measurements showed that combining oppositely charged LDH-TCNF nanoparticles within PVA created an interconnected network in the coating mixture. This hybrid PVA-LDH-TCNF dispersion was applied to a PET substrate using a simple bar coating method. The hybrid PVA-LDH-TCNF coating exhibited better oxygen barrier performance than PVA-LDH and PVA-TCNF coatings. The improved barrier properties were mainly due to the interlocked PVA-LDH-TCNF network, facilitated by electrostatic interactions and hydrogen bonding, as confirmed by FTIR. The presence of TCNF also led to improved orientation (~90%), enhanced stability, and reduced defects of LDH, contributing to the reduced OTR of the coatings. The final PVA-LDH-TCNF coatings demonstrated a low oxygen transmission rate of 0.04cc/m2d, which is a 99.9% reduction compared to PET.

The third objective of this project is to develop high oxygen and water vapor barrier PVA-LDH-TCNF coatings while ensuring their recyclability. We focus on the different characteristics of LDH-TCNF hybrids that can bring water-based coatings, such as water retention and rheology modification. Coatings were applied to paper at a low coating weight of 5.2 g/m² using an automatic bar coater integrated with an IR dryer for fast drying. The combination of LDH and TCNF in PVA enhances the resistance to blistering and reduces coating penetration into the paper, resulting in improved gas barrier properties. The OTR of the PVA-LDH-TCNF coating is measured at 10.1 and 31 cc/m²/day at 0% and 50% relative humidity, respectively. After thermal treatment at 130°C for 90 min, OTR reduced to 3.48 and 9.5 cc/m²/day at 0 and 50% relative humidity, respectively, attributed to increased electrostatic interactions, hydrophobicity and reduction of free volume. The water vapor transmission rate (WVTR) followed a similar trend, with the lowest value measured as 10.4 g/m²/day for the thermally treated PVA-LDH-TCNF coating. Repulpability tests indicated high repulpability rates of 82% for PVA and 83% for PVA-LC coatings. These coatings are water-soluble and have low coating weights, making them easy to remove during repulping. FTIR analysis detected no residual PVA or PVA-LDH in the recycled pulp.

Overall, the PVA-LDH-TCNF coating achieves excellent oxygen and water vapor barrier performance with minimal coating usage, making it a practical and recyclable option for packaging applications.

TABLE OF CONTENTS

LIST OF TABLES

LIST OF FIGURES

LIST OF SYMBOLS AND ABBREVIATIONS

BP	Base paper
CNF	Cellulose nanofiber
CS	Chitosan
DB	Doctor Blade
LbL	Layer by Layer
LDH	Layered double hydroxide
MMT	Montmorillonite
OTR	Oxygen Transmission Rate
PP	Oxygen Permeability
PE	Polyethylene
PEI	Polyethyleneimine
PEO	Polyethylene oxide
PVA	Polyvinyl alcohol
RH	Relative humidity
TCNF	TEMPO-CNF
TEMPO	2,2,6,6-tetramethylpiperidine-1-oxyl radical
TT	Thermal Treatment
WBBC	Water based barrier coating
WVTR	Water Vapor Transmission Rate
WVP	Water Vapor Permeability

LIST OF APPENDICES

CHAPTER 1 INTRODUCTION

Packaging is necessary to store, protect, and transport food efficiently. Due to its renewable and biodegradable features, paper is becoming more and more popular for this purpose, making up over 31% of the global packaging market [1]. However, paper alone lacks sufficient gas and liquid barriers. To improve the barrier performance, paper is laminated with plastic and aluminum foil, metalized, or coated with wax, but the recyclability of such paper packaging structures is challenging and economically unfeasible. Water-based barrier coatings (WBBC) have emerged as a more sustainable solution by improving the barrier properties of paper without compromising recyclability.

Nanoparticles are commonly used to enhance the WBBCs further, as they can create a tortuous pathway that can prolong gas diffusion. Natural nanoclays, like bentonite, are widely used but have disadvantages in high-barrier applications such as limited and non-tunable aspect ratios (diameter/thickness), sensitivity to deformation (e.g., bending, folding and curling) to applied shear, and offer poor optical properties [2, 3]. Synthetic nanoclays, like layered double hydroxides (LDH), offer advantages such as tunable aspect ratios, compositional variety, superior chemical purity, and homogeneous structure, making them ideal for high-barrier applications [2, 4]. Therefore, it is crucial to understand how to synthesize high-aspect-ratio LDHs (greater than 100) to expand their use in packaging.

The main objective of this doctoral project is to develop recyclable, high-barrier coatings for paper using high-aspect-ratio LDHs. To achieve this goal, we studied the effect of hydrothermal synthesis conditions on the aspect ratio of LDH in the presence of glycine. Due to its high dielectric constant, aqueous glycine facilitated the production of LDHs with the desired high aspect ratio in optimized hydrothermal conditions. These LDHs were then incorporated into a WBBC formulation based on polyvinyl alcohol (PVA). However, due to the strong interactions between LDH layers, the exfoliation of the LDHs in polymers, especially at higher concentrations (>10 wt.%), is challenging. We introduced a negatively charged TEMPO-oxidized cellulose nanofiber (TCNF) inside the formulation to stabilize and obtain a synergistic effect with positively charged LDH within PVA. TCNF provided multiple benefits: (i) forming a reinforcing network with LDH, improving barrier properties; (ii) enhancing the stability and orientation of LDH within PVA; (iii) acting as a rheology modifier and water retention agent; and (iv) contributing mechanical strength.

The LDH-TCNF hybrid minimized defects and prevented over-penetration into the paper, resulting in a uniform coating. Lastly, we investigated thermal treatment to improve barrier performance without compromising recyclability. Thermal treatment improved the coating by reducing porosity, increasing crystallinity, and enhancing hydrophobicity, resulting in better gas barrier properties.

This work is summarized in three submitted journal articles, and the thesis is structured as follows:

- Chapter 2 provides a literature review that explores the main themes and background information relevant to the thesis.

- Chapter 3 addresses the main and specific objectives of the research, followed by a brief explanation of how the articles are structured within the chapter.

- The key results of this study are presented in three scientific articles, included in Chapters 4, 5, and 6.

- Chapter 7 provides a critical analysis, discussing the major issues and challenges encountered during the research.

- Lastly, Chapter 8 presents the conclusions and recommendations for future work on recyclable high-barrier coatings.

CHAPTER 2 LITERATURE REVIEW

2.1 Barrier Packaging and Trends

The type of material in the food packaging industry is selected by considering different criteria such as mechanical and optical properties, processability, sustainability, and barrier properties. Materials like plastic, glass, paper, aluminum, or a combination of these are used for food packaging, each with its advantages and disadvantages. Paper and paperboard are commonly used for food packaging due to their lightweight, renewability, biodegradability, non-toxicity, and affordability. They comprise 31% of the global packaging market and are widely used in food packaging applications [1]. However, paper has insufficient oxygen and water barrier properties due to its porous and hydrophilic structures. To overcome these limitations, paper is often modified, laminated, or coated with materials like aluminum, metals, polymers, waxes, and polymer composites.

Metalized coatings/layers have achieved good barrier performance in various packaging applications [5, 6]. However, the poor adhesion between components, recyclability issues, and poor mechanical properties limit their application. Lamination (or co-extrusion) has been used extensively to produce barrier layers in paper packaging as a more straightforward and cost-effective approach. In this approach, high-barrier polymers such as ethylene-vinyl alcohol (EVOH), polyvinyl alcohol (PVA), polyvinylidene chloride (PVDC), and polyamide (PA) are widely used [5]. Although most of these polymers have an excellent barrier to oxygen gas; their barrier performance could be negatively affected when exposed to high humidity. These polymers are sandwiched between water vapor barrier films to improve the barrier performance. However, their processing is complicated, and this technique has drawbacks in terms of recyclability.

Paper sizing has also been applied to improve the barrier properties and water resistance of paper; however, limited improvements could be achieved in this direction [6, 7]. More recently, various methods like chemical grafting [8], plasma etching [9], and rapid expansion of supercritical CO_2 [9] have been proposed to improve the oxygen and water vapor barrier properties of paper; however, these methods might be uneconomical or required sophisticated steps that render them unpractical in industrial applications.

Latex-based coatings such as styrene-butadiene, styrene-butyl acrylate, and acrylate latices have been offered to improve the barrier performance of paper [10]. Most latexes are petroleum-based, non-biodegradable, and hard to recycle, and they do not exhibit good oxygen barrier performance [11]. Therefore, these drawbacks in their sustainability and oxygen gas barrier make them less preferable for paper packaging applications. Fluorochemicals are also applied to paper-based packaging to improve the water vapor barrier properties. However, these materials risk human health and the environment [12].

Nanoparticle-based coatings are also a practical approach to improve the barrier performance of packaging systems. High aspect ratio nanoparticles can increase the diffusion pathway of gas molecules, enhancing the barrier properties of packaging. Nanoparticles like nanoclays, nanocelluloses, or carbonaceous are less toxic, relatively cheap, and have superior mechanical and barrier properties, which render them suitable for food packaging applications. Dispersion or exfoliation/intercalation of these nanoparticles are the most important criteria that determine the final properties of packaging. A detailed literature review on the use of nanoparticles will be given in the following chapters of this research proposal.

Approaches such as layer-by-layer or hybrid coatings have attracted considerable attention as these approaches could quickly obtain a thinner structure with superior barrier properties. These methods include utilizing oppositely charged components that ensure the formation of electrostatic interactions. Besides electrostatic interactions, hydrogen and covalent bonding and charge transfer interactions can take place in these systems [13]. These coatings can have a higher barrier performance than conventional metal or mineral oxide coatings as a higher amount of nanoparticles can be used. A more detailed literature review will be given in the following sections.

Water-based barrier coatings are becoming more popular as they provide good barrier properties with very low coating weight, use non-volatile organic materials, and are easily removed from the substrate. New formulations based on biopolymers and nanoparticles are also becoming more popular. A detailed review of this coating is also given in the following chapters.

2.2 Gas Barrier: Theory, Definitions and Influencing Factors

Controlling the amount of oxygen or water vapor inside the package is crucial to extend the shelf life of the food product. To improve the barrier performance of the package, one must understand the theory behind it. In the barrier film/coating, penetration of gas molecules through the homogeneous nonporous material can be divided into three stages (Figure 2.1):

- sorption of the gas molecules at one side of the film surface
- diffusion through the film due to a concentration gradient
- desorption penetrant from the other side of the film

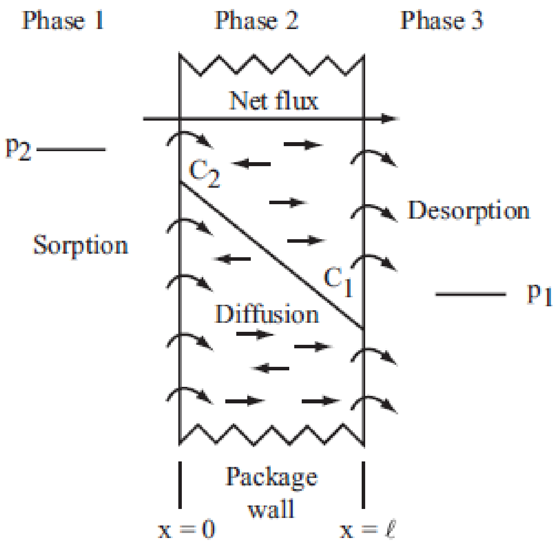

Figure 2.1 Sorption, diffusion, and desorption across the barrier film/coating [14]

The relationship between the concentration gradient and the rate of permeation can be expressed by Fick's first law:

$$J = -D\frac{\delta c}{\delta x} \tag{2.1}$$

Where J is the transfer rate per unit area, D is the diffusion coefficient, C is the concentration of diffusing substance, and x is the distance measured normal to the section. Under steady-state conditions, J became constant, and the equation can be integrated from x = 0 to x = L, and between the penetrant concentrations $c = c_2$ (at x=0) and $c = c_1$ (at x = L) and assuming D is constant and independent of concentration, the equation could be written as;

$$J = -D\frac{\delta c}{\delta x} = D\,\frac{c_2 - c_1}{l} \tag{2.2}$$

However, in barrier measurements, measuring the partial pressure in the gas phase surrounding the film is easier than measuring the penetrant concentration. Therefore, Henry's law (c= Sp) can be applied -if the concentration is low enough- and the equation can be rewritten as:

$$J = DS\,\frac{p_2 - p_1}{l} \tag{2.3}$$

At a steady-state, gas molecules can diffuse through a polymer film at a constant rate if the pressure difference along the polymer is kept constant. The diffusive flux of a permeant in the polymer can be defined as the quantity of permeant (Q) passing through a unit area A in a time t.

$$J = \frac{q}{At} \tag{2.4}$$

Rearranging Equations 2.3 and 2.4 gives us

$$DS = \frac{ql}{At\Delta p} \tag{2.5}$$

The diffusion coefficient is associated with kinetics or the mobility of the gas molecules in the matrix[15, 16]. On the other hand, the soluble coefficient is a thermodynamic factor, and the affinity between the diffusing molecules and the packaging material determines this factor.

Many factors, such as crystallinity, accessible volume, pore size, the hydrophilicity of the polymer, and temperature, pressure, and relative humidity of the environment, can affect the penetrant motion within the polymer package/film [17]. For instance, the presence of crystalline regions in the polymer matrix hinders the diffusion of gasses as the crystalline regions are assumed to be impermeable to gases, so sorption and diffusion take place mainly in the amorphous phase of the polymer matrix [18]. Crystals can also change the segmental mobility of neighbor chains and decrease the gas diffusivity in that part of the polymer, known as the chain immobilization effect.

On the other hand, temperature affects the free volume or mobility of the polymer chains. Higher temperatures could cause easier permeation of the penetrant. The size and polarity of the penetrant are other factors that can affect the ability of the penetrant molecule to permeate through the plastic film. Moreover, molecular orientation and architecture (branching, molecular weight, and tacticity), the presence of fillers, and their content significantly affect barrier properties as they could affect the segmental mobility and free volume of polymeric systems [17].

Permeance, permeability, and gas transmission rates are important parameters/descriptions in barrier packaging. The gas transmission rate can be defined as the weight or volume of permeant (e.g., water vapor or oxygen) passing through the film per unit area and time. *Permeance* is the transmission rate divided by the partial pressure difference of the permeant across the film. *Permeability* is the permeance multiplied by the thickness, as shown in Table 2.1. These parameters can be converted into each other if test conditions and film thickness are known.

Table 2.1 Barrier parameters, equation, and units

Barrier Property	**Equation**	**Unit**
Water Vapor Transmission Rate (WVTR)	$\text{WVTR} = \frac{weight\ passed\ through}{area \times time}$	$g/m^{2}\cdot day$
Water Vapor Permeability (WVP)	$\text{WVP} = \frac{WVTR \times thickness}{satturated\ pressure \times \Delta\%RH}$	$g\cdot \mu m/m^{2}\cdot day\cdot kPa$
Oxygen Transmission Rate (OTR)	$\text{OTR} = \frac{volume\ passed\ through}{area \times time}$	$cm^{3}/m^{2}\cdot day$
Oxygen Permeability (OP)	$\text{OP} = \frac{OTR \times thickness}{oxygen\ partial\ pressure\ diff.}$	$cm^{3}\cdot \mu m/m^{2}\cdot day\cdot atm$

We categorized the barrier performance of films/coatings into poor, low, medium, high, and very high barrier films. Table 2.2 shows the examples, and the barrier performance range attributed to each polymer film/coating grade. A good barrier toward oxygen does not necessarily mean good moisture barrier performance. Oxygen permeability is mostly required for a structure with polar-polar interactions or hydrogen bonding. This leads to high hydrophilicity that causes poor water vapor barrier properties. Although chemistry has a more pronounced effect on permeability, morphology can also play a determining role in controlling the gas and water vapor permeation.

Table 2.2 Classification of barrier performance and examples [13]

Grade	**OP ($cm^{3}\cdot$ µm /m^{2} day. atm)**	**Example**	**WVP (g· µm /m^{2} day . kPa)**	**Example**
Poor	>40000	HDPE, PP, PS, PHB	>3000	Silicone elastomer
Low	4000-40000	PVC, BOPP, PHA, PLA	1000-3000	PA 6, PLA
Medium	40-4000	EVOH, OPET, PA6 PET	400-1000	PS, PHA
High	40-400	PVdC, PA6 449	40-400	PAN, PVC, PET
Very high	<40	EVOH 393	<40	HDPE, PP, PVdC, OPET, BOPP

HDPE: high-density polyethylene, PP: polypropylene, PS: polystyrene, PHB: polyhydroxybutyrate, PVC: polyvinylchloride, BOPP: biaxially oriented polypropylene, PHA: polyhydroxyalkanoates, PLA: polylactide, EVOH: ethylene vinyl alcohol, OPET: oriented polyethylene terephthalate, PVdC: polyvinylidene chloride

2.3 High Barrier Films and Coatings

Several methods are used to deposit polymer coatings on a substrate, such as roll-to-roll, dip, spin, spray coating, and doctor blading. All these approaches enable the deposition of coating solution after solvent evaporation. One of the most used in research, dip coating, involves dipping (and then pulling) the substrate into the polymeric solution at a certain speed. This technique can precisely control process parameters such as dipping time, pH, and temperature [19]. However, there are difficulties in the large-scale application of this method. Spin coating is another approach that is used in high-barrier coatings. This approach rotates the substrate while different polymer-based solutions can be deposited onto the surface. Rotation can allow the formation of very thin films with the perfect alignment of nanoparticles. This technique is faster than dip coating, and the precise film thickness can be obtained easily. Spray coating is also used in academia and industry in high-barrier coating applications. This technique can easily obtain high barrier performance with low coating weights. However, uniform deposition could be a challenge in this approach. Doctor blading and roll-to-roll coatings are other approaches with larger applications in the industry. In a former approach, the coating solution is spread on a substrate using a blade at a constant speed. The thickness of the coating or film can be tailored by adjusting the distance between the blade and the roll. Shear stress induced by a doctor blade leads to a high level of orientation in this approach. However, this coating approach has little waste and can be used at the industrial level. In the roll-to-roll coating process, the substrate moves with the help of a conveying belt. The coating solution coming from the nip is passed through the rolls, namely, the application roll and metering rolls, and then the substrate is coated. This approach is continuous, unlike the other coating techniques; therefore, it is widely used in industry. The velocity of the web, temperature, and the gap between the slot die and slot die geometry are important parameters that affect the final structure of the coatings [20]. For all coating approaches, the rheological properties of the solution are decisive. Drying approaches are also dictating the final properties, such as coating/film thickness and coating weight. Table 2.3 summarizes the recent studies on high barrier films and coatings, including the type of coating method, sample, nanoparticle content, coating weight or film thickness, OTR and OP, and reduced permeability (P/P_0) reported. Among nanoparticles, the use of graphene oxide (GO), nanoclays, nanocelluloses, and boron nitride results in a remarkable improvement in OTR and OP values. For example, Huang et al. [21] showed that the use of GO in polyvinyl alcohol (PVA) led to a decrease in OP and WVP coefficient by about 98% and 68% at a low GO loading of 0.72 vol%. This improvement was attributed to uniform GO dispersion, high-level GO exfoliation, and alignment of GO within the polymer matrix. Unalan et al. [22] reported that OP of pullulan was reduced from 6337 cc·µm·m^{-2} d^{-1} atm^{-1} to 1357 cc·µm·m^{-2} d^{-1} atm^{-1} with 0.3wt% loading. This improvement was also ascribed to a high level of dispersion and alignment of GO as in the previous study.

Nanocellulose materials such as cellulose nanofiber (CNF) and cellulose nanocrystals (CNC) have also been used in high-barrier films or coating preparation [23-26]. Biobased and biodegradable properties, comparable mechanical and optical properties, high crystallinity, and natural abundance make them potential candidates for several applications. For instance, one of the pioneering studies in the field, Fukuzumi et al. [27] showed that upon oxidation of CNF by a 2,2,6,6-tetramethylpiperidine-1-oxyl radical (TEMPO) high barrier coating can be obtained. They reported that the oxygen permeability of PLA reduced from 746 ml·m^{-2}·day^{-1}Pa^{-1} to 1 ml·m^{-2}·day^{-1}Pa^{-1} for PLA film coated with CNF layer. However, difficulties in processing due to thermal degradation are still significant issues in nanocelluloses based high-barrier applications.

In the literature, layered nanoclays have been highlighted as having a strong gas barrier performance as their rigid structures do not allow the diffusion of small gas molecules [28-33]. These nanomaterials can be obtained from natural substances like montmorillonite and smectites or can be synthesized using substances like fluorohectorite, fluoromica, and metal oxides [34]. Natural nanoclays generally have a layer thickness of around 1 nm and an aspect ratio of 10 to 200-300 [2, 3]. On the other hand, synthetic nanoclays can have a high aspect ratio of 20,000. To benefit from these high aspect ratios, intercalation/exfoliation of nanoclays in the polymer matrix is crucial. For instance, Yu et al. [35] showed that after exfoliation or delamination of LDH using formamide, OTR and WVTR of PET and PLA can be improved. In another study, Fatma et al. [15] showed that a poor level of MMT exfoliation because of the use of a high concentration of nanoparticles caused a reduction in the OTR of PVA/MMT-coated PET substrate. Therefore, determining the exact concentration of nanoclay solution is decisive in the final properties. To increase the exfoliation of nanoclays, different approaches have been used, such as ultrasonic treatment [36, 37], surfactant and/or plasticizers [38-40], oppositely charged nanoparticles [41], and solutions such as toluene [40].

Besides the type of nanoparticles, orientation, coating approach, and thermal annealing, additives can also significantly affect the microstructure of barrier coatings/films. For instance, a high level of orientation of either nanoparticles or polymer chains can also enhance the gas barrier properties of coating and films as the highly aligned structures extend the gas pathway through the film. Wang et al. [42] showed that in LDH/carboxymethyl cellulose sodium coatings that are prepared layer-by-layer technique, the orientation of LDHs plays a key role in the decrease of the gas transmission rate of films. In another study, Huang et al. [21] also showed that upon the alignment of graphene oxide nanosheets within the PVA matrix, the diffusion coefficient could be reduced remarkably due to the increasing tortuous path.

Depending on the coating technique chosen, the properties of the film vary. Char et al. [43] compared the morphology and wettability of dip-coated (DC) and spin-coated (SC) layer-by-layer assembly coatings. They showed the roughness is lower while the orientation is higher in SC films than in DC films. As a result, SC improved the gas barrier properties of films more efficiently [43]. Besides improving barrier properties, they reported that the SC approach is much faster than the DC approach. In another study, Fatma et al. [15] showed that PVA/MMT films prepared through doctor blading have better surface homogeneity than their dip-coated counterparts.

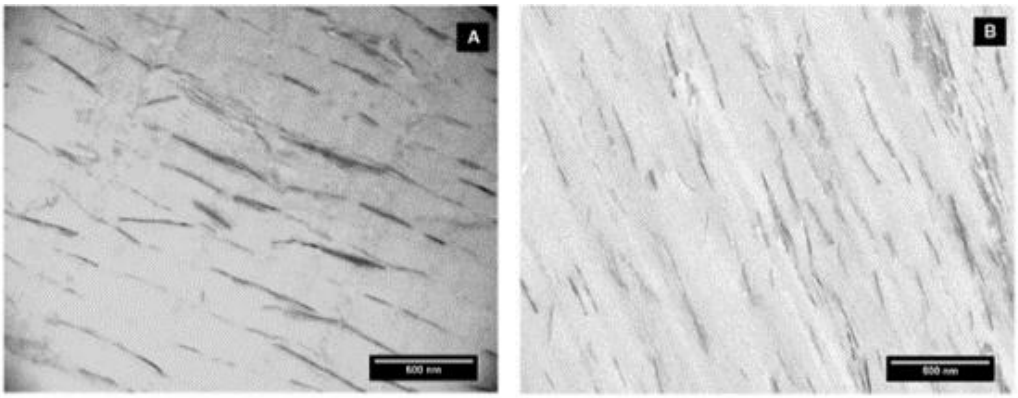

Figure 2.2 TEM images of nanocomposite films prepared by (a) dipping-LbL and (b) spray spinning-LbL [43]

Thermal annealing is another key factor that influences the barrier performance of films. Kim et al. [44] indicated that hot pressing of LbL assembly of cellulose nanowhisker and chitin can improve the barrier properties due to the formation of amide bonds between components. Ren et al. [45] also reported that upon hot pressing at 65 ˚C extremely compact and highly oriented GO/CNF nanocomposite films can be achieved. In another study [46], thermal annealing for 2h at

140 ˚C improved the OTR and WVTR of CNC-CNF coatings due to the hornification. Sharma et al. [47], confirmed these results, in which a similar thermal treatment is applied to improve the OTR and WVTR of CNF films. They showed that upon thermal treatment at 175 ˚C for 3h, OP and WVP decrease by 25 and two-fold, respectively. These improvements were attributed to (i) a reduction in interfibrillar space or porosity (ii) an increase in crystallinity, and (iii) an increase in hydrophobicity due to hornification.

The use of secondary nanoparticles has recently emerged as a new approach to developing barrier coatings/films. Oppositely charged materials lead to synergistically reinforced nanocomposite films/coatings. This originated from the improvement of delamination/exfoliation of nanoparticles and a high level of electrostatic interactions. The details of these approaches will be given in the following sections.

Table 2.3 Various studies have attempted to improve oxygen barrier properties in the literature

Sample	NP content	Method	Thickness (µm)	OTR (cc/(m2 day)) Or OP (cm^3 cm / (cm^2 day Pa)) At %50 RH	P/P_0	Year	Ref
Cellulose/GO	1.64 vol%	SC + HP	90	8.64× 10^{-12} cm^{3}cm /(cm^2 day Pa)	0.1	2014	[48]
PLA/GO	0.0034 vol %	SC + HP	500	2.25 × 10^{-10} cm^{3}cm/(cm^2 day Pa)	0.042	2020	[49]
PLA/Chitosan-MMT	0.2wt%*70 layer	LbL	0.4	6.35 × 10^{-11}cm^{3}cm /(cm^2 day Pa)	0.037	2012	[32]
PVA-GO	0.72 vol%	SC	-	2.07 × 10^{-11} cm^{3}cm/(cm^2 day Pa)	0.0113	2012	[21]
PVA-Starch-HNT	5 wt%	SC	125	7.2 × 10^{-5} cm^3 cm / (cm^2 day Pa)	0.24	2019	[50]
PVA-CNF-Clay	5 wt%	SC	-	4.9× 10^{-13} cm^{3}cm/(cm^2 day Pa)	0.0125	2014	[25]
PLA-rGO-PVP	0,65 mg/mL	LbL	110	2.27 × 10^{-7} cm^3 cm / (cm^2 day Pa)	0.0104	2016	[51]
CNF-GO	0.72 vol%	LbL + HP	30–40	1.45 × 10^{-10} cm^3 cm / (cm^2 day Pa)	0.00025	2019	[24]
PET/Chitosan-CNF	0.1wt%* 40 layer	LbL	7	1.6 cc/(m^2 day)	0.0026	2021	[52]
PET/PVA-LDH	3wt%	RC	1.2	<0.005 cc/(m^2 day)	0.0038	2020	[33]
PET/PVA-GO	0.07vol %	SC+anneal	-	0.0054 cc/(m^2 day)	<0.06	2014	[53]
Pullulan-GO	0.01 vol%	SC	30	70 cc/(m^2 day)	0.26	2015	[22]
PTPu;lulan_GO	1.5 wt%	RC	12.8	22.3 cc/(m^2 day)	0.2	2016	[54]
CNF-boron nitride	0.5 wt%	SC	-	4.7 cc/(m^2 day)	0.235	2018	[23]
PVA-Boric acid	5 wt%	SC	60	0.15 cc/(m^2 day)	0.025	2015	[55]
PET/PVA-saponite	7 wt%	SC	12	1.67 cc/(m^2 day)	0.3	2006	[56]
Paper/Starch-MMT	3.1 wt%	Lamination	-	70 cc/(m^2 day)	-	2014	[30]
PET/PEI-GO	0.2wt%* 10 layer	LbL	0.050	0.12 cc/(m^2 day)(%0 RH)	0.014	2013	[57]
CA-LDH	0.3wt%*20 layer	Spin-LbL	20	<0.005 cc/(m^2 day)	0.00005	2013	[28]
PET/PAA-LDH	0.1wr%*15 layer	LbL	0.15	<0.005 cc/(m^2 day)	0.00059	2015	[58]
PET/PVA-MMT	25 vol%	LbL	-	0.00142 cc/(m^2 day)	0.0064	2019	[16]
PET/CNF-Chitin	20 BL	Spray-Lbl+HP	2.62	0.48 cc/(m^2 day)	0.012	2019	[44]

SC: solution casting, HP: Hot press, LbL: Layer-by-layer assembly, RC: Rod coating, GO: graphene oxide, PLA: polylactide, MMT: montromonolite, PVA: polyvinyl alcohol, HNT: halloysite nanotubes, CNF: cellulose nanofiber, rGO: reduced graphene oxide, PVP: polyvinylpyrrolidone, CA: cellulose acetate PET: polyethylene terephthalate, LDH: layered double hydroxide, PDDA: polydiallydimethylammonium chloride, PEN: polyethylene naphthalate, PEI: polyethylenimine, PAA: polyacrylic acid

2.4 Permeability Models

Fick's diffusion model is insufficient to explain the diffusion of gases in composites as these materials have heterogeneous structures, and diffusion occurs differently through the material. To model the diffusion behavior of the nanocomposites, the polymer matrix is considered a permeable phase, and the nanoparticle is assumed to be an impermeable phase. This behavior is illustrated in Figure 2.3. Nanoparticles force gas molecules to diffuse through the polymer in a tortuous pathway, leading to a decrease in permeability. Different models explain the diffusion behavior of gases in polymers in the presence of nanoparticles with various assumptions.

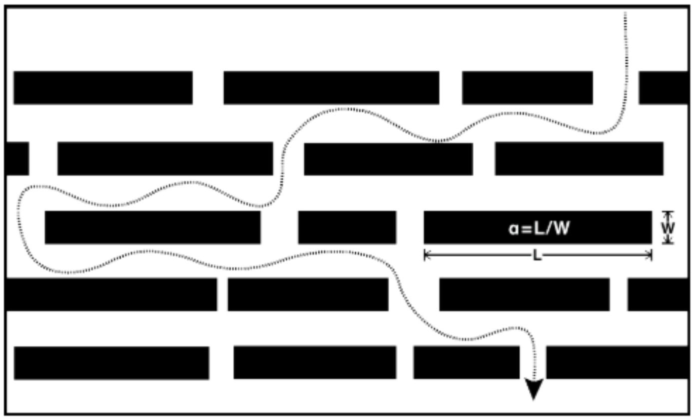

Figure 2.3 Illustration of the tortuous pathway. Polymer matrix containing nanoplatelets. Gas molecules cannot pass through directly, so a more tortuous path is taken, increasing diffusion time. α is aspect ratio = length/width [13]

The simplest model for diffusion of small components through a filled matrix was proposed by Maxwell's equation [59] for impermeable arrayed spheres:

$$\frac{P}{P_0} = \frac{1-\varphi}{1+\frac{\varphi}{2}} \tag{2.6}$$

However, this equation can be applied to dilute systems independent of the particle size. A similar model was also suggested by Raleigh [60] for arrayed infinite cylinders aligned parallel to the surface (Equation 2.7). However, this equation also did not consider the size of the particles.

$$\frac{P}{P_0} = \frac{1-\varphi}{1+\varphi} \tag{2.7}$$

Nielsen [61] developed a model which is taking aspect ratio -or size of the particles- into consideration:

$$\frac{P}{P_0} = \frac{1-\varphi}{1+\frac{\alpha\varphi}{2}} \tag{2.8}$$

where α is the aspect ratio of fillers [62]. The Nielsen model assumes a perfect orientation of nanoparticles is achieved within the matrix, and platelets have a rectangular shape. This model cannot be used for composites with high filler contents. Cussler et al. [61] proposed the geometric factor (dependent on size, shape, and level of positional disorder of nanoparticles) to predict the effect of filler shape.

$$\left(\frac{P}{P_0}\right)^{-1} = 1 + \mu\frac{\alpha^2\varphi^2}{1-\varphi} \tag{2.9}$$

As the perfect orientation is almost impossible in polymer nanocomposites, Bharadwaj [63] modified Nielsen's model and introduced an orientation parameter S, with three possible values: 0 for random orientation, 1 and -0.5 for the two extremes, perfect alignment perpendicular to the surface and vertical orientation, respectively

$$\frac{P}{P_0} = \frac{1-\varphi}{1+\frac{\alpha\varphi}{2}(\frac{2}{3})(S+\frac{1}{2})} \tag{2.10}$$

These permeability models can be applied by considering their pros and cons. For instance, they do not consider the synergistic effects originating from electrostatic or hydrogen bonding interactions between components or possible changes in interphase and matrix. Therefore, applying these models to complex systems such as hybrid nanocomposites or layer-by-layer coatings might give approximate results.

2.5 Layered double hydroxide

LDHs can be used to improve the barrier properties as they create a tortuous pathway within the polymer matrix. LDHs are a class of synthetic anionic clays with brucite-like cationic layers containing anions in the hydrated interlayer for charge balance. Figure 2.4 shows the structure of LDH with a general formula of $[M^{II}_{1-x}M^{III}_{x}(OH)_2](A^{n-})_{x/n}\cdot mH_2O$ (M^{II} and M^{III} are divalent and trivalent metals respectively, A^{n-} is interlayered anion). LDH can have a wide range of chemical compositions based on different metal species and interlayer anions.

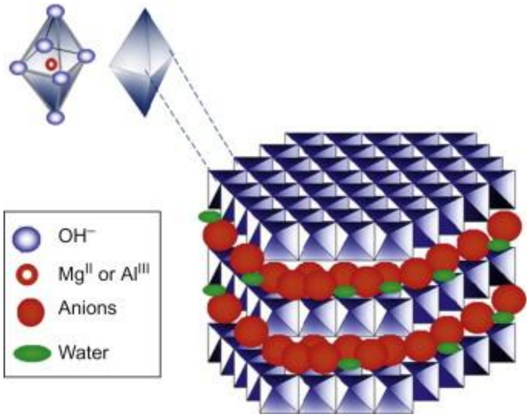

Figure 2.4 Structure of Layered double hydroxide [64]

Due to their compositional flexibility, high anion exchange capacity, and nontoxicity, LDHs have a wide range of applications, such as fire-retardant additives, absorbents in environmental purification, corrosion inhibitors, and polymer additives. Today, MgAl-LDHs can be found in the market and have regulatory approvals for food-contact materials[33].

LDH can be synthesized in two ways: top-down (delamination) and bottom-up (controlled nucleation). In top-down methods, the interlayer is modified first within suitable solvent systems, while in bottom-up methods, aqueous co-precipitation systems are required [64].

Hydrothermal treatment is often used to modify nanoparticles, particularly to adjust their aspect ratio. Various properties of nanoparticles, such as size, shape, crystallinity, and surface characteristics, can be modified with this approach [33, 65, 66]. The hydrothermal process involves placing a solution containing the nanoparticles into a sealed autoclave (Figure 2.5). The autoclave is then heated to temperatures ranging from 70 to 300°C and subjected to pressures between 1 to 10 MPa [67]. Under these conditions, water becomes highly reactive, acting as both a solvent and a reagent, which facilitates the modification of the nanoparticles.

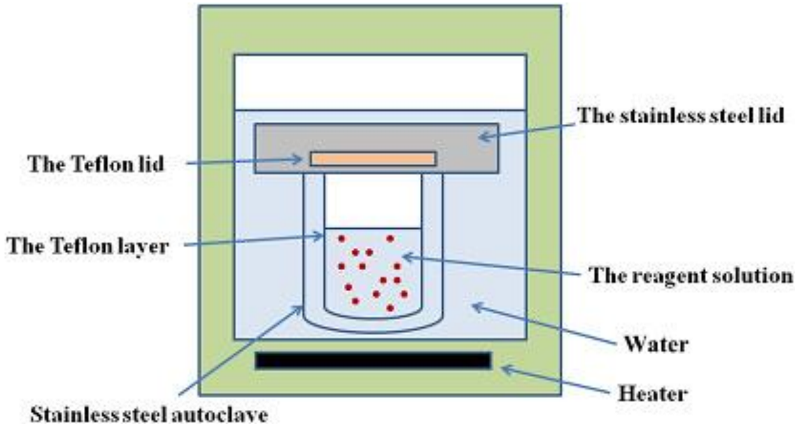

Figure 2.5 The standard setup for the synthesis of LDH nanoparticles by hydrothermal method [68]

During the hydrothermal treatment process, nanoparticles may experience simultaneous dissolution and recrystallization. The elevated temperature and pressure facilitate Ostwald ripening, where larger particles grow at the expense of smaller ones due to varying surface energy. This phenomenon results in a larger average particle size and a narrower size distribution. Furthermore, high temperatures and pressure can lead to crystallographic alterations in nanoparticles. With a longer time, thermodynamically stable phases may be formed [33, 65, 66].

The calcination-rehydration method using hydrothermal treatment is an effective way to produce high aspect ratio LDHs. It involves two steps: calcination of unmodified LDH (generally low aspect ratio) to obtain metal oxides and rehydration of obtained metal oxides in aqueous media to modify or rebuild LDHs. The hydrothermal treatment conditions, including pH, temperature, and duration, can significantly influence the size, shape, charge, and composition of the LDH. In a study by Yu et al. [69], the impact of reconstruction time during hydrothermal treatment on the aspect ratio of LDHs was investigated. As the reconstruction time increased from 16h to 96h, the thickness of LDHs decreased while the lateral dimension increased. LDH with an aspect ratio of approximately 336 ± 170 was achieved at 96h. Another study by Xu et al. [70] suggested that the stacking of LDHs is reduced at pH 7 compared to pH 10.5. However, the researchers did not quantify the aspect ratio of the final LDHs.

Incorporating LDH into polymers can significantly improve the mechanical, optical, and thermal properties. However, preparing exfoliated LDHs in a polymer matrix is extremely demanding as the interlayer electrostatic interactions need to be overcome. Exfoliation in high dielectric constant liquids such as formamide or amino acids with the help of mechanical stirring and sonication gives good results [71]. But the exfoliated LDHs are unstable and will reassemble into thickly layered structures after removing the delamination media [72, 73]. Therefore, stabilization of exfoliated LDHs is crucial to widening their applications. LDHs with a positively charged surface of each layer can be stabilized with negatively charged polymers or nanoparticles. For instance, Kang et al. [72] reported that the co-assembly of carboxymethyl cellulose with LDH was able to stabilize LDH in an aqueous solution, preventing the re-agglomeration of LDHs (Figure 2.6). In another study, it was shown that positively charged LDHs could be stabilized in an aqueous solution through complexation with alginate molecules that possess negative charges [73]. Negatively charged GO, boron nitride and molybdenum disulfide were also able to stabilize the positively charged LDHs.

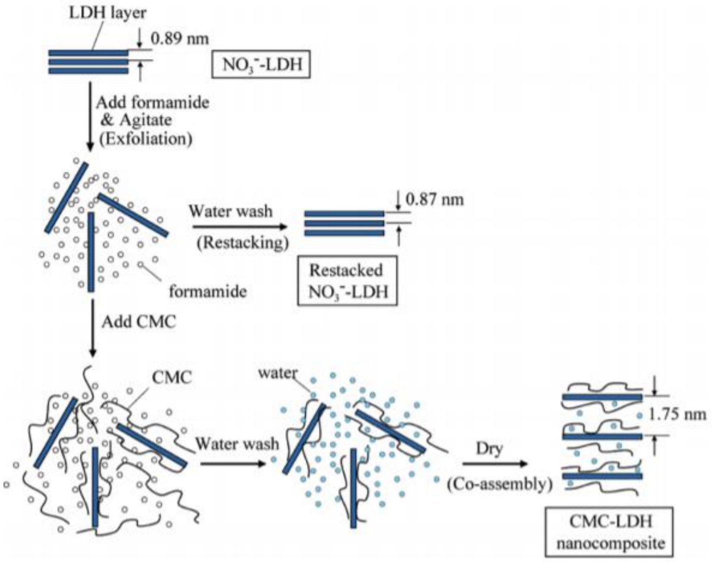

Figure 2.6 Illustration of the delamination of LDH by using CMC [72]

As mentioned before, LDHs enhance the gas performance of polymers as they create a tortuous pathway. Table 2.4 summarizes studies in which LDHs are used to improve the barrier properties of the system. Melt mixing [74] or simple solution casting [28, 41, 75] approaches were not able to improve the oxygen barrier properties; however, the use of secondary components such as surfactants [76] or nanoparticles [41] seems to help the improvement of the exfoliation of LDH and led to better barrier performance. Another critical factor that should be considered is the aspect ratio of LDHs. The use of high aspect ratio LDHs significantly enhances both the oxygen and water vapor barrier performance of coatings/films [28, 69, 77-79]. Another interesting feature of LDHs was explained by Pan et al. [77]. In their study, the authors showed that reconstructed LDHs could play an oxygen scavenger role due to the emergence of oxygen vacancies in reconstructed LDHs. They reported that chemisorption between reconstructed LDH and oxygen molecules improved oxygen barrier properties. Through X-ray photoelectron spectroscopy (XPS) and molecular dynamic simulation results, Dou et al. [58] indicated that the assembly process is driven by electrostatic interactions between the positively charged LDH and the negatively charged PAA; as a result, oxygen barrier performance dramatically improved.

Table 2.4 Different studies used LDH to improve oxygen barrier properties

Substrate	**Nanocomposite System**	**Method**	**OTR (cc/(m2 day)) or OP (cm^3 mm / (m^2 day atm)**	**P/P$_0$**	**Ref**	**Yr**
PET	(PAA/LDH)$_{15}$	LbL	0.15 cc/(m^2 day)	0.018	[58]	2015
PET	(PAA/LDH)$_{15}$	LbL	0.0071 cc/(m^2 day)	0.0008	[58]	2015
PET	(Chitosan/H-LDH)$_{10}$	Spin-LbL	<0.05 cc/(m^2 day)	0.06	[77]	2015
PET	(Chitosan/L-LDH)$_{10}$	Spin - LbL	2.4 cc/(m^2 day)	0.6	[77]	2015
PET	(CA/L-LDH)$_{20}$	Spin LbL	25 cc/(m^2 day)	0.036	[28]	2014
PET	(CA/H-LDH)$_{20}$	Spin-LbL	<0.05 cc/(m^2 day)	0.00007	[28]	2014
PET	PVA/LDH (%60LDH)	RC	<0.05 cc/(m^2 day)	0.00004	[69]	2019
PET	PVA/LDH (%70LDH)	RC	0.43 cc/(m^2 day)	0.006	[78]	2021
PET	(PVA/H-LDH)$_{30}$	LbL	0.62 cc/(m^2 day)	0.078	[79]	2017
PET	(PVA/L-LDH)$_{30}$	LbL	6.1 cc/(m^2 day)	0.76	[79]	2017
-	PLA/LDH-surfactant	SC	380 cm^3/m^2.bar.d	0.75	[76]	2015
-	PVA/LDH	SC	1.9 cm^3 mm/ m^2 atm d	0.77	[41]	2021
-	PVA/LDH-GO	SC	0.095 cm^3 mm/ m^2 atm d	0.036	[41]	2021
-	PVA/LDH-BN	SC	0.8 cm^3 mm/ m^2 atm d	0.032	[41]	2021
-	(PDMS/LDH+surfactant)$_{10}$	LbL	0.7 cc/(m^2 day)	0.0063	[80]	2018
PET	(PSS/LDH)$_{20}$	LbL	10 cc/(m^2 day)	0.2	[81]	2014
PET	(PVA/PSS-LDH)$_{10}$	LbL	0.72 cc/(m^2 day)	0.02	[81]	2014

Table 2.4 (continued)

PET	$(CMC/LDH)_{20}$	LbL	0.106 cc/(m^2 day)	0.001	[42]	2014
-	PE/Starch/LDH	TSE	55 cc/(m^2 day)	0.2	[74]	2013

SC: solution casting, TSE: twin screw extruder, LbL: Layer-by-layer assembly, RC: Rod coating, GO: graphene oxide, PVA: polyvinyl alcohol, PE: polyethylene, CA: cellulose acetate PET: polyethylene terephthalate, LDH: layered double hydroxide, H-LDH: high aspect ratio LDH, L-LDH: low aspect ratio LDH, PDMS:polydimethylsiloxane, PSS: poly(sodium styrene-4- sulfonate), PAA: polyacrylic acid

2.6 Hybrid nanocomposite systems

Recent studies have shown that hybrid systems formed by combining two different nanoparticles are a promising way to improve nanoparticle dispersions, hence the final properties of the system. Prof. Ica Manas-Zloczower's group conducted a fundamental study on the synergistic effect of using two different nanoparticles, namely, CNT-graphene nanoplate (GNP) in epoxy [82]. The combination of CNT and GNP in a ratio of 8:2 synergistically increased the flexural properties and reduced the electrical percolation threshold for the epoxy composites, indicating easier formation of a conductive network due to the improved state of CNT dispersion in the presence of GNPs. Grunlan et al. [83] reported that upon the addition of nanoclay into the epoxy/CNT nanocomposites, the dispersion of CNTs could be substantially improved. They explained that in two ways: (i) the increase in the viscosity forces CNT agglomerates to break up and hinder their re-agglomeration and (ii) affinity between the CNT and nanoclay.

Another example that shows the advantage of using a secondary nanofiller to improve the final properties was given by Zuo et al. [84], where researchers incorporated GO and MMT into polyimide. Their TEM results indicated that GO dispersion within polyimide enhanced considerably with the help of MMT. They attributed this behavior to the two physical interactions: (i) ionic interactions and (ii) hydrogen bonding between nanomaterials. Bhattacharya et al. [85] also demonstrated that electrostatic interaction between oppositely charged nanomaterials could help to improve the dispersion. In this context, they investigated the dispersion of positively charged carbon black within natural rubber in the presence of negatively charged nanoparticles such as MMT, carbon nanofiber, and sepiolite. They showed that barrier properties of produced hybrid nanocomposite systems could be improved due to the increase in the dispersion level of nanoparticles.

It should be noted that hybrid nanocomposite systems are also crucial in terms of application since using secondary filler not only helps the dispersion improvement but can also provide additional functionalities to the system, such as flame retardancy, processability, and electrical conductivity [86-88]. For instance, Trifol et al. [89] showed that the addition helped to mitigate the brittleness of MMT-loaded PLA while synergistic improvement in both OTR and WVTR with the combination of MMT and CNF was observed. A reduction of 90% in the OTR and 76% of the WVTR was achieved in hybrid PLA/MMT-CNF compared to neat PLA. In another study[41], LDH was modified using a series of different 2D nanosheets such as GO, boron nitride, and molybdenum disulfide based on the concept of electrostatic interactions. It was shown that the oxygen barrier properties of PVA show a 25-fold improvement upon GO-LDH addition. In another study [88], synergistically improved co-dispersion of negatively charged MMT and positively charged modified-CNT increased the modulus and tensile strength of styrene-butadiene rubber.

It has been reported that the use of secondary nanomaterials can also improve the barrier properties by filling the defects in the primary nanomaterials [90]. For instance, the combination of laponite and MMT within PVA dramatically improves the barrier performance of coatings compared to PVA/MMT or PVA/LAP systems, as the smaller laponite particles were able to fill the cracks of MMT[90]. The same concept was also reported in another study [91] for GO/LAP systems. In a patented study by Luyi Sun's group [92], it was claimed that the bending of GO can be hindered with the addition of MMT, and this led to significant improvement in OTR.

In addition to those mentioned effects, it was shown that the addition of secondary nanoparticles can improve the coating quality and reduce defects. Schmidt et al. [93] filed a patent on the application of TEMPO-oxidized CNF in a digital printing receiving layer —which includes PVA and pigments. Incorporating 0.05 wt.% CNF into the curtain coating formulation reduced cracking by approximately 50% compared to formulations without CNF.

2.7 Water-based barrier coatings for paper packaging

Untreated/uncoated paper offers a limited barrier against liquid water, water vapor, oxygen, and other chemicals. Therefore, these materials are typically coated to provide sufficient barriers against the of water and gases such as oxygen. In the production of coated paper, commonly used methods include extrusion coating, wax dipping, metallization, and water-based dispersion coating methods. All these methods, sometimes a combination of them, are employed in the food packaging industry, with the choice of technique generally determined by the specific end-use application and cost considerations. Using water-based dispersion coating on a paper enhances recyclability compared to other methods such as metal films or polymer extrusion coatings.

Determining the performance of water-based paper coatings is more complex than plastic packaging systems. The type and characteristics of paper substrate (e.g., porosity, surface roughness, surface pH, chemo-physical composition of surface, compressibility), type of permeant (e.g., water, oxygen, air, oil), type of coating method and conditions (e.g., rod, curtain, coating speed, drying temperature), interaction between paper and coating (e.g., fiber swelling, adhesion) directly affect the barrier performance.

Achieving a high oxygen barrier performance without sacrificing recyclability or water vapor properties is the biggest challenge in paper packaging. Some studies achieved a good oxygen barrier performance; however, they mostly use high coating weight or thickness, which highly limits the application and recyclability of paper. Table 2.5 lists the studies that found the lowest OTR or WVTR values in paper coatings obtained through water-based coating approaches. For instance, one of the studies that applied the lowest coating weight was on starch and PVA. The researchers found an OTR of 23.9 cc/m^2 day and a WVTR of 38 g/m^{2}day can be achieved with 9.4 g/m^2. Some other studies applied even higher coating weights of 26 and 34 g/m^2. The critical conclusion was that PVA performs well in terms of oxygen permeability [94].

Table 2.5 High barrier coating studies on paper

Coating mixture	**OTR (cc/m^2 day) 23°C, %50 RH**	**WVTR (g/m^2 day) 23°C, %50 RH**	**Coating Thickness (μm)**	**Coating Weight (g/m^2)**	**Ref.**
Starch-PVA	23.9	38	6.5	9.4	[95]
Starch-glycerol/zein bilayer (2 layers)	262	299	100	145	[96]
Pigment coating-CNC-PLA (3 layers)	6	28	46	34.6	[97]
Pigment coating-CNC-LDPE (3 layers)	10	8	23	26	[97]
PE – pre-coating and Al_2O_3 (3 layers)	818	4.6	-	-	[98]
PVA-SiO2-polydopamine	0.3	4.1 (37, %90RH)	77.7	-	[99]
Chitosan (1 layer)	17 (0 RH)	-	3.5	5	[100]
PVA-maleic acid-Nanoparticle (Crosslinked)	0.1	162 (37, %90RH)	-	12.2	[101]
PVA-MFC-latex (double layer)	6 (0 RH)	0.5	40	15	[94]
Chitosan	257	70	12	25	[102]
PC−SA/SiO2	57.942	206.95	54.6	45.49	[103]

CNC: Cellulose nanocrystal, PLA: Polylactic acid, LDPE: Low-density polyethylene, PVA: Polyvinyl alcohol, MFC: microfibrillated cellulose, SA: stearic acid

2.8 Recyclability Barrier Coatings/Films

This research project uses recyclability terminology to evaluate the capability of coating washing out from the paper. A paper can be reused when the fibers it contains can be effectively and efficiently recovered to produce a new paper of suitable quality. Indeed, recycling problems of paper packaging are more about feasibility/economics than technical issues. This is because most of the coated paper packages can be recyclable, but it depends on the paper products' yield, energy, and value. In general, the recyclability of paper coatings depends on factors such as thickness, precoating, hydrophobicity, and rheological properties. The thickness of a coating plays a crucial role in recyclability, as thicker coatings tend to be more challenging and time-consuming to recycle than thinner ones. A suitable precoating can prevent barrier dispersion from penetrating the substrate, enhancing recyclability, as seen in using nanocelluloses to improve polyethylene-coated paper recyclability [104]. Hydrophobic coatings may extend recycling time or obstruct the process altogether. The rheological properties of a coating, such as its viscosity, directly influence how deeply the coating penetrates the paper fibrils, affecting both performance and recyclability.

For instance, some polymer laminations and metal foil mostly stay in one piece and can also remain attached to the fiber. Thus, the efficiency of recyclability is reduced [105]. Latexes may form colloids, such as vinyl acrylates, styrene-butadiene rubber, and polyvinyl acetate. The instability of these colloids -due to changes in chemical conditions or temperature- causes the formation of stickies during the recyclability process. These stickies can damage the equipment and create non-uniform surface properties on paper, which causes undesired printability problems and renders the products unattractive to the manufacturer. Waxes such as beeswax with a hydrophobic structure can easily diffuse into paper fibrils and create severe problems during recyclability [106].

In general, it could be said that efficient recyclability of coatings can be ensured with good repulpability, high paper fiber yield, easy removal of non-paper components, and a small amount of micro “stickies.”

However, few studies have investigated the recyclability of paper coatings in the literature, and there is no consistency in the recyclability procedure. For instance, Bideau et al. [107] mixed TEMPO-oxidized CNF (TCNF) with polypyrrole (PPy) and coated paperboard. After ten minutes in water, their coating could be removed by using a spatula. However, this procedure is not suitable for industrial applications. Moreover, they did not show any data to evaluate the recyclability of the coating. In a very recent study [108], an alkali solution (pH = 12) was employed at 90 ˚C to remove silanized castor oil coating from paper. The authors claimed that the coatings were completely removed when exposed to alkali solution for 3h; however, they did not show any results, only photographs of the coatings. In another study [109], the recyclability of zein-wax-coated paper was investigated through enzyme washing, and the mechanical properties of coated, uncoated, and recycled papers were compared. They showed that the tensile, burst, and tear index of recycled paper is comparable to that of uncoated paper, which indicates the removal of the coating. In a recent study by Kansal et al. [110] four different approaches were used to assess the recyclability of chitosan-zein-coated paper. The recyclability procedures include washing with (i) DI water, (ii) acetic acid solution, (iii) ethanol solution, (iv) ethanol + acetic acid solution. Authors claimed that the color changes -from yellowish to dark-brown- after washing with ethanol and acetic acid solution indicates successful removal of coatings.

Zhang et al. [111] to examine the recyclability of PLA/zinc oxide coating. All the ‘‘rejects” (material separated by the screen) and the ‘‘accepts” (fibrous material passing through the screen and possible coating fragments and filler particles) are collected, filtered, and oven-dried overnight to obtain solid content. To quantitatively assess the recyclability performance of their coating, they did mass balance through (i) weighting accepts-rejects, (ii)mass spectroscopy, and (iii) ash content measurements. Authors reported that the waste is very high (%21), which can be rated as ‘level C’ according to UNI11743. The explanation for high waste was the use of solution-based coatings. Solutions lower the viscosity, and PLA can penetrate deep into paper fibrils and bind fibrils together. So, a significant amount of paper fibrils were rejected by PLA during recycling.

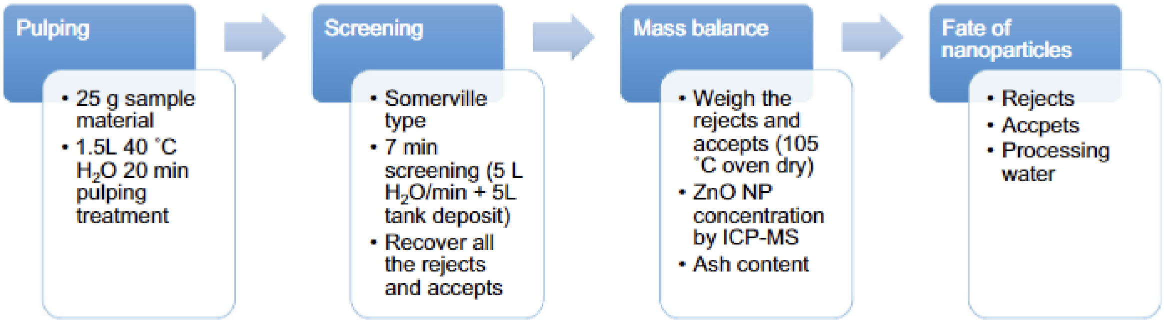

Figure 2.7 The recyclability protocol reported in a study by Zhang et al. [108]

2.9 Summary of Literature Review and Problem Identification

In summary of the literature review, there is a growing demand for recyclable alternatives for packaging materials, and water-based barrier coatings are being seen as a promising solution. The use of high-aspect-ratio nanofillers is crucial for achieving low oxygen and water vapor barrier systems. Studies have shown that high aspect ratio LDHs significantly improve the oxygen barrier properties of films and coatings [28, 33, 40, 41, 58]. However, there is a lack of research on how hydrothermal treatment conditions, such as pH, time, and temperature, affect the control of LDH aspect ratios. Addressing this gap could expand LDH applications in barrier coatings. Furthermore, hybrid systems, which have the potential to enhance gas barrier properties and offer additional functionalities, are gaining popularity. Most hybrid systems studied so far involve natural nanoclays or carbon-based particles, with no reported studies on LDH-TCNF systems. Low coating weights are crucial to maintaining recyclability and ensuring industrial feasibility. However, most studies apply high coating weights to paper. No research has successfully achieved balanced oxygen-water vapor gas barrier properties with low coating weights while preserving recyclability. Despite the importance of producing recyclable coating for paper, significant efforts are still required to develop fully recyclable coatings and implement a suitable recycling process for the paper industry. This study aims to address these challenges.

CHAPTER 3 OBJECTIVES AND ORGANIZATION OF ARTICLES

3.1 General Objectives

The main objective of this research proposal is to develop a recyclable and high-barrier paper coating for food packaging applications.

3.2 Specific Objectives

Specific objectives can be listed as:

- To establish a fundamental understanding of the effect of hydrothermal treatment conditions on the synthesis of high aspect ratio LDH for high-gas barrier applications.
- Developing the oxygen barrier coatings through a hybrid approach using oppositely charged LDH-TCNF within PVA and determining the microstructure-final properties relationship.
- Developing a repulpable - high oxygen and water vapor gas barrier paper coatings and understanding each component's role in the formulation.

3.3 Organization of articles

The main achievements of this work are presented in the form of three scientific papers in the following chapters:

Chapter 5 presents the results of the first paper, “Towards High Aspect Ratio Layered Double Hydroxides for Gas Barrier Applications: Effects of Hydrothermal Conditions,” submitted to *Applied Clay Science* in October 2024. This article studied the impact of hydrothermal treatment conditions like pH, time, and temperature on LDH morphology and aspect ratio. We use glycine to improve the stacking and obtain a high aspect ratio. Interactions between glycine, LDH, and pre-LDH species at different conditions were characterized with rheometer and FTIR. We also showed how the aspect ratio and sizes of LDH were affected by various conditions through AFM, TEM, and SEM. We further used XRD, zeta potential, DLS, and EDX to characterize the crystalline structure, surface, and chemical characteristics of various LDHs. Final LDH-glycine gels were applied on PET substrate, and OTRs were measured using permeability devices.

Chapter 6 presents the second article, “Electrostatically Complexed Polyvinyl Alcohol-Layered Double Hydroxides-TEMPO-Oxidized Cellulose Nanofibers Gas Barrier Coatings” submitted to *Advanced Composites and Hybrid Materials* in October 2024. This article systematically investigated the electrostatic interactions between oppositely charged LDH-TCNF in PVA. We used rheometer, sedimentation studies, XRD, and FTIR to understand these interactions. We have shown that TCNF and LDH synergistically affect gas barrier performance. We attributed this synergistic effect to an electrostatically complex network PVA-LDH-TCNF structure that maximizes tortuosity, reduces free volume, and modifies the nanoparticles. It was shown that superior oxygen gas performance was achieved in PVA-LDH-TCNF than in only-LDH or only-TCNF PVA coatings. All these are confirmed with various permeability models.

Chapter 7 presents the third article, “Repulpable and High Gas Barrier Polyvinyl Alcohol-Cellulose Nanofiber-Layered Double Hydroxide Coatings,” submitted to *Carbohydrate Polymers* in November 2024. In this study, we developed repulpable PVA-LDH-TCNF coatings that enhance barriers against oxygen and water vapor. We applied them to paper at a low weight of 5.2 g/m^2 using an automatic bar coater and infrared dryer for quick drying. The effect of LDH-TCNF on water retention and viscosity is studied through a rheometer. We measured the penetration of coating inside paper using darkfield fluorescence microscopy. Blistering was also characterized. The oxygen transmission rate at 0, 50, and 90 relative humidity and water vapor permeability are measured. We also applied thermal treatment to improve the gas barrier at higher relative humidities. Finally, we quantified the repulpability of coated papers. Overall, the PVA-LDH-TCNF coating offers excellent barriers against oxygen and water vapor, making it a practical choice for recyclable packaging.

CHAPTER 4 ARTICLE 1: TOWARDS HIGH ASPECT RATIO LAYERED DOUBLE HYDROXIDES FOR GAS BARRIER APPLICATIONS: EFFECTS OF HYDROTHERMAL CONDITIONS

Emre Vatansever[1] Amir Saffar[1,2], Abdellah Ajji[1]*

1: 3SPack, Research Center for High Performance Polymer and Composite Systems (CREPEC),
Chemical Engineering Department, Polytechnique Montréal, Montréal, Québec H3C 3A7, Canada

2 ProAmpac Terrebonne, QC, Canada J6Y 1V2
**Corresponding Author email: abdellah.ajji@polymtl.ca*

Submitted to Applied Clay Science on October 26, 2024

Abstract

In this study, we examined how hydrothermal treatment parameters—temperature, time, and pH—affect the aspect ratio of MgAl-layered double hydroxides (LDHs) synthesized in the presence of glycine. The reconstruction of layered double oxides (LDOs) in concentrated aqueous glycine solutions yielded stable dispersions of LDH nanosheets. Hydrothermal treatments were conducted under mildly acidic (pH 6) and alkaline (pH 9.5) conditions at 100 °C and 140 °C for 1, 3, and 5 days. At pH 6, glycine in its zwitterionic form effectively stabilized the LDH layers, reducing stacking along the thickness direction and achieving an aspect ratio of 132 ± 35 at 100 °C after 3 days. Conversely, at pH 9.5, weaker glycine-LDH interactions and higher charge density increased layer stacking, lowering the aspect ratio. Higher temperatures (140 °C) further enhanced stacking, broadening the size distribution while extending the reconstruction time from 1 to 5 days, reduced stacking, and increased aspect ratios up to ~200. Using a bar coating approach, positively charged LDH-glycine dispersions were coated on negatively charged corona-treated polyethylene terephthalate (PET) films. LDHs with higher aspect ratios significantly improved the oxygen barrier properties of PET films, as demonstrated by a substantial reduction in the oxygen transmission rate from 129 cc/m²·day·atm to 0.25 cc/m²·day·atm with only 455 nm coating thickness. These findings highlight the important relationship between hydrothermal conditions, LDH morphology, and aspect ratio, offering valuable insights for optimizing LDH synthesis for high-performance barrier coatings.

Keywords: layered double hydroxide, LDH, hydrothermal, glycine, high aspect ratio, oxygen permeability, pH

4.1 Introduction

Synthesizing high aspect ratio layered double hydroxides (LDHs) for gas barrier applications has gained considerable interest in the last decade [28, 33, 41, 43, 58, 64, 75, 78, 112]. Layered double hydroxides (LDHs), also known as hydrotalcite, are a class of anionic clays consisting of inorganic sheets carrying positive charges and intercalated anions between the sheets. The general formula for LDH is $M^{2+}{}_{1-x}\,M^{3+}{}_{x}(OH)_2A_x\ nH_2O$, in which M^{2+} is metallic cations such as Mg^{2+},Zn^{2+},Ni^{2+} and $M^{3+} = Al^{3+}$,Fe^{3+}, etc., and A denotes intercalated anion which can be $CO_3{}^{2-}$, Cl^- , OH^-, etc. The positive charge in LDHs results from the substitution of M^{2+} cations by M^{3+} cations. This positive charge is balanced by intercalated anions in conjunction with water.

The conventional method for synthesizing LDHs involves co-precipitation at constant or varied pH followed by aging. However, the co-precipitation method has some drawbacks, including a multi-step synthesis route, the potential for a large number of stacking or aggregation of LDHs, poor morphology, and the production of large amounts of waste [113-119]. In contrast, hydrothermal synthesis of LDHs is more practical as it does not require any toxic chemicals, mechanical treatment, or a special atmosphere. Hydrothermal treatment can also prevent agglomeration/stacking issues due to Brownian motion generated during the process [66, 113, 120-122]. For instance, Xu et al. [113] showed that while co-precipitation resulted in partially dispersed/delaminated LDHs, using hydrothermal treatment led to well-dispersed—or delaminated—LDHs.

One of the significant areas of LDH research that has experienced rapid growth is the study of high aspect ratio (defined as the ratio of platelet diameter to thickness) LDH synthesis. The aspect ratio and morphology of LDHs are important in various applications such as catalyst, biomedical, and gas barrier applications [28, 40, 123, 124]. The aspect ratio of LDHs is significantly influenced by their restacking and dispersion within the medium, which can be adjusted by modifying the hydrothermal conditions during synthesis. While most studies focus on how hydrothermal treatment affects the crystallite size of LDHs, only a few have explored its impact on restacking, delamination, and aspect ratio. In one study, Yu et al. [33] investigated the effect of reconstruction time during hydrothermal treatment on the aspect ratio. They found that increasing the reconstruction time from 16 to 96 hours reduced the thickness and increased the lateral dimensions of the LDH, resulting in an aspect ratio of approximately 336 ± 170 after 96 hours. Another study by Xu et al. [70] showed that LDH stacking decreased at pH 7 compared to pH 10.5, though they did not quantify the aspect ratio of the resulting LDHs.

In this study, aqueous glycine was used as a medium, and hydrothermal treatment conditions such as pH, temperature, and reconstruction time were changed to understand high aspect ratio LDH formation. Synthesized LDHs were characterized by X-ray diffraction (XRD), transmission electron microscopy (TEM), rheological measurements, energy dispersive X-ray analysis (EDX), zeta potential, and dynamic scattering analysis. We also used atomic force microscopy (AFM) to quantify the aspect ratio of LDHs. By correlating the synthesis pH, temperature, time, and final structures, a plausible formation mechanism was proposed to synthesize high aspect ratio LDHs. Since LDHs are promising nanoparticle candidates in gas barrier applications, LDH coatings were prepared by applying positively charged LDH gels on negatively charged PET substrate using a simple bar coating approach, and the oxygen gas barrier of coatings was characterized.

4.2 Materials and Methods

4.2.1 Materials and substrates

Original low aspect ratio LDH (DHT-4A) was provided by Kisuma Chemicals. It was further modified to obtain high aspect ratio LDHs. Glycine (≥98% purity), sodium hydroxide (≥98% purity), and hydrochloric acid (37% concentration) were obtained from Sigma Aldrich. Polyethylene terephthalate (PET) film (13 µm) was supplied by ProAmpac.

4.2.2 Calcination and hydrothermal synthesize of LDHs

High aspect ratio LDHs were synthesized using a calcination-rehydration approach. We subjected the original LDH to calcination at 500 °C for 12 hours with a heating rate of 5 °C/min to obtain a metal oxide mixture in layered oxide form. A calcination temperature of 500°C was chosen due to similar amino acid uptake at both 500 °C and 600 °C, as reported in previous studies [125]. All LDH samples detailed in Table 4.1 were synthesized through a hydrothermal method. For example, LDH coded as 6_100_3d in Table 4.1 was prepared by mixing 2 g of layered double oxide (LDO) with 20 ml of aqueous glycine solution at a ratio of 1:1.5 (LDH-glycine). The mixture's pH was adjusted to 6 and placed in a Teflon-lined autoclave, which was then heated to 100°C for 3 days. After the reactions, the autoclave was allowed to cool down to room temperature. Table 4.1 details all LDHs prepared using different parameters such as initial pH, time, and temperature.

4.2.3 Film Preparation

LDHs prepared through different hydrothermal conditions were diluted to a 5 wt% concentration in deionized water and further dispersed by using ultrasonication for 180 sec using an ultrasonic probe (Cole-Parmer) at 30 W. These coating dispersions were then applied to a 13 μm thick freshly corona-treated PET substrate. An automatic coater (TQC Sheen AB 3650), equipped with a Mayer rod with a coating gap of 30 μm, was utilized for the application process. Approximately 2 mL of the prepared LDH gel was deposited on the substrate. The Mayer rod moved at a controlled speed, resulting in the formation of a coated film. All coated samples were air-dried naturally at room temperature. Film thicknesses were calculated from coating weight using the density of 2.2 g.

4.2.4 X-ray powder diffraction (XRD)

X-ray powder diffraction (XRD) analysis was conducted using a PANalytical X'Pert Pro diffractometer operating in diffraction mode, with a voltage of 40 kV and a current intensity of 40 mA, utilizing Cu-Kα radiation ($\lambda = 1.5406$ Å). LDHs and LDO powders were loaded into stainless steel sample holders for analysis. LDH dispersions were coated onto a silicon wafer, dried at room temperature, and placed into the sample holder. Data was collected over the 2θ range from 3 to 70° at a scanning rate of 0.08°/s.

4.2.5 Fourier transform infrared spectrometer (FTIR)

Fourier transform infrared (FTIR) analysis was performed using a PerkinElmer 65 FTIR spectrometer (PerkinElmer, Woodbridge, ON, Canada) in attenuated total reflection (ATR) mode. Spectra were acquired in the 600 – 4000 cm^{-1} range, comprising an accumulation of 36 scans with a resolution of 4 cm^{-1}.

4.2.6 Zeta Potential and Dynamic Light Scattering (DLS) Measurements

The zeta potential, hydrodynamic size, and colloidal stability of the dispersed LDH particles were determined using a Nano ZS Zetasizer. Five runs were conducted for each sample, and the data were fitted using the Smoluchowski model. An average of three measurements was obtained for each sample, and the mean value was reported.

4.2.7 Rheological measurements

The rheological behaviors of LDH/glycine suspensions were analyzed using a rotational rheometer (Anton Paar, MCR501, Germany) to investigate the electrostatic and hydrogen bond interactions. Rheological tests were conducted with a concentric cylinder. Frequency sweep tests were performed ranging from 100 to 1 rad/s. Before each test, solutions were pre-sheared to eliminate air from the sample and ensure a consistent starting microstructure. All tests were carried out at 25°C.

4.2.8 Transmission Electron Microscopy (TEM)

Transmission electron microscopy images were acquired utilizing a JEOL JEM-F200 (Japan), operated at 200 kV. To prepare the sample, a droplet of the LDH-containing suspension was deposited onto a carbon film-supported holder, allowed to dry, and subsequently sputtered with platinum before imaging.

4.2.9 Surface composition

Surface composition, particularly Mg and Al, was analyzed using scanning electron microscopy with energy-dispersive X-ray (SEM-EDX) spectroscopy (Hitachi TM3030Plus equipment, Tokyo, Japan) at 15 kV, with a resolution of 512 by 340 pixels and a pixel size of 0.01 µm.

4.2.10 Atomic Force Microscopy (AFM)

The aspect ratio of LDHs was measured using a NanoScope MultiMode atomic force microscopy in tapping mode, utilizing a silicon tip coated with aluminum having a force constant of 40 $N.m^{-1}$. LDH samples, diluted to approximately 0.01 mM, were deposited onto freshly cleaved mica wafers for AFM imaging.

4.2.11 Oxygen transmission rate measurement

MOCON OXTRAN 2/21 (Minneapolis, USA) apparatus was used to measure the permeability to oxygen at 0% relative humidity, 23 °C, and 1 atm pressure, as described in the ASTM standards D-3985-81 and ASTM F1927 using 5 cm^2 samples. A temperature of 23 °C and a humidity of 0 % RH were maintained on both sides of the sample. The oxygen transmission rate (OTR) (cc /m^2day) was converted to oxygen permeability (OP) [$10^{-16} cm^3(STP)\cdot cm\cdot cm^{-2}\cdot s^{-1}\cdot Pa^{-1}$] to compare the oxygen barrier performance of different films with different coating layers and different coating technologies that exist in the market and literature. The measurements were performed in three duplicates.

4.3 Results and Discussion

4.3.1 Preliminary Observations

After reconstructing LDO in aqueous glycine, gel-like products were obtained for all LDHs. The swelling observed can be attributed to two main factors: (i) the molecular structure of the zwitterionic compound (glycine in this study), which enhances the relative permittivity of water, and (ii) the ability of the zwitterion to form inter-lamellar hydrogen bonding networks and electrostatic interactions with LDH [39, 78, 126-128]. A higher number of hydrogen bonds established can indicate more stable LDHs. A detailed discussion about the effect of different conditions on the stability of LDHs will be provided in the following sections.

The pH of the solutions after the reaction for all samples was between 8.8 and 9.3, indicating successful LDH preparation in all cases (Table 4.1). The LDH suspensions exhibited a positive zeta (ζ) potential, varying from 22 to 35 mV. The positive ζ-potential value is consistent with the positively charged nature of the LDH layers due to the isomorphous substitution of the Mg^{2+} by Al^{3+}. Elemental analysis of various LDHs yielded an atomic ratio of Mg/Al between 1.86 to 2.16. Additionally, the FTIR spectra of LDHs synthesized under different hydrothermal conditions exhibited consistent features, as detailed in the Supporting Information, confirming their chemical composition and structure uniformity.

In XRD graphs (Figure 4.1a), distinct LDH structures were evident, characterized by sharp and symmetric peaks at lower 2θ angles, alongside broader and asymmetric peaks at higher 2θ angles (22° to 24°). To quantitatively analyze the interlayer spacing, denoted as d_{003}, the position and half-width of the (003) reflections were utilized, and calculations were performed using the Bragg diffraction formula. The results summarized in Table 4.2 consistently revealed d_{003} values ranging from 0.75 to 0.78 nm for all LDH samples. These findings indicate the successful intercalation of glycine molecules within the LDH layers.

To assess the crystallite size in the c-axis (stacking direction), we employed the Scherrer approximation, defined as follows: $D = 0.9\lambda/\beta\mathrm{Cos}\theta$, where λ represents the X-ray wavelength ($\lambda = 1.5406$ Å), β is the full width at half maximum (FWHM, in radians), and θ denotes the Bragg's angle in degrees. By employing profile fitting of the recorded XRD results, we determined the FWHM values for all the peaks (Table S2). The results highlighted a strong dependency of c-axis stacking on the hydrothermal treatment conditions, with values ranging from 9.1 nm to 18.8 nm for different LDHs (Table S2).

Table 4.1 Synthesize conditions, final compositions, and zeta potentials of various LDHs

Sample	Time (day)	Initial pH	Temperature (°C)	Mg/Al ratio[a] (Final)	Zeta Potential(mV) (Final)	Final pH
9.5-100-3d	3	9.5	100	1.868	30.3	9.3
6-100-3d	3	6	100	1.959	28.1	8.8
6-100-5d	5	5.9	100	2.16	29	8.9
6-100-1d	1	5.8	100	1.91	24	9
6-140-3d	3	5.9	140	2.05	36.3	9.2

a Synthesis conditions and final compositions and zeta potentials of various LDHs

The high pressure generated within the autoclave during hydrothermal treatment allows glycine molecules to be inserted into the interlayer region of the hydrated pre-LDHs. Meanwhile, excess glycine surrounds the LDHs, which is crucial because it prevents the stacking of LDH sheets during the reconstruction process. Aqueous glycine plays a significant role in this procedure; its presence increases the relative permittivity of the solution and disrupts the hydrogen bonding networks within the LDH layers [35, 40, 78]. As a result, the structures become loosely attached [78, 129]. After hydrothermal treatment, we used ultrasonication to break apart and disperse the loosely connected LDH structures. This step was important for producing LDHs with a high aspect ratio, meaning the layers were successfully separated and the LDHs were evenly dispersed.

The alterations in hydrothermal treatment conditions have significant implications for both the reconstruction process (involving metal oxide hydration and LDH dissolution-recrystallization) and the interaction between LDH layers and glycine [65, 67, 70, 118, 129, 130]. So, it is crucial to examine the influence of hydrothermal treatment conditions on the LDH aspect ratio from two distinct perspectives: (i) its effect on dissolution and crystal growth in the lateral directions (a and b axes), and (ii) its impact on LDH sheet exfoliation (or stacking along the c-axis) (as illustrated in

Figure 4.2). These considerations are fundamental for a comprehensive understanding of how hydrothermal treatment conditions affect the morphology and structure of LDH.

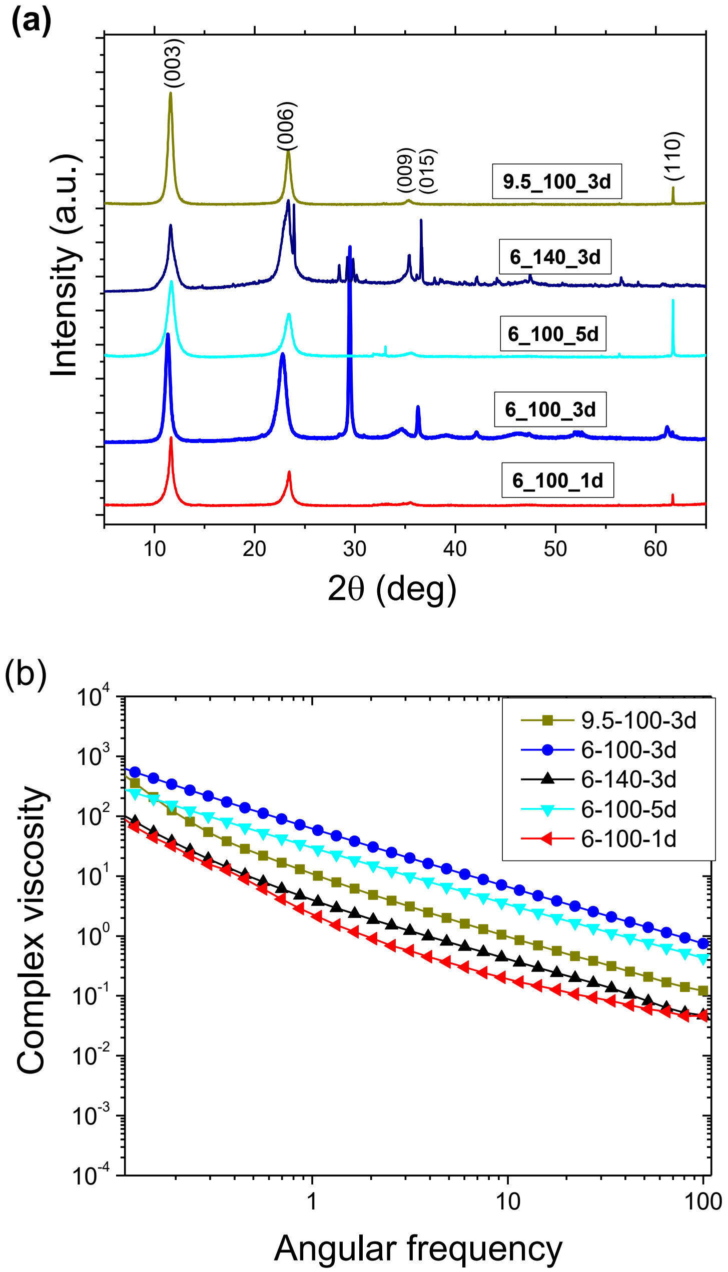

Figure 4.1(a) XRD results of LDHs prepared through different hydrothermal conditions, d-spacing, and crystal size calculated through XRD data listen in Table 4.1 (b) Complex viscosity vs angular frequency results of LDH gels (LDHs within aqueous glycine) are prepared at different conditions. Viscosity upturn at low frequencies can be an indication of a larger number of hydrogen bonding and/or electrostatic interactions.

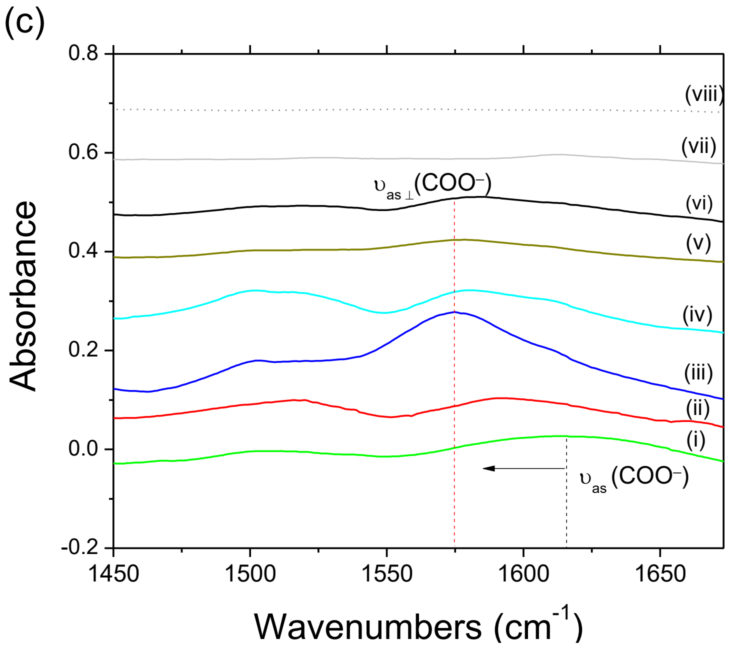

Figure 4.1 (continued) **c)** IR spectra: (i) glycine (ii) 6_100_1d (iii) 6_100_3d, (iv) 6_100_5d (v) 10_100_3d (vi) 6_140_3d (vii) 6_100_3d prepared using only water (no glycine) (viii) 9.5_100_3d prepared using only water (no glycine) The formation of hydrogen bonding and electrostatic interactions evidenced by a shift of the asymmetric vibration of COO^- group of glycine (1615 cm^{-1}) to lower wavelength during reconstruction in glycine solution [33, 131-133]. The black line is assigned to the asymmetric vibration of COO^- group, and the red line is attributed to the shift to an orthogonal position of part of the group.

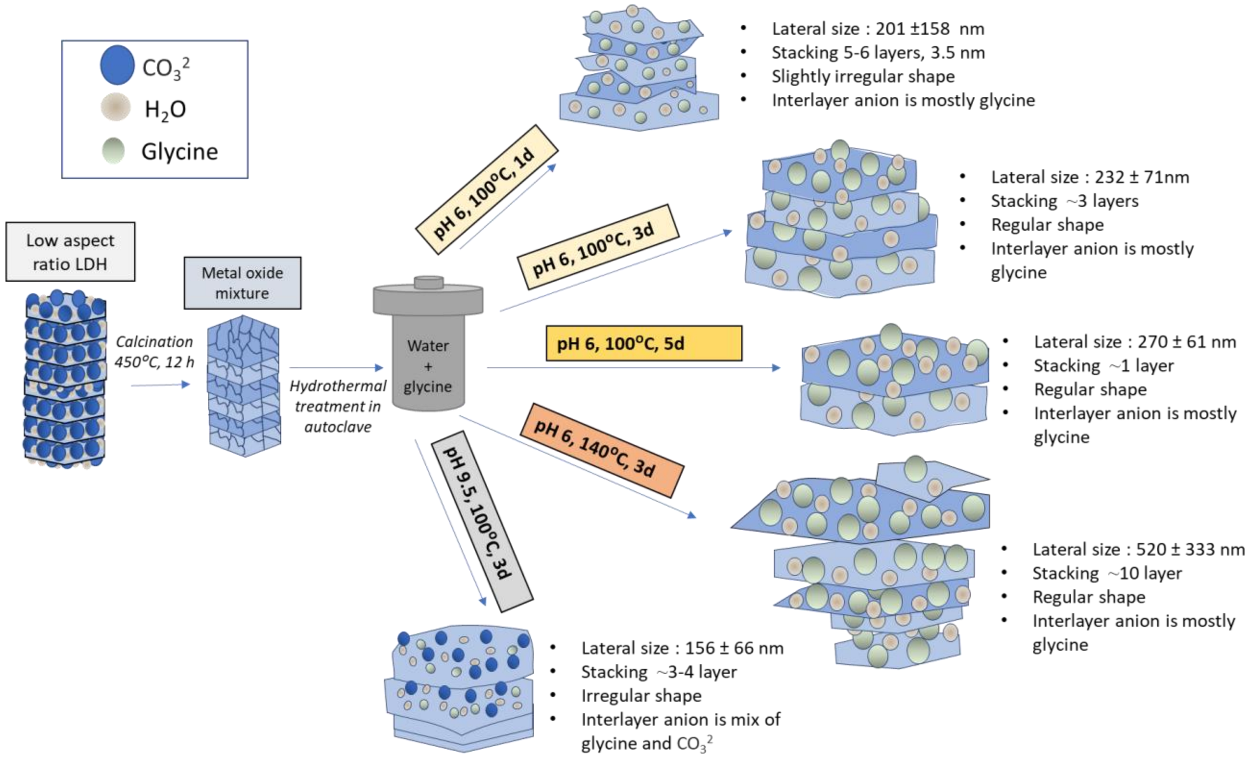

Figure 4.2 Illustration of the effect of hydrothermal treatment conditions on LDHs morphology, size, and stacking

Table 4.2 Morphological features and sizes of LDHs prepared through different conditions

Sample	d_{003} (nm)[a]	Lateral size TEM[b] (nm)	Hydrodynamic size DLS[c] (nm)	Lateral Size AFM[d] (nm)	Thickness AFM[d] (nm)	Aspect ratio AFM[d]
9.5-100-3d	0.762	156 ± 66	792 ± 32	113 ± 23	1.97 ± 0.43	57 ± 13
6-100-3d	0.782	232 ± 71	517 ± 4	238 ± 63	1.8 ± 0.6	132 ± 35
6-140-3d	0.756	520 ± 333	673 ± 43	315 ± 152	10.5 ± 3.5	29.5 ± 5.3
6-100-5d	0.761	270 ± 61	2125 ± 321	162 ± 20	0.8 ± 0.06	200 ± 22.9
6-100-1d	0.757	201 ±158	460±18	82.2 ± 24.2	3.5 ± 2.1	20.5 ± 3

a *d* (003) spacing is calculated from the position and half-width of reflections (003) using the Bragg diffraction formula **b** LDH lateral sizes were calculated from TEM images **c** Hydrodynamic size of LDH in water measured through DLS **d** lateral size, thickness, and aspect ratio. The aspect ratio was calculated by lateral size divided by the thickness of individual particles from AFM measurements of samples at more than 8 different spots.

4.3.2 The Effect of pH

To assess the influence of initial pH on the morphology, size, and aspect ratio of LDH, we conducted LDH synthesis at two distinct pH levels: 6 and 9.5. Alterations in pH can impact LDH synthesis in two different manners: (i) by modifying the charge state of glycine, thereby affecting its stabilizing effect on LDHs, and (ii) by influencing the reconstruction process of LDHs (involving hydration, re-crystallization, and dissolution stages) due to changes in the concentrations of pre-LDH species.

The calculated d_{003} values for LDHs synthesized at initial pH 6 and pH 9.5 were 0.782 nm and 0.762 nm, respectively (Table 4.2). At pH 9.5, the formation of OH^- and CO_3^{2-} anions is highly possible within the system, and glycine competes for intercalation into LDH with these anions [70]. This competition may lead to a reduction in the amount of glycine incorporated within LDH sheets, consequently decreasing the interlayer spacing for the 100_9.5_3d sample [134]. Conversely, the formation of OH^- and CO_3^{2-} anions was hindered under acidic conditions (pH 5.9), allowing glycine to intercalate into LDH sheets readily [70, 130]. Therefore, the d_{003} is higher under these conditions.

In the case of 100_6_3d, we obtained LDH particles with a regular hexagonal shape, as observed in the TEM image (Figure 3b), with lateral dimensions of 232 ± 71 and exhibiting a narrow particle size distribution. The LDH sheets displayed remarkably homogeneous contrast in the TEM image, indicating their ultrathin nature and uniform thickness. Under these conditions, most glycine molecules exist in a zwitterionic state, allowing them to stabilize the pre-LDH sheets through electrostatic interactions or hydrogen bonding [135]. At pH 9.5, the stabilizing effect of glycine via hydrogen bonding and/or electrostatic interactions decreases as amine groups become deprotonated. This results in a higher disorder in the 100_9.5_3d sample (Figure 3c) [136]. Rheological measurements supported these observations. We noticed a more significant increase in complex viscosity for 100_6_3d at lower frequencies than 100_9.5_3d (Figure 4.2a). This is attributed to the higher number of hydrogen bonds formed among glycine, LDH layers, and interlayer water molecules at lower pH. These hydrogen bonding and electrostatic interactions were further confirmed through FTIR analysis, where a shift in the asymmetric vibration of the COO^- group to an orthogonal position (Figure 4.2c) was observed [33, 132, 133].

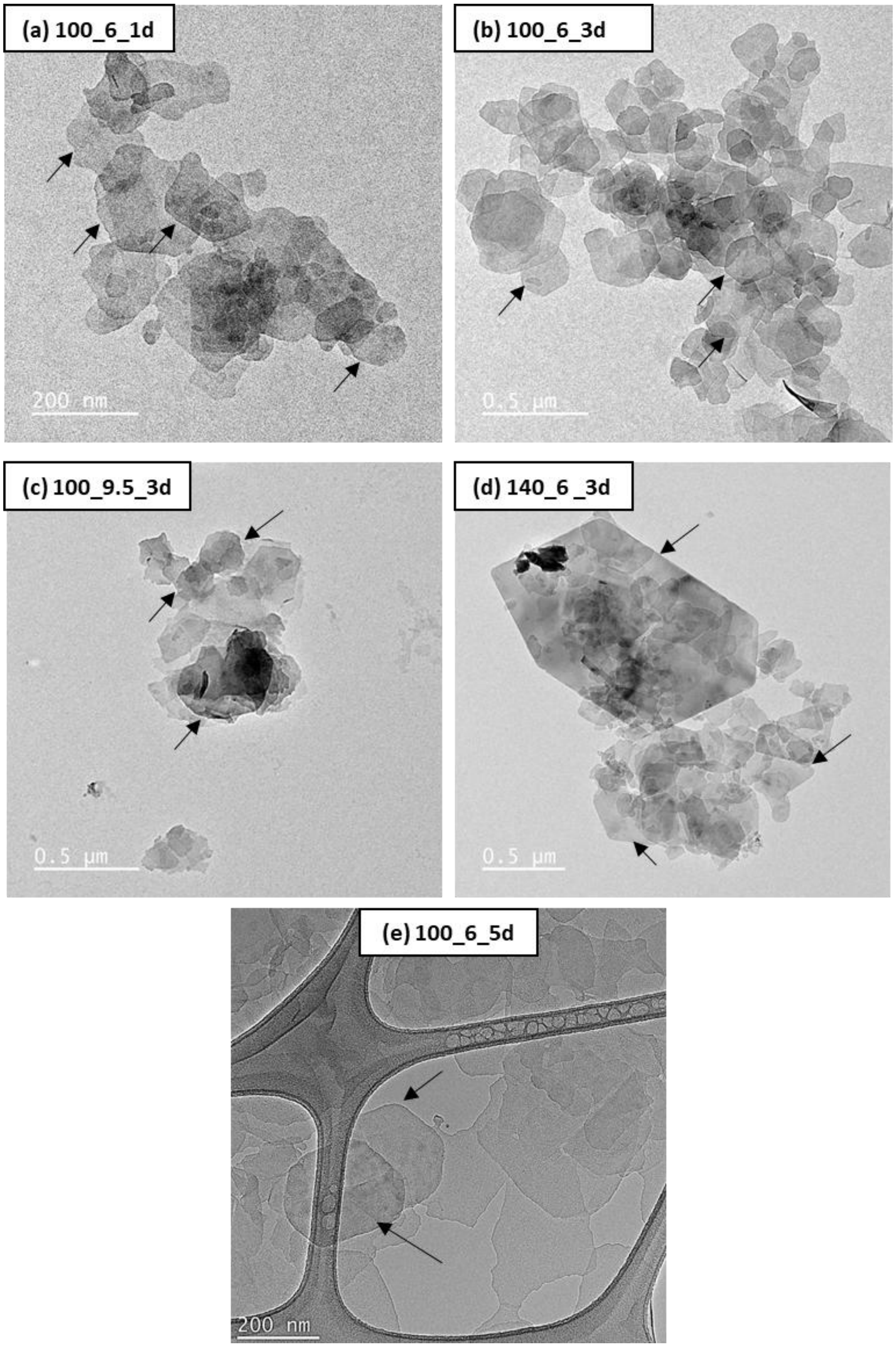

Figure 4.3 TEM images of the LDHs synthesized in different hydrothermal treatment conditions: (a) 100_6_1d (b)100_6_3d (c) 100_9.5_3d (d) 140_6_3d (e)100_6_5d. Lateral dimensions calculated through TEM images are listed in Table 4.1.

In the 100_9.5_3d sample, the size distribution remains narrow, with an average lateral size of 156 ± 66 nm calculated from TEM images (Figure 4.3c), while it measures 232 ± 71 nm for 100_6_3d

(Figure 4.3b). This slight size difference concerning pH was attributed to variations in nucleation and recrystallization pathways, as well as changes in the concentrations of $Mg(OH)_2$ and $Al(OH)_3$ at different pH values (Table S1) (Figure S4.2 and Figure S4.3) [70].

These observations are consistent with AFM scanning results (Figure 4.4), where well-defined hexagonal shaped (lateral size of 238 ± 63 nm) with a smaller thickness (1.7 nm, corresponding to 2-3 LDH layers) of LDHs were observed in 100_6_3d. The aspect ratio increases from 57 ±13 to 132 ±35 with the decrease in initial pH to 5.8 (Table 4.2), indicating an apparent pH-dependent effect on the morphology and dimensions of the LDHs.

We calculated the crystallite sizes in the *c-axis* (stacking direction) using the Scherrer equation (Table S4.2). The crystallite size increased in the *c-axis*, from 12.7 nm to 13.8 nm, with an increase in pH from 6 to 9.5. This observation supports the notion of enhanced LDH sheet stacking at higher pH values. Besides the influence of interlayer anions, differences in charge density can also affect LDH stacking in the *c-axis*. At higher pH levels, the charge density of LDH is higher (low Mg/Al ratio), promoting stronger LDH-interlayer anion interactions and this strong interactions can facilitate easier stacking in the c-axis [121, 137]. Hence, we can say that the stacking of LDH was not solely governed by the presence of glycine. A similar effect, albeit to a lesser extent, can also be observed even in the absence of glycine. To demonstrate this, we conducted a hydrothermal treatment using only deionized water and layered double oxide (LDO) at two different pH levels (6 and 9.5). We discovered that a higher pH level of 9.5 led to a more significant growth in LDH crystal in the *c-axis* stacking direction (Figure S2). At pH 9.5, the formation of CO_3^{2-} anions is facilitated, and these anions can be readily absorbed at the surface of positively charged hydroxide layers[70]. These absorbed CO_3^{2-} anions, with high binding capacity, provide a platform for the generation of the next layer of LDH, resulting in the formation of more stable LDHs with larger thicknesses [70, 138, 139]. In contrast, at a lower pH of 6, CO_3^{2-} formation was limited and Cl^- ions with lower binding capacity were intercalated, leading to reduced stacking but similar lateral sizes at the same hydrothermal treatment time and temperature [139]. The intensity of CO_3^{2-} in the FTIR spectrum (Figure S4.1) was higher at high pH, confirming increased CO_3^{2-} absorption [70].

4.3.3 The effect of temperature

The temperature during the hydrothermal treatment significantly impacts both the kinetics of particle formation and the thermodynamic stability of the resulting particles. In this study, we synthesized LDHs (in aqueous glycine) at two different temperatures: 100 °C and 140 °C. First, increasing the temperature from 100 °C to 140 °C decreased the basal spacing of d_{003} from 0.782 to 0.756 nm (Table 4.2). A previous study by Nakayama et al. [125] showed that the uptake of amino acids within LDH layers does not change with increasing the temperature of the reaction. Therefore, we believe that the change in the amount of interlayer water molecules and/or the change in the orientation of glycine molecules within LDH layers caused a shift in d_{003}. Similar findings were reported by other researchers, who attributed the changes in d_{003} to the rearrangement of interlayer anions due to the dehydration of LDH [65, 140].

In terms of lateral dimension, we started to see a larger size distribution (the diameter varied from 200-900 nm) at 140 °C (Figure 4.3), which means that hydrothermal treatment at higher temperatures led to the growth of the LDHs while dissolution was also faster [141, 142]. Also, the stacking of the LDHs led to an increase in the thickness; thus, the aspect ratio of LDHs became lower (29.5 ± 5.3) at 140°C. At higher temperatures, the dielectric constant of aqueous glycine solution is reduced [135, 143], so its effect on the stabilization of LDH layers was diminished, and this might have caused further irregularity and stacking in LDHs. Rheological results were consistent with this finding; the complex viscosity upturn at lower angular frequencies was smaller in 140_6_3d compared to 100_6_3d (Figure 4.2b). We also observed a lower shift in the asymmetric vibration of the COO^- group of glycine with increasing hydrothermal temperature, which might be an indication of less extent of hydrogen bonding and electrostatic interactions (Figure 4.2c) [133]. Also, the ζ-potential of 140_6_3d was slightly lower than that of 100_6_3d. The results of Sun et al. [136, 144] support our findings by showing that when the hydrothermal treatment temperature exceeds 90°C, it speeds up Ostwald ripening, and this acceleration leads to significant differences in LDH particle sizes over time. Additionally, they reported an agglomeration of LDHs under higher temperatures, confirming our results regarding increased stacking with increasing temperature. The elevated temperature also caused changes in the composition (Mg/Al ratio) of growing particles due to the varying reprecipitation rates of divalent and trivalent cations (Table 4.1).

4.3.4 The effect of reconstruction time

The duration of hydrothermal treatment is a crucial parameter, as it can favor kinetically stable phases in short-term processes, whereas thermodynamically stable phases are typically formed in long-term experiments. This phenomenon can be attributed to the re-dissolution and recrystallization of already-formed phases.

As the reconstruction time increases, larger crystallites grow at the expense of smaller ones, a process commonly known as Ostwald ripening, as mentioned in the previous section. This behavior becomes more prominent with prolonged time (Figure 4.1). In our observations, TEM images revealed an increase in LDH lateral size from 201 ±158 nm to 270 ± 61 nm with a reconstruction time increase from 1d to 5d (Figure 4.3). Additionally, the hydrodynamic size of LDHs increased from 460 ±18 nm to 2125 ± 321 nm as the duration extended from 1d to 5d (Table 4.1).

We also investigated the influence of reconstruction time on the stacking of LDHs. AFM images (Figure 4.4) demonstrated a decrease in LDH thickness from 3.5 ± 2.1 nm to 0.8 ± 0.06 nm as the hydrothermal treatment duration increased from 1d to 5d (Table 4.2). The observed reduction in LDH stacking indicates improved hydrogen bonding between glycine and LDHs as the reconstruction time increases. This can be confirmed by a larger shift in the asymmetric vibration of the COO^{-}group of glycine as the reconstruction time increases from 1d to 3d. (Figure 4.2c). Rheological analysis further supported this observation, revealing a more significant complex viscosity increase with longer reconstruction times. The aspect ratios for LDHs prepared through 1d, 3d, and 5d reconstruction times were calculated as 23.4 ± 5, 132 ± 35, and 200 ± 22.9 (Figure 4.4, Table 4.1, and Table 4.2), respectively. This trend aligns with previous research findings by Yu et al. [69] who showed that prolonged reconstruction times led to increased glycine concentration in the confined interlayer region that helped reduce the stacking of LDH layers.

Our XRD results also suggest that increasing time can slow the stacking in the c-axis; the crystallite size in the c crystallographic direction was calculated as 18.8 nm and 9.1 nm for 1d and 5d reconstruction time, respectively (Table S4.2). These results emphasize the dynamic nature of LDH stacking and its interaction with glycine, which are significantly influenced by the duration of the hydrothermal treatment process. Finally, the ζ-potential values were +24 mV, +28.1 mV, and +29 mV for LDH obtained for 1d, 3d, and 5d, respectively.

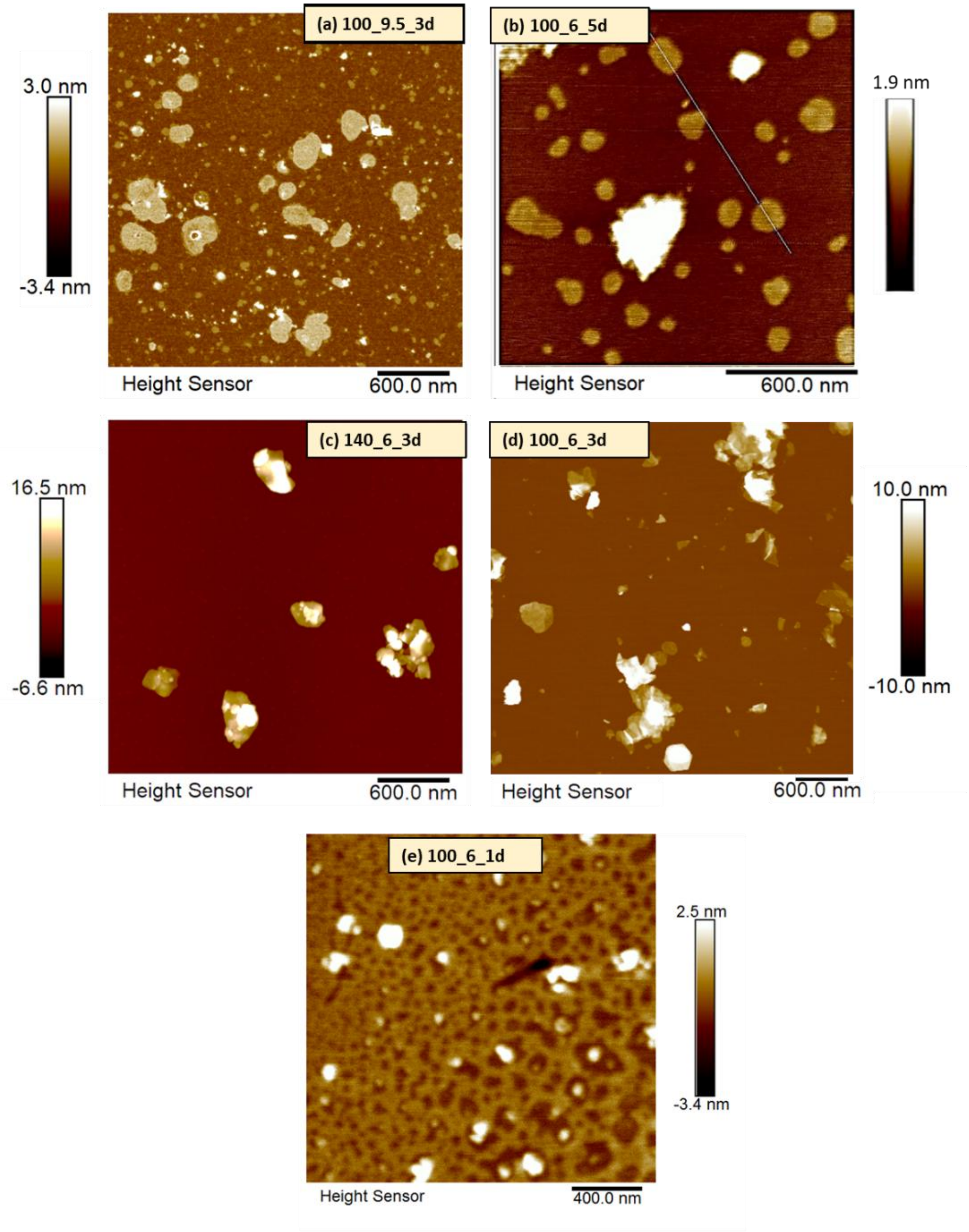

Figure 4.4 AFM measurements of the LDHs synthesized in different hydrothermal treatment conditions. (a) 100_9.5_3d (b) 100_6_5d (c) 140_6_3d (d)100_6_3d (e)100_6_1d . Aspect ratios calculated through AFM images are listed in Table 4.1

4.3.5 Oxygen permeability of LDHs

Based on the classical gas permeability models, the content, aspect ratio, and orientation of platelet-shaped inorganic fillers are the critical factors in determining the gas transmission properties of the composite films [145, 146]; that is, the more significant aspect ratio and the higher orientation of the 2D inorganic platelets are favorable to the barrier properties. In this context, we coated PET films with LDH/glycine gels -prepared through different hydrothermal conditions - to show the effects of aspect ratio. Table 3 shows the OTR results for PET/LDH coatings. The pristine corona-treated PET substrate shows a high OTR of 129 cc /m^{2}day, indicating its low oxygen barrier. Corona treatment oxidized the surface of PET and created phenolic modifications that can impart a strong negative charge[147, 148] without compromising PET bulk properties. This treatment is well-known to enhance the interaction of high surface energy (e.g., water-based) materials with the substrate surface. As LDHs are positively charged and corona treated-PET is negatively charged, we were able to produce durable LDHs coating on PET (Figure S4.4). The coating of the PET film with LDHs reduced the PET oxygen permeability, and the LDH with higher aspect ratios had a more pronounced effect than the lower aspect ratio LDHs. This is because the tortuous pathway increased with increasing aspect ratio, so a longer time is required for oxygen molecules to diffuse through the coating. A 99.98% reduction was observed in OTR upon coating PET with 100_6_3d. The final OTR values (0.039 and $0.041\text{x}10^{-16}\text{cm}^3\text{(STP)}\cdot\text{cm}\cdot\text{cm-}^{2\cdot}\text{s}^{-1}\cdot\text{Pa}^{-1}$) are comparable to commercial metalized PET films [149] and lower than the values reported in the literature for different types of nanoparticle coatings on polymer films such as cellulose nanocrystal [150], SiOx [151], and graphene oxide [152] coatings.

Table 4.3 OTR values of LDHs prepared through different hydrothermal treatment conditions.

Sample	**OTR** [cc·m^{-2}·day^{-1}]	**Coating Thickness** (nm)[a]	**O_2 permeability of coated barrier film [10^{-16}cm^3(STP)·cm·cm^{-2}·s^{-1}·Pa^{-1}]**
PET	129	-	19
PET/100-9.5-3d	0.76 ± 0.14	890	0.120
PET/100-6-3d	0.25 ± 0.13	950	0.039
PET/140-6-3d	0.52 ± 0.27	940	0.082
PET/100-6-5d	0.27 ± 0.22	454	0.041
PET/100-6-1d	0.95 ± 0.07	940	0.145

a Coating thickness was calculated using coating weight and density of LDH

4.4 Conclusion

This study aimed to enhance the understanding of synthesizing LDHs with high aspect ratios. We investigated the effects of hydrothermal treatment conditions, specifically focusing on initial pH, temperature, and reconstruction time on the aspect ratio of LDHs. We utilized an aqueous glycine medium to hinder the stacking of LDHs. Compared to pH 9.5, we found that higher aspect ratio LDHs were obtained at pH 6 due to the zwitterionic glycine providing better stability during the reconstruction. Moreover, varying the hydrothermal treatment temperature played an important role: applying higher temperatures led to the formation of larger crystals; however, stacking of LDHs was also promoted. For example, LDHs synthesized at 140 °C had smaller aspect ratios than those synthesized at 100 °C. Additionally, the relationship between aspect ratio and reconstruction time was straightforward: longer reconstruction time led to high aspect ratio LDHs. The oxygen permeability performance of LDHs synthesized by hydrothermal treatment coatings compared favorably to existing nanoparticle coating technologies. These findings offer a promising pathway for producing LDHs tailored for high-performance barrier coatings in flexible packaging and related industries.

4.5 Acknowledgments

The authors gratefully acknowledge the financial support of 3SPack NSERC Industrial Research Chair by the Natural Science and Engineering Council of Canada (NSERC) and ProAmpac Inc. Compa.

4.6 Supporting information

FTIR spectra of all LDHs and detailed information, calculation of concentrations of different pre-LDH species, calculation of crystal size and FWHM are reported in Appendix A

CHAPTER 5 ARTICLE 2 : ELECTROSTATICALLY COMPLEXED POLYVINYL ALCOHOL-LAYERED DOUBLE HYDROXIDE-TEMPO-OXIDIZED CELLULOSE NANOFIBER GAS BARRIER COATINGS

Emre Vatansever[1] Amir Saffar[1,2], Abdellah Ajji[1*]

1: 3SPack, Research Center for High Performance Polymer and Composite Systems (CREPEC), Chemical Engineering Department, Polytechnique Montréal, Montréal, Québec H3C 3A7, Canada

2: ProAmpac, Terrebonne, QC, Canada J6Y 1V2

**Corresponding Author, email: abdellah.ajji@polymtl.ca*

Submitted to Advanced Composites and Hybrid Materials on October 28, 2024

Abstract

In this study, we studied a synergistic effect of combining a layered double hydroxide (LDHs) with oppositely charged TEMPO-oxidized cellulose nanofiber (CNF) within polyvinyl alcohol (PVA). Sedimentation and rheological measurements revealed that the combination of oppositely charged LDH-TCNF nanoparticles within PVA created an interconnected network in the coating mixture. This hybrid PVA/LDH-TCNF dispersion was coated onto a polyethylene terephthalate (PET) substrate using a simple bar coating method. Hybrid coating demonstrated superior oxygen barrier performance compared to individual PVA/LDH and PVA/TCNF coatings. The enhanced barrier properties were primarily attributed to the interlocked PVA/LDH-TCNF network, facilitated by electrostatic interactions and hydrogen bonding, as confirmed by FTIR. Improved orientation (~90 %), enhanced stability, and reduced defects of LDH in the presence of TCNF further contributed to the reduced OTR of the coatings. The final PVA/LDH-TCNF coatings show a low oxygen transmission rate of 0.04 cc/m^{2}day, a 99.9 % reduction compared to PET. Additionally, these coatings retained transparency at ~89 % and maintained their oxygen barrier at 60 % relative humidity (~0.7 cc/m^{2}day) and after the Gelbo flex test (~1.2 cc/m^{2}day), making them appropriate for the flexible food packaging application while also offering recycling.

Keywords: Synergistic effect, layered double hydroxides, LDH, cellulose nanofiber, oxygen permeability, polyvinyl alcohol, flexible packaging, barrier coatings

5.1 Introduction

Water-based barrier dispersion coatings, known for their recyclable, non-toxic, and reliable barrier performance, have been considered potential substitutes for current high-barrier solutions such as lamination, metallization, fluorochemicals, and waxes. These water-based barrier dispersions can be polymers dispersible in water, such as polyvinyl alcohol (PVA), starch, cellulose derivatives, proteins, and latexes. In some applications, particularly those where humidity resistance and mechanical properties are the focus, barrier dispersions alone may not fully satisfy the performance needs. To address these needs and introduce additional functionality, nanoparticles are often added to barrier dispersions. Nanoclays are widely used for this purpose, offering improved barrier properties due to their lamellar structure and high aspect ratios [153].

Layered double hydroxides (LDHs), also known as hydrotalcite, have been shown to offer promising barrier performance in polymers [28, 33, 58, 69, 78, 112]. LDHs are a class of anionic clays consisting of inorganic sheets carrying positive charges with intercalated anions between the sheets. The general formula for LDH is $M^{2+}_{1-x}\ M^{3+}_{x}(OH)_2A_x\ nH_2O$ where M^{2+} represents metallic cations such as Mg^{2+}, Zn^{2+}+, Ni^{2+} and M^{3+}includes cations like Al^{3+}, Fe^{3+}, etc., and A denotes intercalated anion which can be CO_3^{2-}, Cl^-, OH^-, etc. The positive charge in LDHs results from the substitution of M^{2+}cations by M^{3+} cations. This positive charge is balanced by intercalated anions in conjunction with water. Such synthetic nanoclays are free from color contamination, possess homogeneous charge distribution, and may exhibit a wide range of morphologies, sizes, and aspect ratios [154].

However, like most nanoparticles, LDH aggregates within polymer matrices at higher concentrations or shows phase separation in polymer dispersions due to strong interactions among LDH layers [72]. To stabilize particles in a well-dispersed state, it is necessary to introduce repulsive forces, typically through electrostatic or steric repulsion [155]. Stabilization of micro/nanoparticles (or pigments) through oppositely charged components (e.g., polymer dispersants or surfactants) has been employed in the coating industry for decades. A typical example is using anionic polyacrylate to achieve uniform dispersion of calcium carbonate or kaolin pigment particles. However, these dispersants may deteriorate the interaction between particles and desired substances [156] or may cause pinholes or irregularities in the coating [157, 158]. A more recent approach involves adding secondary nanoparticles to improve the dispersion and stability of primary nanoparticles. Unlike surfactants or polymer dispersants, secondary nanoparticles can also provide additional functionalities to the coating system, such as better processability, thickening, water retention, sealability, flexibility, and antibacterial properties [159-162]. Several studies have explored the effects of negatively charged molecules on stabilizing positively charged LDHs. For instance, Kang et al. [72] reported that carboxymethyl cellulose could stabilize LDH in water, preventing the re-agglomeration of LDHs. In another study [41], LDH was combined with a series of different 2D nanosheets, such as graphene oxide (GO), boron nitride, and molybdenum disulfide, based on the concept of electrostatic interactions. It was shown that the oxygen barrier properties of PVA show a 25-fold improvement upon GO-LDH addition, while the electrical conductivity and gas selectivity of nanocomposites also improved.

Nanocellulose materials such as cellulose nanofiber (CNF) and cellulose nanocrystals (CNC) have been utilized in the development of high-barrier films and coatings [23-26, 163]. Their biobased, biodegradable nature and mechanical and optical properties comparable to conventional materials make them good candidates for packaging applications. The polyanionic nature of CNF, thanks to the presence of carboxylic groups, enables it to form hybrid complexes with positively charged materials. Various types of nanocellulose-based hybrid systems are used in literature to improve the dispersion and stabilization of graphene [164], clay [165], or other nanoparticles [166]. One study highlighted that TEMPO-oxidized CNF is an effective dispersant for kaolin, providing better stability than commercial sodium polyacrylate dispersants and offering a water retention functionality [165].

Herein, we aim to develop PVA-LDH-CNF dispersion for high-barrier coating applications. We used PVA as a matrix, a polymer known for its potential for sustainable coatings thanks to its biodegradability, non-toxicity, excellent film-forming properties, and gas barrier properties. The LDH, selected for its unique layered structure, positive charge, and high aspect ratio, contributes additional gas barrier performance. TCNF is added to the mixture as the electrostatic interactions between LDH and the negatively charged TCNFs can contribute to the structural integrity of the coating dispersion but also create a synergistic effect that enhances the overall compatibility within the PVA matrix.

5.2 Materials and Methods

5.2.1 Materials and substrates

PVA (Mw=140 000 – 186 000 g. mol-1) was purchased from Sigma Aldrich. The positively charged LDH (DHT-4A), provided by Kisuma Chemicals, was further modified to obtain a high aspect ratio LDH. Cellulose nanofiber is surface modified via 2,2,6,6-tetramethyl-1-piperidinyloxy (TEMPO)-mediated oxidation and was purchased from the University of Maine (ME, USA).

5.2.2 Calcination and hydrothermal synthesis of LDH

High aspect ratio LDHs were synthesized using a calcination-rehydration approach. Initially, the LDH was calcinated at 500°C for 12 hours with a heating rate of 5°C/min. High aspect ratio LDH was prepared by mixing 2 g of calcinated LDH with 20 ml of aqueous glycine solution at a 1:1.5 (LDH:glycine) ratio. The mixture's pH was adjusted to approximately 6 and placed in a Teflon-lined autoclave. The autoclave was then heated at 100°C for 72 hours in an oven. The autoclave was then allowed to cool down to room temperature, and LDH gel was obtained. LDH was washed with DI in centrifugation to remove impurities before adding to coating formulations.

5.2.3 Preparation of coating dispersions and application on PET

PVA was first dissolved in DI water for 2h at 90 °C with constant stirring. When PVA was used alone, the total solid content was 5 wt% with respect to the aqueous phase. Prepared high aspect ratio LDH gel was diluted to 5 wt% and dispersed in deionized water by using ultrasonication for 180 sec using an ultrasonic probe (Cole-Parmer) at 30 W. Similarly, 2 wt% of TCNF in DI water prepared by using magnetic stirrer for 2 h at 80 °C and then by using ultrasonication for 180 sec at 30 W. To prepare PVA/LDH or PVA/TCNF, those well dispersed LDH or TCNF added in PVA slowly and mixed for 3 hour using magnetic stirrer at 80°C. To prepare a hybrid PVA/LDH-TCNF mixture, we first mixed LDH-TCNF briefly using a magnetic stirrer, and then this mixed LDH-TCNF hybrid was added to PVA and stirred for 3 hours through a magnetic stirrer. The solid contents and formulations of the coating dispersions are summarized in Table S1. These coating dispersions were then applied to a 13 μm thick freshly corona-treated polyethylene terephthalate substrate. An automatic coater (TQC Sheen AB4120) equipped with a Mayer rod was utilized for the application process. Approximately 3 mL of the prepared coating mixture was deposited on the substrate. The Mayer rod moved at a controlled speed of 100 mm/s, forming a coated film. All coated samples were air-dried at room temperature. The coated films were conditioned at a controlled environment of 25 °C and 50 % relative humidity (RH) for 48 h before any analysis.

5.2.4 Coating weight, film thickness, and microstructure

Coating weights were determined by subtracting the weight of the uncoated PET films from that of the coated PET films. We used three different ways to measure the coating thickness. First, the coated film thickness was measured using an automatic deadweight micrometer (ProGage Touch Thickness Tester, Thwing-Albert Instrument, USA), with a sensitivity of 0.01 mm, and reported as an average of at least three measurements. We also used scanning electron microscopy (SEM, JSM 7600F, JEOL, operated at 5kV accelerating voltage) to measure coating thickness. To do this, films were prepared using a single-edged razor blade cleaned with ethanol before being used for cross-section analysis.

Another method to examine the overall film thickness is by calculating the coating weight and density of the coatings. The total thickness of the film is then calculated using equation 5.1

$$d_{total} = d_{PET} + \left(\frac{\Delta m}{\rho . S}\right) \tag{5.1}$$

where d_{PET} is the thickness of the PET substrate, Δm (g) is the weight difference between after and before coating the film, ρ (g/mL) is the calculated density of the coating, and S (cm^2) is the surface area of the film, which was 5 cm × 5 cm for all films. Coating weights and thicknesses were obtained through different approaches listed in Table S2.

5.2.5 Zeta Potential and Dynamic Light Scattering (DLS) Measurements

The zeta potential, hydrodynamic size, and colloidal stability of the dispersed LDH and TCNF particles were determined using a Nano ZS Zetasizer at 25 °C. The concentration of nanoparticles in water was approximately 0.05 wt.%. Five runs were conducted for each sample, and the data were analyzed using the Smoluchowski model. An average of three measurements was obtained for each sample, and the mean value was reported. It is important to note that Dynamic Light Scattering (DLS) and zeta potential methods are designed primarily for spherical particles and may not be suitable for non-spherical shapes, such as hexagonal or fibrillar structures. Therefore, we employed these methods mainly for a preliminary evaluation of the nanoparticles' size, charge, and adsorption properties rather than focusing on the precise size and surface charge values.

5.2.6 Rheological measurements

The rheological behaviors of coating dispersions were analyzed using a rotational rheometer (Anton Paar, MCR501, Germany). Rheological tests were conducted with a concentric cylinder. Frequency sweep tests were performed, ranging from 100 to 0.1 rad/s. Before each test, coating mixtures were pre-sheared to eliminate air from the sample and ensure a consistent starting microstructure. All tests were carried out at 25°C.

5.2.7 Attenuated total reflection-Fourier transform infrared (ATR-FTIR)

ATR-FTIR analysis was conducted using a PerkinElmer 65 FTIR spectrometer (Woodbridge, ON, Canada) in attenuated total reflection (ATR) mode. Spectra were acquired in the 600 – 4000 cm^{-1} range, comprising an accumulation of 36 scans with a resolution of 4 cm^{-1}. For crystallinity measurements, we used the following equation:

$$x_c(\%) = a + b\left(\frac{I_c}{I_a}\right) \qquad (5.2)$$

where a and b are correlation coefficients. For PVA, the values of these coefficients are assigned as −13.1 and 89.5, respectively[167]. I_c and I_a are the IR absorbance intensities of peaks corresponding to the crystalline phase at a wavenumber range of 1140–1145 cm^{-1} and the amorphous phase at a wavenumber around 1090–1096 cm^{-1}, respectively[167].

5.2.8 Transmission Electron Microscopy (TEM)

Electron microscopic images were acquired utilizing a JEOL JSM-6400F (Japan) field emission scanning electron microscopy, operated at 200 kV. To prepare LDH, a droplet of the LDH-containing suspension (0.01 wt%) was deposited onto a TEM grid, allowed to dry, and sputtered with platinum before imaging. To prepare TCNF samples, we positively charged the TEM grids in the Pelco Glow Discharge Cleaning System. Then, drop cast 0.1 wt% TCNF in water on grids and negatively stained using uranyl acetate.

5.2.9 Scanning Electron Microscopy (SEM)

The morphology and cross-section of various samples were observed with a field-emission SEM (FE-SEM) machine (JSM 7600F, JEOL), operated at 15kV accelerating voltage. Surface test samples were mounted on stubs with carbon tape. Cross-sectioned samples were prepared, as mentioned in 5.2.4.

5.2.10 Atomic Force Microscopy (AFM)

LDH and TCNF sizes were also measured using a NanoScope MultiMode AFM in tapping mode, utilizing a silicon tip coated with aluminum with a force constant of 40 N.m^{-1}. Aqueous LDH and TCNF samples were diluted to approximately 0.005 wt% and deposited onto freshly cleaved mica wafers for AFM imaging.

5.2.11 UV-vis Optical properties

The UV–Visibility spectra of the coated samples were recorded using a UV–Vis spectrophotometer (Lambda 900, PerkinElmer)

5.2.12 X-ray powder diffraction (XRD)

X-ray powder diffraction (XRD) analysis was conducted using a PANalytical X'Pert Pro diffractometer operating in diffraction mode, with a voltage of 40 kV and a current intensity of 40 mA, utilizing Cu-Kα radiation (λ = 1.5406 Å). For the analysis, coating dispersions were coated onto a silicon wafer, dried at room temperature, and placed into the sample holder. Data was collected over the 2θ range from 3 to 70° at a scanning rate of 0.08°/s.

The same XRD was used for pole figure measurements. PVA/LDH and PVA/LDH-CNF are separate films prepared on a Si wafer using a similar coating procedure to hinder any uncertainty that could be raised from the PET substrate. They were then mounted on a glass slide using double-sided tape and oriented so that at rotation angle, φ = 0° the top of the sample. A series of φ scans (rotation of the sample about the surface normal) made at several different ψ angles (sample tilt angle). Each φ scan was from 0 to 360° with a 2° step size and a counting time of 5 s per position. A phi scan was made every 3° from 0 to 26° in ψ. For each sample, pole figure measurements were made with the detector fixed at 11.7° in 2θ to ensure the diffracted intensity. The degree of orientation is calculated by using the Equation 5.2

$$\Theta = \frac{180 - FWHM}{180} \tag{5.3}$$

where ϴ is the degree of orientation, and FWHM is a full-width half maximum calculated by pole figure measurements.

5.2.13 Gas permeability measurements

MOCON OXTRAN 2/21 (Minneapolis, USA) apparatus was used to measure the permeability of oxygen at 0% relative humidity, 23 °C, and 1 atm pressure, as described in the ASTM standard, D-3985-81 and ASTM F1927 standards to prepare 5 cm^2 samples. A temperature of 23 °C and a humidity of 0 % RH were maintained on both sides of the sample. The same tests were conducted at 60% RH to investigate the effect of RH on coatings. The oxygen transmission rate (OTR) ($cc \cdot m^{-2} \cdot d$) was converted to oxygen permeability (OP) [$cm \cdot \mu m \cdot m^{-2} \cdot d \cdot atm^{-1}$] to compare the oxygen barrier performance of different films with different coating layers and different coating technologies exist in the market and literature. The measurements were performed at least in 3 duplicates.

Water vapor permeability of the films (Mocon, Permatran-W 101K) was measured following ASTM F 1249-90 standard at 23°C and 50 % RH. Data were recorded as water vapor transmission rate (WVTR) in g/m^2.day unit.

5.2.14 Mechanical Flex of the Films

All coated films were flexed 100 times using a Gelbo flex tester (IDM Instruments) following a modified ASTM F392–93 version. The films were conditioned at 23 ± 2 °C and 50 ± 5 % RH for 48 h before the flex.

5.3 Results and Discussion

5.3.1 Morphology, surface charge, and colloidal stability of LDH, TCNF, and PVA

The basic structural and charge properties of LDH and TCNF were first characterized. To increase the aspect ratio of LDH, LDH was reconstructed using glycine (Fig. S5.1a). After reconstructing LDH in aqueous glycine, a gel-like product was obtained. This gel-like LDH was diluted and subsequently dispersed using ultrasonication. XRD graph (Figure S5.1) highlighted distinct LDH structures with sharp and symmetric peaks at lower 2θ angles of 11.6° and broader, asymmetric peaks at higher 2θ of 23° and 61°. The TEM micrographs (Figure 1a) show that LDHs appear as hexagonal platelets with an average lateral size of 232 ± 71 nm, and the aspect ratio was calculated as 132 ± 35 nm through AFM images (Figure S5.2a and Table S5.1). LDH suspensions exhibited a positive zeta potential of +35 mV and hydrodynamic size of 517 ± 4 nm.

TCNF aqueous dispersion (1 wt. %) exhibited a gel-like structure with high viscosity, attributed to hydrogen bonding and network structure among nanocellulose fibrils. The hydrodynamic diameter was measured as 501 ± 48 nm using DLS. The zeta potential of TCNF was measured as -49 mV, resulting from the oxidation of reaction sites. Through TEM images (Figure 5.1b), the average width and length of TNCF were measured as 4.4 ± 0.7 nm and 276 ± 111 nm, respectively.

The effect of TCNF and PVA on LDH stability was investigated through a sedimentation study. Figure 5.1 shows sedimentation images after two months of three aqueous dispersions: 1 wt.% LDH (Figure 5.1c), 0.5 wt.% LDH mixed with 0.5 wt.% TCNF (Figure 5.1d) and 4wt% PVA mixed with 1 wt% of CNF-LDH (Figure 5.1e). LDH particles showed significant sedimentation in water after two months (Figure 5.1c). In contrast, the combination of cationic LDH within anionic TCNF reduced LDH sedimentation in water due to the H-bond and electrostatic interactions (Figure 5.1d)[168, 169]. Previous studies also reported that the fibrillar network formed by CNF throughout the mixture can limit particle movement and counteract gravitational effects [165, 170]. Adding PVA further hindered LDH sedimentation in PVA/LDH-TCNF dispersion (Figure 5.1e). This enhanced stability was attributed to the PVA stabilizer role for LDH-CNF hybrids through steric stabilization. The hydrodynamic particle size (Table S6.1) increased in PVA/LDH-TCNF (~1670 nm) compared to PVA/LDH (~920 nm) and PVA/TCNF (~1049 nm), suggesting physical adsorption among the components facilitated by H-bond and electrostatic interactions. These observations confirmed that both PVA and TCNF play crucial roles in preventing the agglomeration of individual clay particles [165]. The final zeta potential of PVA/LDH-TCNF was measured as +10 mV.

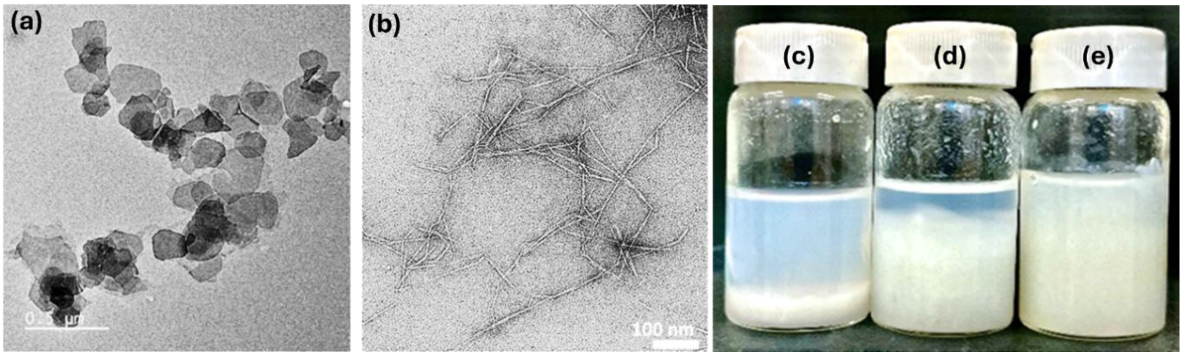

Figure 5.1 TEM image of (a) high aspect ratio LDHs prepared using calcination-rehydration method, scale bar 0.5μm. (b) TEMPO-oxidized CNF, scale bar 100 nm. Sedimentation of LDH (c) in water, (d) in TCNF, and (e) in PVA-TCNF. Sizes of LDH and TCNF measured through TEM are listed in Table S5.2.

5.3.2 Rheology, interaction, and microstructure of coating dispersions

The rheology of coatings is a critical factor that influences the coatability, uniformity, thickness, and structure of the final coating layer. These characteristics are determined by the various interactions within the coating dispersion system, such as polymer-polymer, polymer-filler, and filler-filler interactions. We carried out frequency sweep tests to explore these possible interactions and the microstructure of prepared coatings. Figure 5.2b shows complex viscosity (η^*) versus angular frequency (ω) and storage modulus (G') versus ω graphs of PVA/LDH, PVA/TCNF, and PVA/LDH-TNCF coating mixtures with %5 solid content in water. PVA alone showed a liquid-like Newtonian behavior, which could be originated from feeble interactions and low PVA concentration in water (Figure 5.2a). Regardless of the formulation, PVA nanocomposite mixtures (PVA/LDH and PVA/TCNF) exhibited shear-thinning behavior where gradual increases in η^* were observed as ω decreased. For PVA/TCNF, the upturn in η^* and G' at lower ω can be attributed to intermolecular interactions between PVA and TCNF as well as TCNF network structure within PVA. At higher ω, interactions among TCNFs and PVA might be disrupted, leading to a decrease in η^* of coating dispersion. Similarly, due to hydrogen bonding between LDH and PVA chains, we observed an increase in η^* at a lower frequency in PVA/LDH.

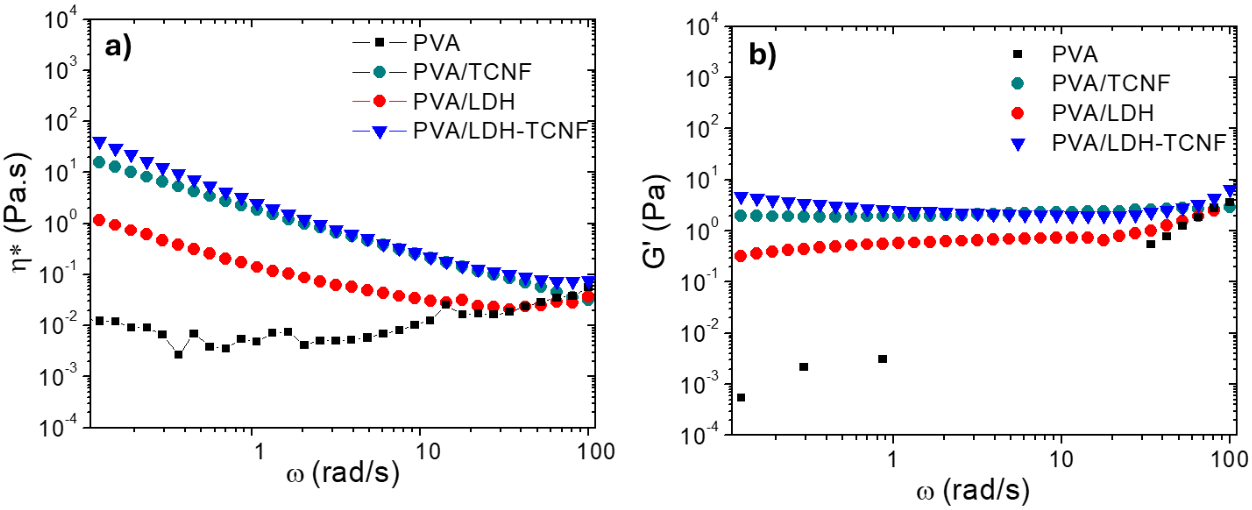

Figure 5.2 Rheological test results of (a) η* vs ω and (b) G′ vs ω. An increase in η* and G′ at low ω region indicates the formation of network structure.

The PVA-LDH-TCNF hybrid exhibited a more pronounced η* upturn at lower ω compared to PVA/LDH or PVA/TCNF. Hydrogen bonds and electrostatic interactions among LDH-TCNF and PVA contribute to forming a more rigid TCNF network even at lower nanoparticle concentrations

(0.5 wt%) in this hybrid dispersion [171-173]. A similar trend was observed in G' (Figure 5.2b), where the formation of a network among PVA-LDH-TCNF increased G' at low ω [174]. This more significant G' increase means higher stress levels are required to deform the PVA/LDH-TCNF hybrid dispersion than its individual PVA/LDH and PVA/TCNF dispersions due to the hydrogen bonding and electrostatic interactions between oppositely charged components, resulting in a stiffer network[173].

The possible microstructure and the interactions among LDH, TCNF, and PVA are schematically illustrated in Figure 5.3. The TCNF fibrils (depicted in black) are negatively charged, while LDHs (depicted in blue) are positively charged with glycine intercalated between the layers. LDHs provide additional physical cross-linking/contact points and play a bridging role in forming a stiffer TCNF network, restricting the fibrils' movement under shear [175, 176]. Simultaneously, PVA (depicted in green) with its hydroxyl groups can interact with LDH and TCNF through hydrogen bond interactions, acting as a stabilizer and/or binder for these nanoparticles [177-179]. Consequently, an electro-sterically complex network is formed among PVA-LDH-TCNF. This behavior of hybrids has been reported in the literature for various hybrid systems such as TCNF-laponite [176], graphene-cellulose nanofiber [180, 181], LDH-alginate [182] and calcium carbonate-carboxyl methyl cellulose [183].

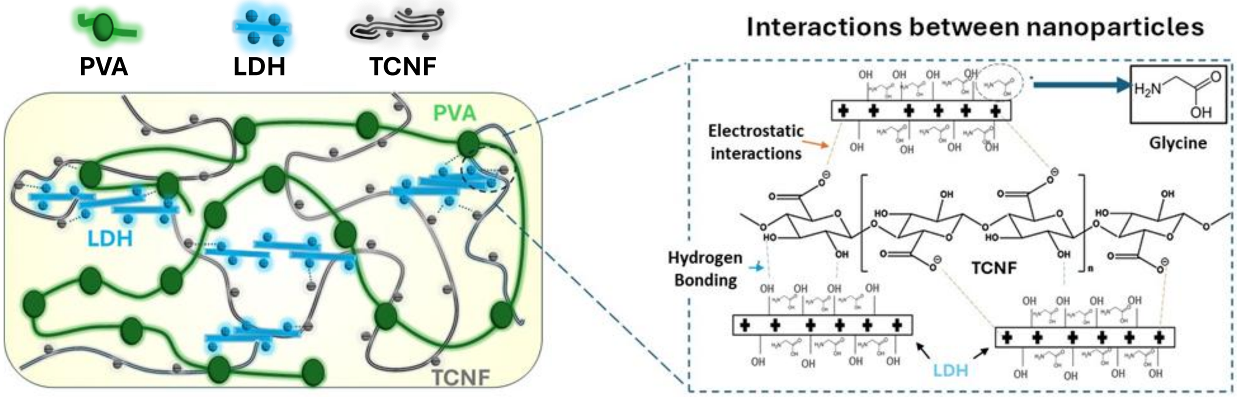

Figure 5.3 Bridge effect of LDH (colored blue) on TCNF (colored black) and PVA (colored green) and possible interactions between LDH-TCNF. The inset shows possible hydrogen bonds and electrostatic interactions between TCNF and glycine-intercalated LDH.

FTIR tests were conducted to validate these findings and results are presented in Figure 5.4 PVA/LDH, PVA/TCNF, and PVA/LDH-TCNF samples exhibited similar characteristics, with vibration band at 3260-3404 cm^{-1} (O–H stretching), 2915 cm^{-1} (C–H stretching), 1585-1577 cm^{-1}

(COO- asymmetric) 1334-1350 cm^{-1} (CH$_2$ wagging sym-metric bending), 1144-1131 cm^{-1} (C–O–C stretching), 1060 cm^{-1} and 1035 cm^{-1} (C–O stretching) [184, 185]. The COO$^-$ stretching bands at 1585 cm^{-1} in PVA/TCNF and at 1586 cm^{-1} in PVA/LDH, along with the NH$_3^+$ of glycine intercalated-LDH, merged into a new absorption peak at 1577 cm^{-1} in the PVA/LDH-TCNF sample. This confirms the formation of an electrostatically complex network in the PVA/LDH-TCNF system [173, 186, 187]. Some changes were also observed in O–H stretching bands within the 3260–3400 cm^{-1} range. O–H stretching band of PVA and PVA/TCNF shifted from 3263 cm^{-1} and 3262 cm^{-1} to 3350 cm^{-1} in PVA/LDH-TCNF, indicating the formation of hydrogen bonds among PVA/LDH-CNF. A decrease in the O–H stretching band intensity of PVA/LDH-CNF was observed compared to PVA/LDH and PVA/TCNF. Similar behavior observed by other researchers for CNF-nanoclay hybrid systems contributed to a reduction in CNF interfibrillar hydrogen bonding [173, 188].

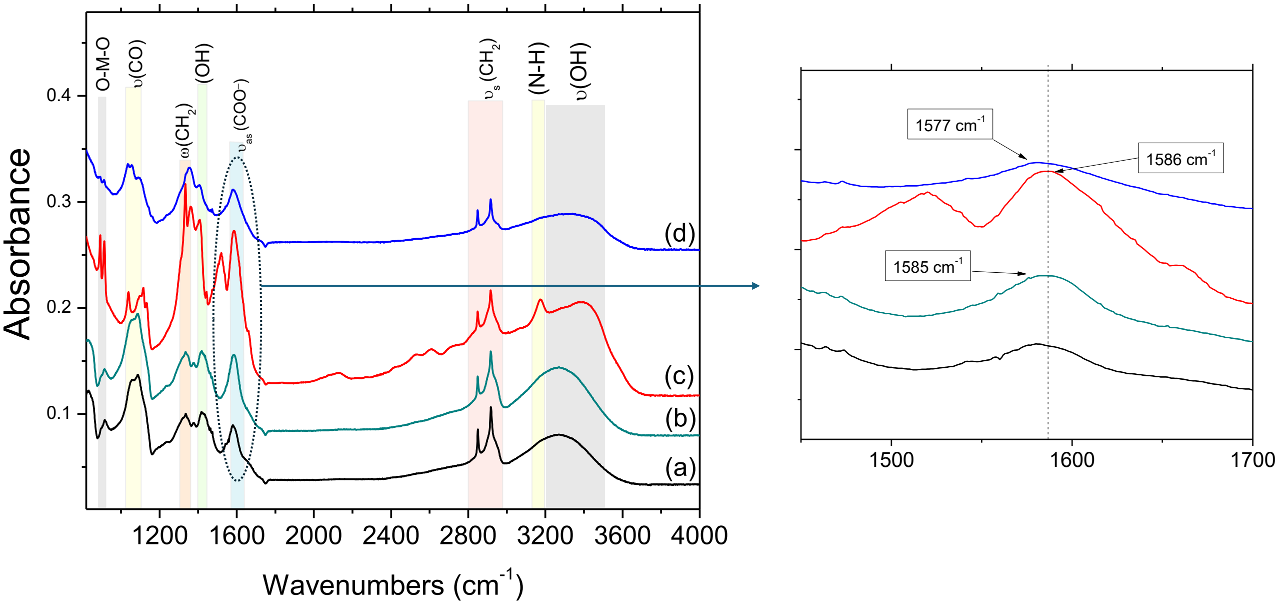

Figure 5.4 FTIR results of (a) PVA, (b) PVA/TCNF, (c) PVA/LDH (d) PVA/LDH-TCNF. Inset shows a blue shift in COO$^-$ stretching band, which can be due to the possible hydrogen bond and electrostatic interactions in PVA/LDH-TCNF.

We further calculated the crystal amounts through FTIR spectra using equation 5.2. The final crystallinity values were 60%, 65%, 72%, and 72.7% for PVA, PVA/TCNF, PVA/LDH, and PVA/LDH-TCNF hybrids. The results showed that both TCNF and LDH improved the crystallinity of PVA, however, the difference between PVA/LDH and PVA/LDH-TCNF was insignificant.

5.3.3 Morphological and structural characterization of coating films

XRD was used to evaluate the microstructure of coatings. The XRD patterns of PVA, PVA/LDH, PVA/CNF, and PVA/LDH/CNF are shown in Figure 5.5. The XRD pattern of the pure PVA revealed strong crystalline reflections at around 2θ = 19.92° and a shoulder at 22.74°. The two peaks are characteristic of PVA, representing reflections from (101) and (200) from a monoclinic unit cell [43]. We observed a reduction of intensity at 2θ = 19.92° with the addition of either LDH, CNF, or LDH-CNF. Vaezi et al. [189] reported that the interconnected structure of nanocellulose and nanoclay within a polymer matrix may reduce the intensity of any coherent diffraction peak from the matrix.

In the PVA/LDH sample, (003) and (006) diffraction peaks can be detected at 2θ of 11.8° and 23.6°, respectively, suggesting the presence of LDH within PVA (Figure 5.5c). The full exfoliation of LDH did not occur due to the high concentration of LDH inside PVA (i.e., wt%20 with respect to PVA) [190, 191]. In the PVA/TCNF sample (Figure 5.5b), we observed (110) planes of cellulose II at 2θ of 11.9°. Upon mixing of TCNF and LDH together within PVA (Figure 5.5d), the (003) peak of LDH (originally at 2θ = 11.86°) shifted slightly to a lower 2θ value of 11.73°. This slight shift could be attributed to the interaction between TCNF with intercalated glycine (within LDH interlayers) and/or the outer positively charged surface of LDH. These interactions may alter the orientation of intercalated glycine, thereby affecting the interlayer space of LDH.

The (003) peak of LDH in PVA/LDH-TCNF (Figure 5.5d) was slightly narrower compared to PVA/LDH (Figure 5.5c), suggesting that the presence of TCNF slightly improved the orientation of LDH within PVA [192]. To confirm this observation, we conducted a pole figure measurement. The results were plotted as a pole figure in which the contours indicate intensity as a function of sample orientation (Figures 5.5e and 5.5f). Although some anisotropic scatterings were observed in pole figures of both PVA/LDH (Figure 5.5e) and PVA/LDH-TCNF (Figure 5.5f), they were mostly centered around tilt (ψ) and rotation angle (φ) of 0°. These centered scatterings suggest that in both PVA/LDH and PVA/LDH-TCNF, LDH layers were primarily orientated around the (003) lattice plane parallel to the film direction. Any scattering in ψ angle indicated LDH sheets aligned ψ angle away from (003) crystal plane. We quantified the orientation distribution of LDH by using data obtained through pole figure measurements, following the approach reported by Yu et al. [33]. We averaged the scatterings from all φ angles to get a single set of scattering intensities as a function of sample tilt. This data was then fitted with Gaussian distribution (Figure S5). The fitting provided the full-width half-maximum (FWHM) values of 21.7° and 19.5° for PVA/LDH and PVA/LDH-CNF, respectively. Using these FWHM values, the orientation degree of LDH was calculated (using equation 5.2) as %87.8 and %89 for PVA/LDH and PVA/LDH-TCNF, respectively. For the PVA/LDH-TCNF sample, during the drying step of the coating application, the presence of TCNF resulted in a PVA/LDH-CNF interconnected structure that helped to maintain LDHs in a slightly more aligned state thanks to the H-bond and electrostatic interactions.

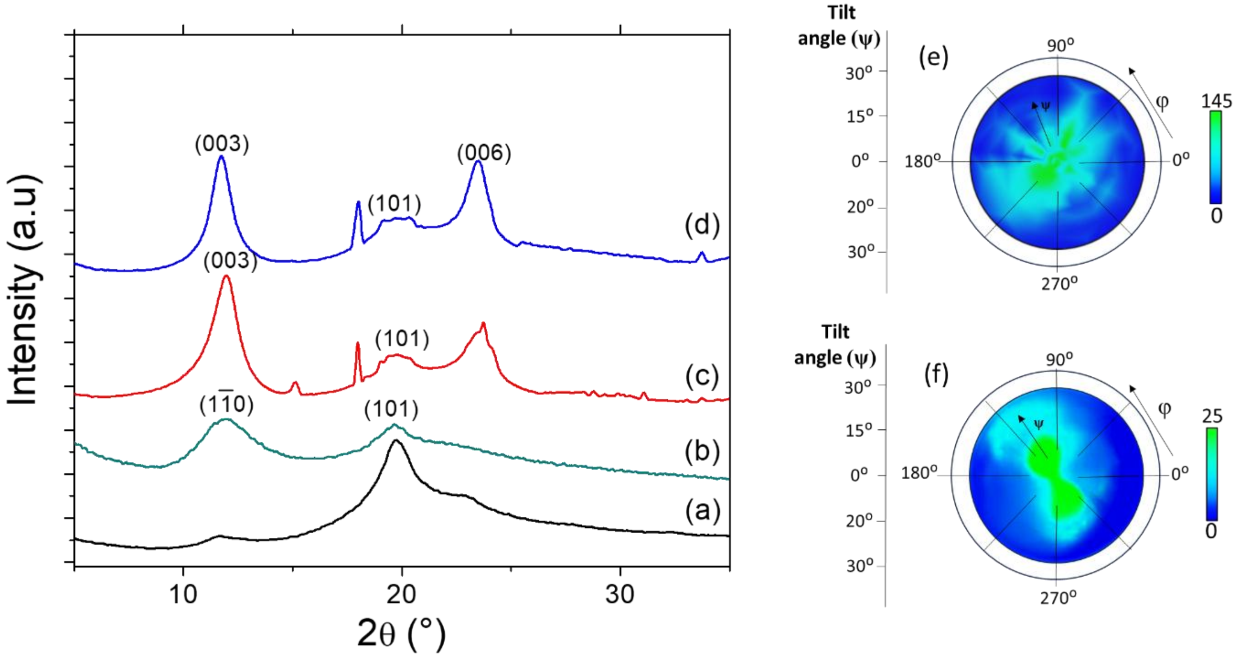

Figure 5.5 XRD graphs of (a) PVA, (b) PVA/TCNF, (c) PVA/LDH, (d) PVA/LDH-TCNF. Pole figure of (e) PVA/LDH and (f) PVA/LDH-CNF. Scattering intensity is higher at the center (0 tilt and rotation angle). This indicates that LDH layers are well-oriented around the (003) plane.

5.3.4 Surface characteristics of coating films

The overall surface morphology of coatings was examined using SEM. The PVA and PVA/TCNF coatings exhibited a smooth surface, likely due to their relatively similar flexible long-chain structures. In PVA/LDH and PVA/LDH-TCNF coatings, we observed a characteristic feature of nanoclay-added systems where nanoclay addition increases the surface roughness of coatings. For

PVA/LDH-TCNF coatings, the roughness of the surface slightly increased compared to PVA/LDH.

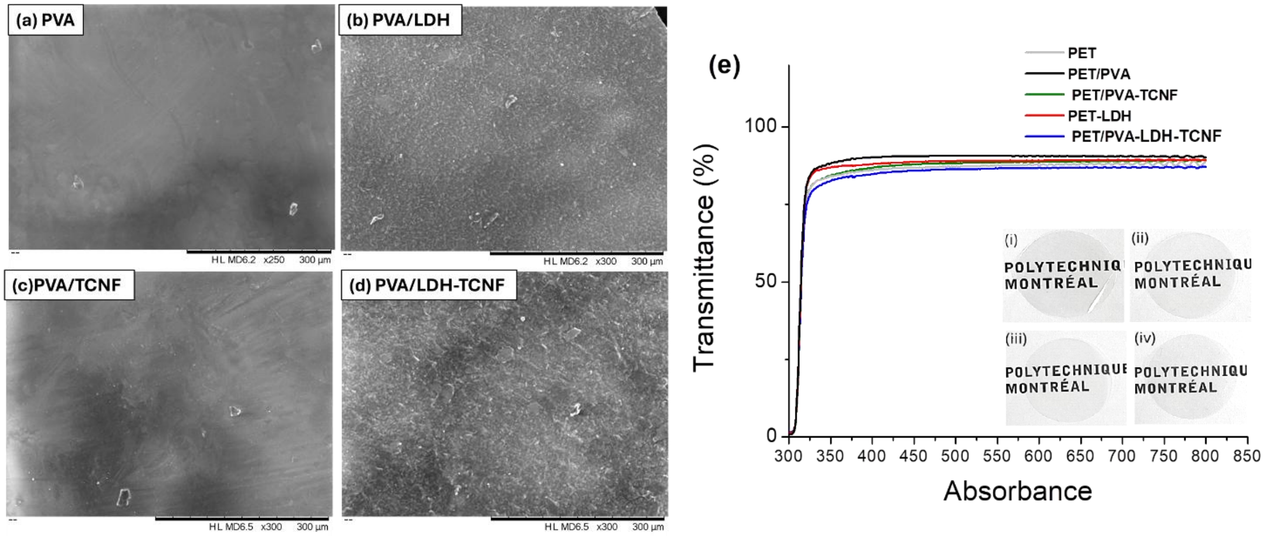

Figure 5.6 SEM micrographs of PET coated (a) PVA, (b) PVA/LDH, (c) PVA/TCNF, and (d) PVA/LDH-TCNF. Scale bar is 300 µm. (e) UV-vis spectra of PVA (colored black), PVA/TCNF (colored green), PVA/LDH (colored red), PVA/LDH-TCNF (colored blue) coatings on PET films. Insets are photographs of (i) PVA, (ii) PVA/LDH, (iii) PVA/TCNF, and (iv) PVA/LDH-TCNF coatings on PET film. All coated films showed high transparency.

The cross-section of PVA/LDH and PVA/LDH-TCNF coatings under SEM revealed a tightly packed structure (Figure S6.3). The shear thinning behavior of PVA/LDH-TCNF (Fig. 5.2c–e) enabled a uniform formation of the barrier layer on PET by rod coating. Moreover, electrostatic interactions LDH-TCNF within PVA led to the formation of a tightly bonded layer [44, 193]. No debonding was observed between substrate and coating layers, indicating good adhesion of coatings on corona-treated PET. The thickness of coatings layers ranged from approximately 1.5 to 2µm, as listed in Table S6.2.

The change in transparency of a substrate upon coating application is one indicator of coating uniformity and coating microstructure, including the dispersion and orientation of nanoparticles [41, 194, 195]. Digital images show (Figure 5.4e) no significant changes in the transparency of PET by applying coatings, which might indicate good dispersion of nanoparticles within PVA [23]. The UV-vis transmittance of the coated films was recorded to quantify the optical clarity of the coated films (Figure 5.4e). All coated films exhibited high UV-vis transmittance, with values exceeding %86.5 at 550 nm. The UV-vis transmittance of PET (%87.7 at 550 nm) is almost unaffected by applying PVA and PVA nanocomposite coatings.

5.3.5 Gas barrier performance of coatings

Figure 5.7 shows the oxygen permeability of PET and PVA, PVA/LDH, PVA/TCNF, and PVA/LDH-TCNF coatings on PET at 23°C %0 and %60 RH. To evaluate the coating layer's performance independently from the thickness of each coating, the oxygen permeability (OP) was calculated for each sample.

PET substrate has an OTR of 133 $cc·cm^{-2}·d^{-1}$ corresponding to an O_2 permeability of 1664 $cc·µm·cm^{-2}·d^{-1}·atm^{-1}$. Application of the PVA coating on PET reduced the OTR and OP values of PET from 133 $cc·cm^{-2}·d^{-1}$ and 1664 $cc·µm·cm^{-2}·d^{-1}·atm^{-1}$ to 9.9 $cc·µm·cm^{-2}·d^{-1}·atm^{-1}$. Upon incorporating wt%1 TCNF into PVA, OP further reduced to 6.5 $cc·µm·cm^{-2}·d^{-1}·atm^{-1}$. This limited improvement in OP could be attributed to nanopores or voids within the fibrillar structure of TCNF (Figure S5.6). On the other hand, LDH with a dense-compact structure is more impermeable to gases, offering superior oxygen barrier performance when combined with PVA (Figure S6). We achieved an OP of 1.8 $cc·µm·cm^{-2}·d^{-1}·atm^{-1}$, representing a %90 reduction in OP for PVA/LDH coatings compared to PET. As suggested by classical permeability models, nanoparticles can improve the gas barrier performance of polymers by creating a tortuous pathway that delays the permeation of gas molecules through the polymer film, as illustrated in Figure S5.6 [196]. This tortuosity can be maximized by combining oppositely charged LDH and TCNF; therefore, OP can be improved further. The PVA/LDH-TCNF coatings demonstrated exceptional oxygen barrier performance, with an OP of 0.6 $cc·µm·cm^{-2}·d^{-1}·atm^{-1}$, representing nearly a 99.9% reduction compared to the PET film. While nanoparticle tortuosity plays a significant role in this improvement, it is not the only mechanism explaining the enhanced gas barrier properties in complex hybrid systems [197]. Other factors, such as modification of polymer microstructure (e.g., crystallinity amount and morphology, network structure, or orientation of chains) and alterations to the polymer-nanoparticle interphase, are also crucial in enhancing permeability in polymer-hybrid nanoparticle systems [153, 196, 198, 199]. As discussed in the microstructure and interactions section, the coexistence of LDH and TCNF in PVA can create a more effective confined space and reinforce the network structure, potentially resulting in a synergistic effect on oxygen barrier performance [200].

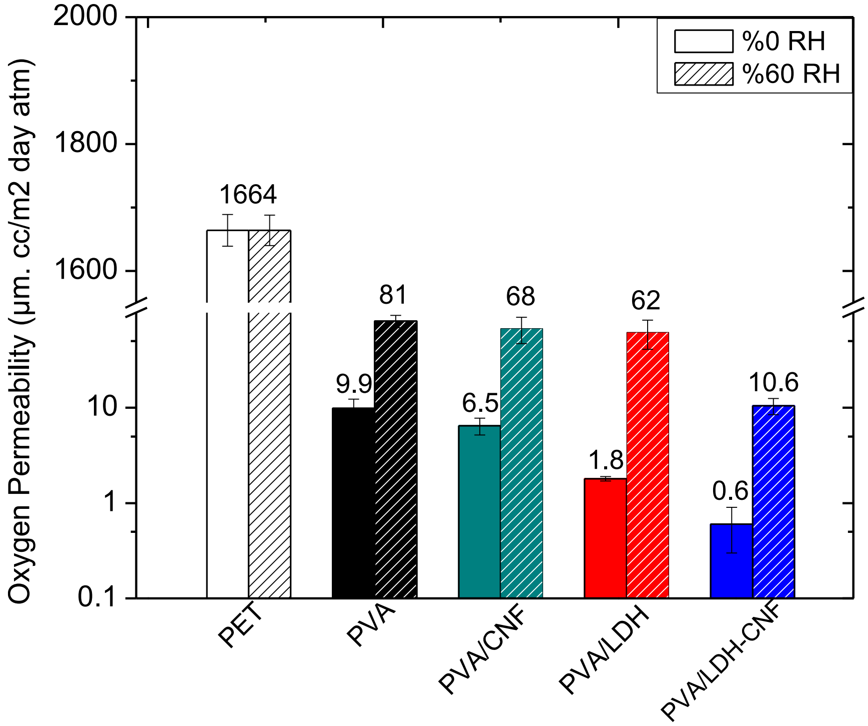

Figure 5.7 Oxygen permeability results of PVA, PVA/LDH, PVA/TCNF, and PVA/LDH-TCNF coatings on PET at %0 and %60 RH.

Considering the final application, we also conducted oxygen gas permeability tests under %60 RH (Figure 5.7). While PVA and TCNF typically provide excellent oxygen barrier properties, this is mostly under dry conditions. In high-humidity environments, water molecules can penetrate the PVA chains and/or TCNF fibrillar network, weakening the interactions, increasing the free volume within the structure, and facilitating the diffusion of oxygen molecules[15]. Consequently, OP of PVA increased to 81 $cc{\cdot}\mu m{\cdot}cm^{-2}{\cdot}d^{-1}{\cdot}atm^{-1}$ at %60 RH. Similarly, PVA/TCNF and PVA/LDH OP increased to 68 and 62 $cc{\cdot}\mu m{\cdot}cm^{-2}{\cdot}d^{-1}{\cdot}atm^{-1}$. On the other hand, the presence of oppositely charged LDH-CNF within PVA limited this loss in OP at %60 RH, and OP was measured as 10.6 $cc{\cdot}\mu m{\cdot}cm^{-2}{\cdot}d^{-1}{\cdot}atm^{-1}$. Mianehrow and coworkers [180] reported that graphene oxide could reduce the detrimental effect of humidity on barrier properties by stabilizing the CNF network. Similarly, Noshrinai et al. [201] showed that a three-dimensional network generated among PVA-cellulose nanocrystals and starch reduced the water solubility of final films. In our study, the interlocked-stabilized structure of PVA/LDH-CNF may also act in a similar manner, limiting the detrimental effect of humidity at %60 RH.

We used a Gelbo flex tester to simulate the mechanical stresses (twist, pull, and compress) that can occur in real applications. After 100 flex cycles, the oxygen permeability of coatings was measured, and the results are shown in Figure S5. PVA coating on PET exhibited a significant reduction in barrier performance, with an OP value of 451 cc·μm·cm^{-2}·d^{-1}·atm^{-1}. In contrast, PVA/LDH and PVA/TCNF maintained low OP values of 24.5 and 25 cc·μm·cm^{-2}·d^{-1}·atm^{-1}, respectively. We observed the lowest OP value of 18.8 cc·μm·cm^{-2}·d^{-1}·atm^{-1} in PVA/LDH-TCNF coating, indicating good mechanical flexibility of PVA-LDH-TCNF coatings under flex testing. Our PVA/LDH-TCNF coating exhibited much lower OP than metalized PET film sandwiched between oriented-PET and linear low-density polyethylene, which had an OP of 226 cc·μm·cm^{-2}·d^{-1}·atm^{-1} after 27 flex cycles [202].

Considering all these findings from our study as well as from the literature [197], we concluded that the following factors may govern the improved oxygen gas barrier performance of PVA-LDH-TCNF coatings:

I. Maximized tortuous pathway of oxygen molecules through interconnected structure and densification of this structure through H-bond and electrostatic interactions (i.e., modification of microstructure) [46, 200, 203-205]

II. Enhanced resistance to humidity and mechanical stress thanks to the high cohesive energy of stiff interlocked network (i.e., modification of segmental mobility and dynamic free volume) [153, 206, 207]

III. The influence of nanoparticles on each other's orientation, dispersion, bending, and defects. (i.e., modification of nanoparticle states) [92, 168, 208]

To confirm the barrier improvement mechanisms of (I) and (II), we fit experimental OTR data of the PVA/LDH-CNF sample to various gas permeability models. Table 5.1 presents the permeability models, equations, assumptions/parameters, and the final relative permeability values obtained using those models. We calculated the effective aspect ratio of LDH-TCNF to fit a single aspect ratio into models; detailed explanations are provided in the supporting document.

In the PVA/LDH-CNF sample, the experimental value of P/P_0 is 0.06. We observed that the Nielsen, Cussler-Moggridge, Gusev-Lusti, and Fredrickson-Bicerano models predicted higher P/P_0 values than our experimental P/P_0 value. Among these models, Cussler's model estimated a higher reduction in permeability due to the more restrictions and resistances accounted for in this model.

However, when we apply the extension of the Cussler model (i.e., Cussler-Moggridge) for hexagonal nanoparticle geometry -which corresponds to the shape of LDHs- we obtained a P/P_0 value of 0.0701, which is still higher than our experimental P/P_0.

As shown in Table 5.1, these models rely on nanoparticle volume, orientation, and aspect ratio. However, they do not account for microstructural changes such as alterations in matrix morphology (in both crystalline and amorphous regions) and/or the interphase [16, 196, 209-212]. Strong interfacial interactions between nanoparticles and polymer matrix likely reduce the segmental mobility, suppress the interfacial cavities, and densify the structure, limiting available free volume for gas diffusion [196, 207, 212]. In our case, an interlocked PVA–TNCF–LDH network may further densify the structure and restrict chain flexibility. Thus, since our experimental P/P_0 value is lower than the predicted P/P_0 values of these tortuosity models, we can conclude that the permeability reduction in PVA/LDH-TCNF coatings is not the sole effect of LDH-TNCF tortuosity, but rather the combined effect of factors (I), (II), and (III).

Table 5.1 Permeability models, corresponding assumptions, predicted and experimental values of P/P_0 for PVA/LDH-TCNF coating.

Model		**Filler geometry**	**Flake size, array type**	**Equation**	**Predicted P/P_0**	**Experimental P/P_0**
Nielsen[213]	2D	Ribbon	Monodisperse, Regular array	$/\frac{P}{P_0} = \frac{1-\emptyset}{1+\frac{\alpha}{2}\emptyset}$	0. 110	0.0606
Cussler [214]	2D	Ribbon	Monodisperse, Random array	$\frac{P}{P_0} = \frac{1-\emptyset}{(1+\frac{\alpha}{3}\emptyset)^2}$	0.0291	
Cussler-Moggridge[214]	2D	Hexagonal	Polydisperse, Random array	$\frac{P}{P_0} = (1+\frac{2}{27}\frac{\alpha^2\emptyset^2}{1-\emptyset})^{-1}$	0.0701	
Gusev-Lusti[215]	3D	Disc	Polydisperse, Random Array	$\frac{P}{P_0} = \frac{1-\emptyset}{e^{(\frac{\alpha}{3.47}\emptyset)^{0.71}}}$	0.0643	
Fredrickson-Bicerano[216]	3D	Disc	Monodisperse, Random array	$\frac{P}{P_0} = \frac{(1-\emptyset)(2+x)^2}{4(1+x+0.1245x^2)^2}$ where $x = \frac{\pi\times\emptyset\times\alpha}{2\ln(\frac{\alpha}{2})}$	0.112	

$\emptyset$ is volume fraction, α is the aspect ratio.

Considering point (III), various studies have shown that in systems containing two different nanoparticles, the defects, bending, and re-agglomeration (re-stacking) of one nanoparticle can be minimized by the secondary nanoparticle, leading to further improvement in gas barrier properties [92, 208].

With a permeability coefficient of 10.6 cc·µm·cm^{-2}·d^{-1}·atm^{-1} at %60 RH, PVA/LDH-TCNF barrier performance is comparable to widely used barrier polymers such as polyvinylidene chloride (PVdC) and ethylene-vinyl alcohol (EVOH). At 23° and %50 RH, PVdC has OP of ~90 cc·µm·cm^{-2}·d^{-1}·atm^{-1} and EVOH has OP of ~14 cc·µm·cm^{-2}·d^{-1}·atm^{-1} with similar coating thicknesses [217].

WVTR was measured as 11 g·cm^{-2}·d^{-1}·and 10.5 g·cm^{-2}·d^{-1} for PVA and PVA/TCNF, respectively. PVA/LDH coating demonstrated a WVTR of 7.8 g·cm^{-2}·d^{-1}, while PVA/LDH-TCNF coating reduced WVTR by approximately 18%, reaching 9.4 g·cm^{-2}·d^{-1}. The water vapor barrier properties of both PVA/LDH and PVA/LDH-TCNF coatings can be satisfactory in various high-barrier applications for food packaging, such as nuts and snacks[218].

5.4 Conclusion

In this study, benefiting from the oppositely charged natures of LDH and TCNF, we developed PVA/LDH-TCNF coatings with a rigid network structure with high cohesive energy and lower free volume. Positively charged LDH acted as a bridge, interlocking the TCNF network within PVA through hydrogen bonding and electrostatic interactions. Stable, homogeneous coating dispersions with shear thinning behavior enabled the formation of uniform coatings on PET substrate. The presence of negatively charged TCNF slightly improved the LDH orientation during the drying stage, reaching a degree of %89. Coatings showed a good adhesion to corona-treated PET substrate. All of those provided the basis for improving oxygen barrier performance at different conditions, i.e., higher humidity and under-flexed. A synergistic effect of using oppositely charged LDH-TCNF improved the oxygen performance of coatings more than their induvial counterparts; final OP was measured as 0.6 cc·µm·cm^{-2}·d^{-1}·atm^{-1}, representing a %99.9 reduction compared to PET. We showed that this improvement does not only originate from the simple tortuous effect of nanoparticles but is a combination of tortuous effects, rigid and dense network formation, and modification of nanoparticle states. This study provides fundamental knowledge for designing barrier dispersions containing multicomponent and oppositely charged nanoparticles. This PVA/LDH-TCNF hybrid barrier dispersion shows comparable OP to PVdC, and EVOH can be recyclable and does not contain any volatile organic compound; therefore, they can be used for food packaging applications as a safe and sustainable solution.

5.5 Acknowledgments

The authors gratefully acknowledge the financial support of 3SPack NSERC Industrial Research Chair by the Natural Science and Engineering Council of Canada (NSERC) and ProAmpac Inc. Compa.

5.6 Supporting Information

Cross section of coated films, calculation of the effective aspect ratio, coating weight, thickness and OTR results are reported in Appendix B.

CHAPTER 6 ARTICLE 3 : REPULPABLE AND GAS BARRIER POLYVINYL ALCOHOL-CELLULOSE NANOFIBER-LAYERED DOUBLE HYDROXIDE COATINGS

Emre Vatansever[1] Amir Saffar[1,2], Abdellah Ajji[1*]

1: 3SPack, Research Center for High Performance Polymer and Composite Systems (CREPEC), Chemical Engineering Department, Polytechnique Montréal, Montréal, Québec H3C 3A7, Canada

2 ProAmpac Terrebonne, QC, Canada J6Y 1V2

**Corresponding Author, email: abdellah.ajji@polymtl.ca*

Submitted to Carbohydrate Polymers on November 3, 2024

Abstract

In this study, repulpable paper coatings with enhanced oxygen and water vapor barrier properties were developed. The water-based coatings were formulated using polyvinyl alcohol (PVA), positively charged layered double hydroxide (LDH), and negatively charged TEMPO-oxidized cellulose nanofiber (TCNF). These coatings were applied to paper at a low coating weight of 5.2 g/m² using an automatic bar coater integrated with an infrared dryer for fast drying. Incorporating LDH-TCNF hybrids into the PVA matrix led to a thickening effect attributed to the formation of an electrostatically complex network, as indicated by an increase in low shear viscosity. The synergy between LDH and TCNF in PVA enhanced blistering resistance and reduced coating penetration into the paper, forming the basis for improved gas barrier properties. The oxygen transmission rate (OTR) of the PVA-LDH-TCNF coating was 10.1 and 31 cc/m²day at 0% and 50% relative humidity (RH), respectively. After thermal treatment at 130 °C for 90 minutes, the OTR was reduced to 9.5 cc/m²·day at 50% RH, attributed to increased electrostatic interactions, hydrophobicity, and reduction of free volume. A similar trend was observed in the water vapor transmission rate, with the lowest value of 10.4 g/m²day for the thermally treated PVA-LDH-TCNF coating. Repulpability rates were 82% for PVA, and 83% for PVA-LDH-TCNF, and no residual PVA or LDH-TCNF was detected in the recovered pulp. Overall, the PVA-LDH-TCNF coating demonstrates excellent oxygen and water vapor barrier performance with minimal coating usage, presenting a practical and recyclable option for packaging applications.

Keywords: Barrier coating, polyvinyl alcohol, layered double hydroxide, cellulose nanofiber, recyclable, repulpable

6.1 Introduction

The global focus on reducing plastic usage has led to a rise in the use of biodegradable, renewable, and recyclable paper as an alternative packaging material. This trend, known as "paperization," is becoming prominent in the packaging industry. While paper offers environmental benefits, its barrier performance is often inadequate for many applications. Traditional methods, such as lamination with plastics or aluminum foils, metallization, fluorochemicals, and waxes, have addressed these issues. However, these approaches complicate the recyclability of paper and come with drawbacks such as poor heat sealibility and low crack resistance [219-222].

In response to these challenges, research has increasingly focused on developing water-based barrier coatings (WBBC) as alternatives to conventional methods. WBBCs are easily removable from paper, perform well at lower coat weights than other systems, and can be applied in-line or off-line [223, 224]. However, achieving an optimal balanced oxygen and water vapor barrier performance without using high coating weights is challenging [1, 225].

The use of polyvinyl alcohol (PVA) in WBBC barrier dispersions offers excellent oxygen gas properties, film-forming ability, biodegradability, heat sealability, and non-toxicity. However, PVA's oxygen gas performance is limited at higher relative humidities and is sensitive to mechanical stress [226]. Our previous study [227] indicated that combining oppositely charged layered double hydroxide (LDH) and 2,2,6,6-tetramethylpiperidine-1-oxyl-oxidized cellulose nanofiber (TCNF) can enhance the oxygen barrier performance of PVA under higher relative humidity and after flexing. LDH, with its unique layered structure and high aspect ratio, provides excellent barrier properties and can be used as a pigment (or filler) for high-barrier coating applications. Nanocelluloses can also improve the gas barrier performance of paper and bring additional functionality, such as improving water retention and rheological properties [228-231], acting as dispersants or stabilizers [232-234], and enhancing flexibility [163, 235-237]. High water retention and shear thinning behavior can reduce coating penetration inside paper, ensuring smooth drying and high coating quality.

The gas barrier performance of coatings can be further improved by applying a thermal treatment. For example, Kim et al. [44] found that hot pressing of cellulose nanowhisker and chitin improved their synergy and decreased the OTR due to the forming amide bonds between components. Similarly, thermal treatment of CNF at 175 ˚C for 3 hours reduced the OP and WVP by 25 and two-fold, respectively [47]. These improvements in OP and WVP were attributed to reduced interfibrillar space or porosity, increased crystallinity, and increased hydrophobicity due to hornification [47].

Herein, we have developed waterborne PVA-LDH-TCNF barrier coatings for paper products. We applied low coating weights using a bar coating approach integrated with an IR dryer to ensure lower penetration and high repulpability of the coated paper. We examined the effect of nanocellulose and nanoclay on PVA film formation and characterized the surface blistering and penetration of the coatings using darkfield fluorescence microscopy. The surface characteristics and possible surface defects were also investigated using scanning electron microscopy. Thermal treatment was applied to further improve the gas barrier performance of coatings at higher relative humidities. The repulpability of the coated papers was evaluated by separating the paper pulp from the coating via a repulping approach. Our proposed approach is a straightforward one-step that can be easily implemented for recyclable high-barrier coatings.

6.2 Materials and Methods

6.2.1 Materials and substrates

PVA (Mw=140 000 – 186 000 g/mol) was purchased from Sigma Aldrich. The positively charged LDH, provided by Kisuma Chemicals, was further modified to obtain a high aspect ratio LDH. Cellulose nanofiber is surface modified via 2,2,6,6-tetramethyl-1-piperidinyloxy (TEMPO)-mediated oxidation, purchased from the University of Maine (ME, USA) and used without further purification. Acridine orange (Sigma Aldrich, St. Louis, MO, USA) was used as a fluorescent dye to stain the coating dispersions. The paper used in this study was supplied by ProAmpac and is a natural, unbleached kraft paper with a base weight of 75 g/m². It was pre-coated with low-density polyethylene (LDPE) at a coating weight of approximately 7 g/m². In this study, this substrate is referred to as the base paper (BP).

6.2.2 Calcination and Hydrothermal Synthesis of LDH

High aspect ratio LDHs were synthesized using the calcination-rehydration method. First, LDH was calcined at 500 °C for 12 hours at a heating rate of 5 °C per minute. To prepare a high aspect ratio LDH, 2 g of the calcined LDH was mixed with 20 ml of an aqueous glycine solution at a 1:1.5 (LDH: glycine) ratio. The mixture's pH was adjusted to approximately 6, and the solution was placed in a Teflon-lined autoclave and heated at 100 °C for 72 hours for rehydration. After rehydration, the LDH was washed with deionized water to remove impurities.

6.2.3 Preparation of coating dispersions and application on paper

PVA was first dissolved in deionized (DI) water at 90 °C for 2 hours using a magnetic stirrer. When PVA was used alone, the total solid content was 5 wt% relative to the aqueous phase. Prepared high aspect ratio LDHs were diluted to 2 wt% and dispersed in DI water for 180 seconds using an ultrasonic probe (Cole-Parmer) at 30 W. To prepare TCNF; the required amount was first dispersed in DI water at 80 °C for 1 hour using a magnetic stirrer. Then, TCNF was further dispersed using ultrasonication under the same conditions as LDH. To prepare PVA-LDH-TCNF (coded as PVA-LC), LDH-TCNF hybrid (2 wt% total) was briefly mixed via ultrasonication and then added to the PVA solution, which was stirred for 2 hours. The final concentrations of PVA and LDH-TCNF in water were adjusted to 4 wt% and 1 wt%, respectively. Coating dispersions were applied to 80 µm thick, freshly corona-treated base paper (BP). The application process was performed using an automatic coater (TQC Sheen AB4120) equipped with a Mayer rod, providing a 30 µm wet film thickness and moving at a controlled speed of 100 mm/s. All samples were double-coated under identical conditions and rapidly dried using an infrared (IR) dryer (Datou Boss, ZJ-SC-002, 2 kW, 220V). Thermal treatment was applied at 130 °C for 90 minutes in an oven. The sample notations, compositions, and conditions are summarized in Table 6.1.

Table 6.1 Sample notations, compositions, and thermal treatment conditions

`Sample	**Polymer**	**Filler**	**Thermal treatment**	**Coating weight (g/m^2)**	**Total thickness (µm)**
BP	-	-	-	-	83.3 ± 1.7
BP_PVA	PVA wt% 5	-	-	6.4 ± 0.6	87.1 ± 2.1
BP_PVA-LC	PVA wt% 4	%0.5 LDH and %0.5 TCNF	-	5.2 ± 1.2	87.2 ± 4.2
BP_ PVA_TT	PVA wt% 5	-	130°C, 90 min	6.4 ± 0.6	87.1 ± 2.1
BP_ PVA-LC_TT	PVA wt% 4	%0.5 LDH and %0.5 TCNF	130°C, 90 min	5.2 ± 1.2	87.2 ± 4.2

6.2.4 Coating weight and thickness

Coating weights were determined by subtracting the weight of the uncoated paper from the weight of the coated paper. Sample thicknesses were measured using an automatic deadweight micrometer (ProGage Touch Thickness Tester, Thwing-Albert Instrument, USA) with a sensitivity of 0.01 mm, and the values were reported as the average of at least three measurements.

6.2.5 Attenuated total reflection-Fourier transform infrared (ATR-FTIR)

ATR-FTIR analysis was conducted using a 65 FTIR Spectrometer (PerkinElmer, Woodbridge, ON, Canada) in attenuated total reflection (ATR) mode. Spectra were acquired in the 600 – 4000 cm^{-1} range, comprising 36 scans with a resolution of 4 cm^{-1}. For crystallinity measurements, we used the following equation:

$$x_c(\%) = a + b\,(\frac{I_c}{I_a}) \tag{6.1}$$

where a and b are correlation coefficients. For PVA, the values of these coefficients are assigned as −13.1 and 89.5, respectively[167]. I_c and I_a are the IR absorbance intensities of peaks corresponding to the crystalline phase at a wavenumber range of 1140–1145 cm^{-1} and the amorphous phase at a wavenumber around 1090–1096 cm^{-1}, respectively[167].

6.2.6 Rheological measurements

The rheological behaviors of coating dispersions were analyzed using a rotational rheometer (Anton Paar, MCR501, Germany). Rheological tests were conducted with a concentric cylinder. Shear sweep tests were performed, ranging from 100 to 0.1 s^{-1}. Before each test, coating mixtures were pre-sheared to eliminate air from the sample and ensure a consistent starting microstructure. All tests were carried out at 25°C.

6.2.7 Transmission Electron Microscopy (TEM)

Electron microscopic images were obtained using a JEOL JSM-6400F (Japan) field emission scanning electron microscopy operating at 200 kV. For LDH sample preparation, a droplet of LDH-containing dispersion was placed on a TEM grid, allowed to dry, and then coated with platinum before imaging. For the TCNF samples, the TEM grids were initially positively charged using the Pelco Glow Discharge Cleaning System. A 0.1 wt% TCNF solution in water was then drop-cast onto the grids, followed by negative staining with uranyl acetate.

6.2.8 Zeta Potential and Dynamic Light Scattering (DLS) Measurements

The zeta potential of LDH and TCNF particles was determined using a Nano ZS Zetasizer at 25°C. The concentration of nanoparticles in water was approximately 0.05 wt.%. Five runs were conducted for each sample, and the data were analyzed using the Smoluchowski model. An average of three measurements was obtained for each sample, and the mean value was reported.

6.2.9 Scanning Electron Microscopy (SEM)

The surface characteristics of coatings were observed with a field-emission SEM (FE-SEM) machine (JSM 7600F, JEOL) operated at 5kV accelerating voltage. Samples were mounted with carbon tape on stubs for imagining.

6.2.10 Analysis of coating penetration into paper

1 mL of 0.05% acridine orange solution was added to 30 mL of 5% coating solutions at 80 °C and in darkness for 2 h and then coated on the surfaces of the base papers in darkness to hinder any photodegradation. The paper samples were cut in the machine direction with a surgical blade fastened to the side of a smooth-based metal block. The surface of the cross-section was thus as smooth and planar as possible to give a clear and focused image. The cross-section was analyzed using dark-field optical microscopy with an Olympus BX51 microscope (Cytoviva). A 10x UPL fluorite oil objective was used in conjunction with a Retigna 2000R fast 1394 Q imaging camera, a cooled color 12-bit, for capturing high-resolution images. Fluorescence imaging was performed using a FITC fluorescent light source to excite the fluorescent signals within the samples. Dark-field microscopy allowed for enhanced contrast in the sample images by scattering light around the specimen, highlighting the structural details of the coating layers. The fluorescent light source enabled the visualization of fluorescent components within the coatings.

6.2.11 Gas permeability measurements

Oxygen permeability was measured using the MOCON OXTRAN 2/21 apparatus (Minneapolis, USA) under controlled conditions of 0% relative humidity, 23°C, and 1 atm, following ASTM D-3985-81 and ASTM F1927 guidelines for sample preparation (5 cm^2). Both sides of the specimen were maintained at 0% RH and 23 °C. Additional tests were performed at 50% RH and 90% RH to evaluate the effect of humidity on the coatings. Each measurement was conducted in triplicate. The MOCON OXTRAN 2/12 was used to measure the OTR of the base paper, as it accommodates higher limits. The water vapor transmission rate (WVTR) of the samples was determined at 23 °C and 50% RH using a MOCON PERMATRAN-W Model 101K, following ASTM F1249.

6.2.12 Mechanical Test

The tensile properties of the papers were examined using a universal testing machine (Instron 5943, Instron Corp., Norwood, MA, USA) equipped with a 500-N load cell. Samples were cut in the machine direction with 25.4 mm in width and 100 mm in length, and the tensile testing was carried out at 23 °C and 50% RH. Tests were done in 8 duplications. Average values of the elongation at break and tensile strength were calculated and reported. Tensile index (N·m/g) refers to the average tensile strength of the sample (N/m) divided by the grammage of the sample (g/m^2).

6.2.13 Repulpability Test

The repulpability of coated and uncoated papers was tested based on the “Voluntary Standard For Repulping and Recycling Corrugated Fiberboard Treated” developed by Fibre Box Association and the American Forest & Paper Association with minor modifications. Briefly, coated-paper samples were cut into dimensions of 10×10 cm^2 pieces and subsequently soaked in warm water (~50 °C at pH 7) for 10 min. The resulting pulp was passed through a 0.010-inch screen to separate the fibers (of pulp) from any residual coating. Fiber recovery was calculated as the percentage of fibers that passed through the screen relative to the initial fiber charge. The recovered fibers were dried in a laboratory oven at 100°C for 4 hours to remove moisture. As a control, uncoated paper samples were subjected to the same pulping and screening conditions. Then, fiber yield was calculated using Equation 6.2.

$$Fiber\ Recovery\ (\%) = \frac{Dry\ weight\ of\ accepted\ sample\ (g)}{Dry\ weight\ of\ sample\ (g)} \text{x}100 \qquad (6.2)$$

6.3 Results and Discussions

6.3.1 Wet properties of coating dispersions

The basic structural and charge properties of LDH and TCNF were initially characterized. The TEM micrograph in Figure 6.1a shows that LDHs exhibit hexagonal platelet structure with an average lateral size of 232 ± 71 nm and the average width and length of TNCF measured as 3.6 ±

0.8 nm and 252 ± 68 nm, respectively. Zeta potential LDH and TCNF were measured as +35 mV and -49 mV, respectively.

The rheological behavior of coating dispersions is a critical factor that determines the final performance and applicability of coatings. The interactions among all coating components significantly affect the rheological properties [238]. To investigate the rheological behavior of our coatings, we conducted steady shear measurements. Figure 6.2 shows apparent shear viscosity (η) versus shear rate (γ) results of PVA and PVA-LC coating dispersions with a total 5 wt% solid content. PVA exhibited liquid-like behavior at this solid content with slight increases at low shear rates. In contrast, PVA-LC dispersions exhibit a strong shear thinning behavior, characterized by a gradual increase in viscosity as the γ decreases. This increase in η at lower γ is attributed to the network formation between TCNF and LDH within PVA. Previous studies have shown that CNF can be used as a rheology modifier/thickening agent for paper coatings [231]. In our system, the oppositely charged natures of LDH and TCNF further reinforce this thickening effect, resulting in an infinite η in the PVA-LC sample. This rheological behavior is crucial for achieving a uniform coating on the surface of paper samples.

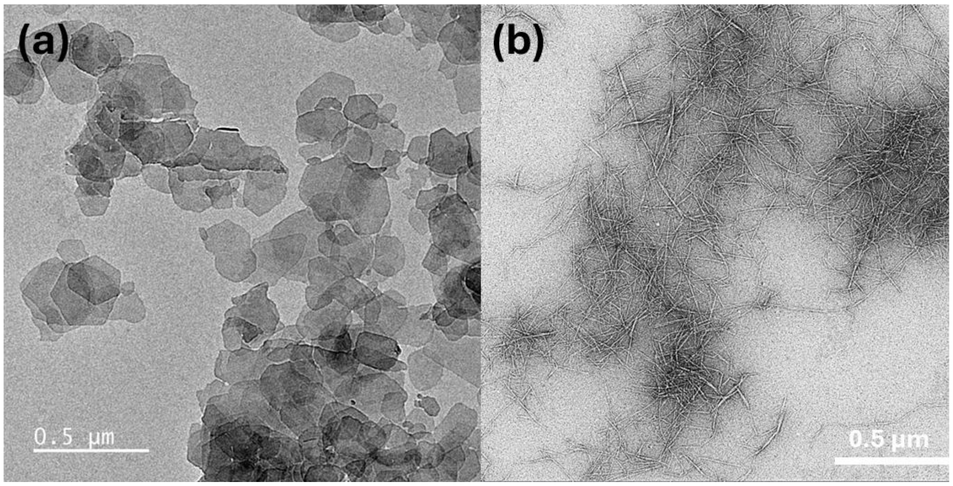

Figure 6.1 TEM image of (a) high aspect ratio LDHs prepared using calcination-rehydration method, scale bar 0.5µm. (b) TEMPO-oxidized CNF, scale bar 100 nm

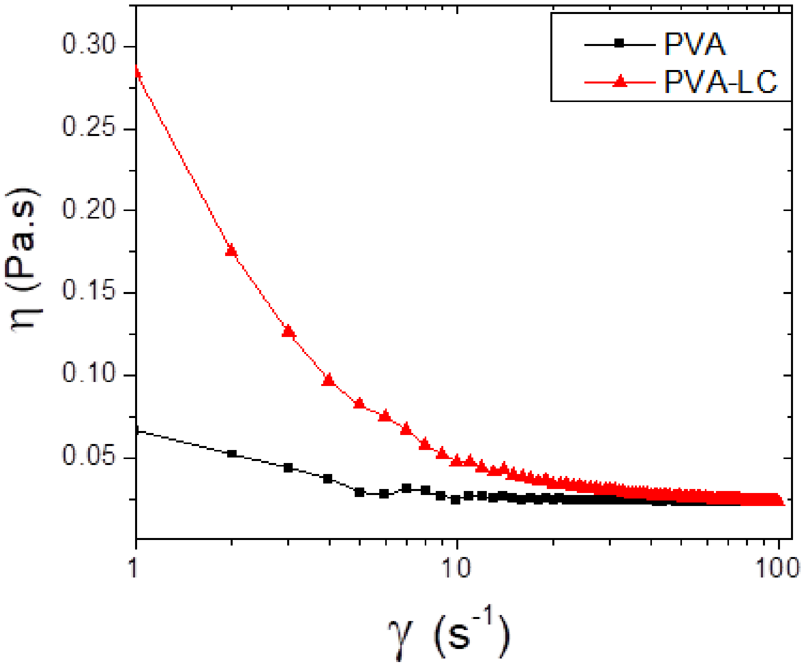

Figure 6.2 Viscosity (*η)* vs shear rate (*γ*) of PVA and PVA-LC dispersions. Shear viscosity increases at lower shear rates due to the interconnected network structure in PVA-LDH-TCNF.

6.3.2 Coating application and surface characteristics

The coating weight and thicknesses of the coated paper substrates are summarized in Table 6.1. The results show that coated papers have slightly different coating weights of 6.4 ± 0.6 g/m^2 for PVA and 5.2 ± 1.2 g/m^2 for PVA-LC. However, both coated papers have a similar total thickness of ~87.1 µm and a coating thickness of ~4 µm. This difference in coating weight and thickness is likely due to the variations in viscosity and structure of PVA and PVA-LC, which can affect the deposition behavior of the coating dispersion on paper. A more detailed discussion is provided in Section 6.3.3.

In paper coating, factors such as drying efficiency and the pH of the final solution are essential in meeting industry standards. Both PVA and PVA-LC dispersions have a final pH of approximately 9, which is acceptable to prevent damage to the paper fibers. Efficient drying is also crucial, as it can reduce the penetration of the coating into the paper and provide a uniform coating layer. We utilized fast IR drying to minimize the penetration of the coating into the paper. However, we observed blistering in some regions of the paper surface when PVA was used alone (Figure 6.3).

No blistering occurred in the PVA-LC coating. Guezennec et al. [94] indicated that adding microfibrillar cellulose (MFC) to PVA helped prevent blistering by reducing interactions between PVA and water, accelerating the drying process. In our study, TCNF, with a structure similar to MFC, led to more controlled and uniform drying in PVA-LC. To ensure consistency, we selected the areas of the samples where blistering did not occur for further characterization.

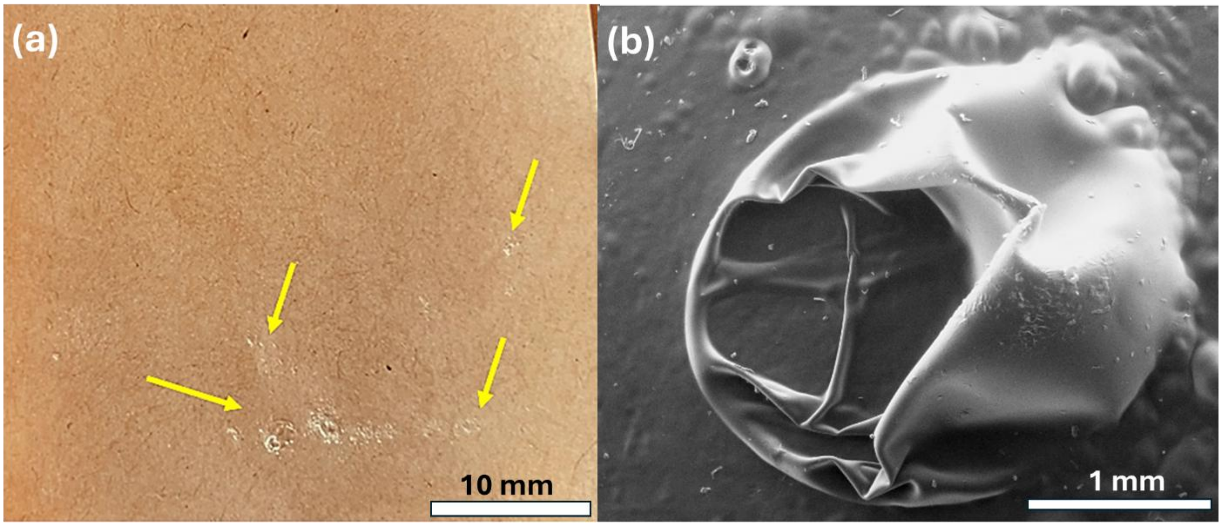

Figure 6.3 (a) Photographs of blistering after drying PVA coatings through IR dryer (b) SEM image of blistering.

The surface characteristics of coated papers were analyzed by using SEM. Figure 6.4 shows SEM images of BP, PVA-coated BP, and PVA-LC-coated BP. We observed that PE coating did not fully cover the paper surface, leaving some visible uncovered areas. The application of both PVA and PVA-LC covered these uncovered spots. The addition of LDH-TCNF in PVA slightly increased the surface roughness. Finally, we did not observe any pinholes in either PVA or PVA-LC-coated papers.

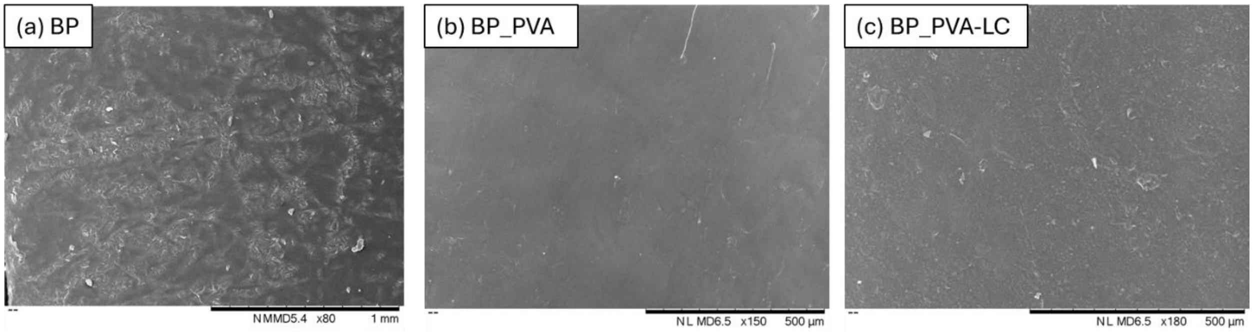

Figure 6.4 SEM images of (a) base paper (BP) and (b) PVA-coated BP (c) PVA-LC coated BP

6.3.3 Penetration study of coatings into paper

The extent to which coating dispersions penetrate into paper significantly affects the barrier performance of the coated paper. Excessive penetration may leave some parts of the paper surface uncovered. Furthermore, the absorption of large amounts of water into the paper can cause fiber swelling and debonding, leading to web breaks. In this context, we investigated the penetration of PVA and PVA-LC coatings inside paper. An AO fluorescent dye was used to stain coating dispersions to investigate the penetrations. Then, the cross-sections of the coated papers were analyzed under a darkfield fluorescence microscope, as shown in Figure 6.5.

The PVA-LC remained on the surface more than PVA. The main factors that hindered PVA-LC penetration are the thickening effect, stronger coating-paper interactions, and improved water retention (Figure 6.5). First, the electrostatically complex LDH-TCNF network within PVA induces a thickening effect, slowing down penetration into the paper [239]. In contrast, with its lower viscosity, pure PVA penetrated more deeply into paper [239, 240]. Secondly, LDH and TCNF can interact with cellulose fibrils in the paper during the coating application. TCNF and paper cellulose fibrils have similar chemical structures; therefore, they may have a higher affinity than PVA-paper cellulose fibrils [241]. LDH, with its positive charges, can also interact with the negatively charged cellulose fibrils in paper. The use of cationic additives to reduce the penetration of coating dispersion into paper has been well-documented [10, 242, 243]. Finally, thanks to the abundant hydroxyl and carboxyl groups in LDH and TCNF, along with the network structure, the PVA-LC dispersion retains more water [231, 244, 245]. This higher water retention can prevent overflow of coating inside porous paper [238, 246].

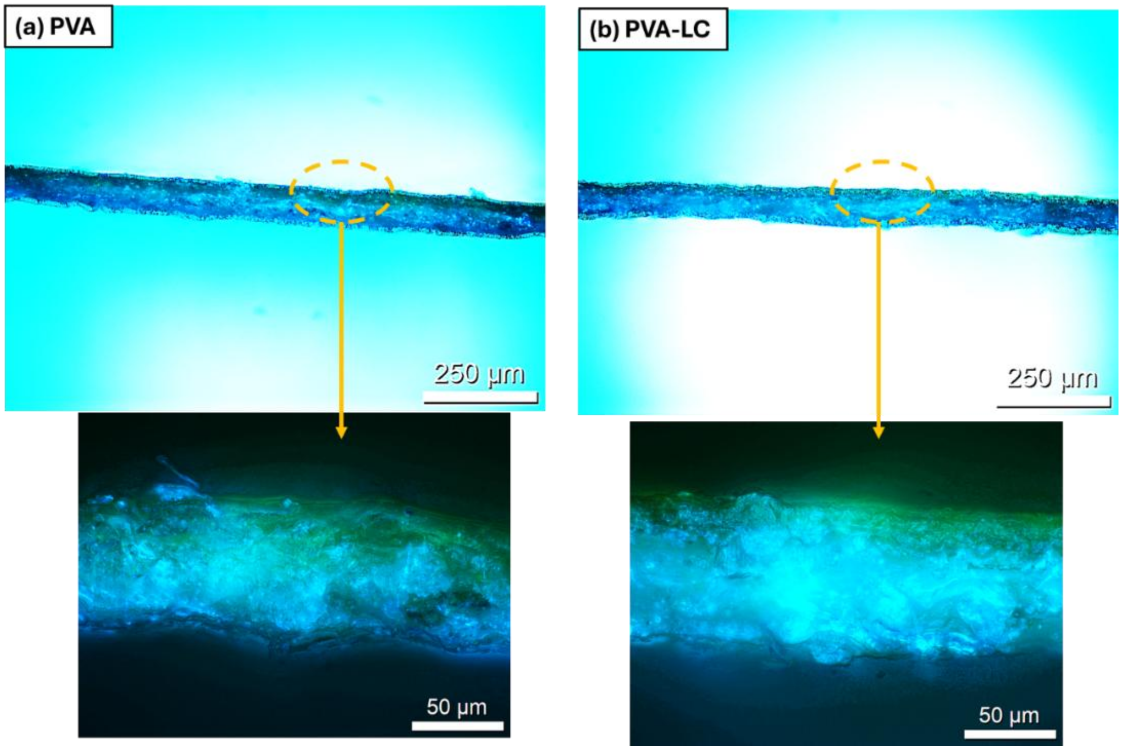

Figure 6.5 Penetration of (a) PVA and (b) PVA/LDH-CNF coatings into paper. The yellowish color shows stained coatings. LDH-CNF addition reduces the PVA penetration inside the paper.

6.3.4 Microstructure and interactions

FTIR tests were conducted to analyze the microstructure and interactions in coatings, and the results are shown in Figure 6.6. Some similar characteristics were observed in both PVA and PVA-LC, including those at 3267-3297 cm^{-1} (O–H stretching), 2916-2920 cm^{-1} (C–H stretching), 1334-1350 cm^{-1} (CH_2 wagging symmetric bending), 1144-1131 cm^{-1}, (C–O–C stretching) 1060 cm^{-1} and 1035 cm^{-1} (C–O stretching)[184, 185].

The FTIR spectra showed more distinct differences before and after thermal treatment. After the thermal treatment of PVA-LC, the N-H bending shifted from 1559 cm-1 to 1565 cm-1 with a slight increase in intensity, and O-H stretching shifted from 3270 to 3286 cm-1. These shifts suggest stronger hydrogen bonding and increased electrostatic interactions, likely contributing to a more densely packed structure [44]. In PVA-coated paper, the only change was a decrease in the intensity of O-H stretching, likely due to the removal of water during thermal treatment. No new peaks were detected in either coating, indicating that thermal treatment did not result in chemical crosslinking or amide bond formation.

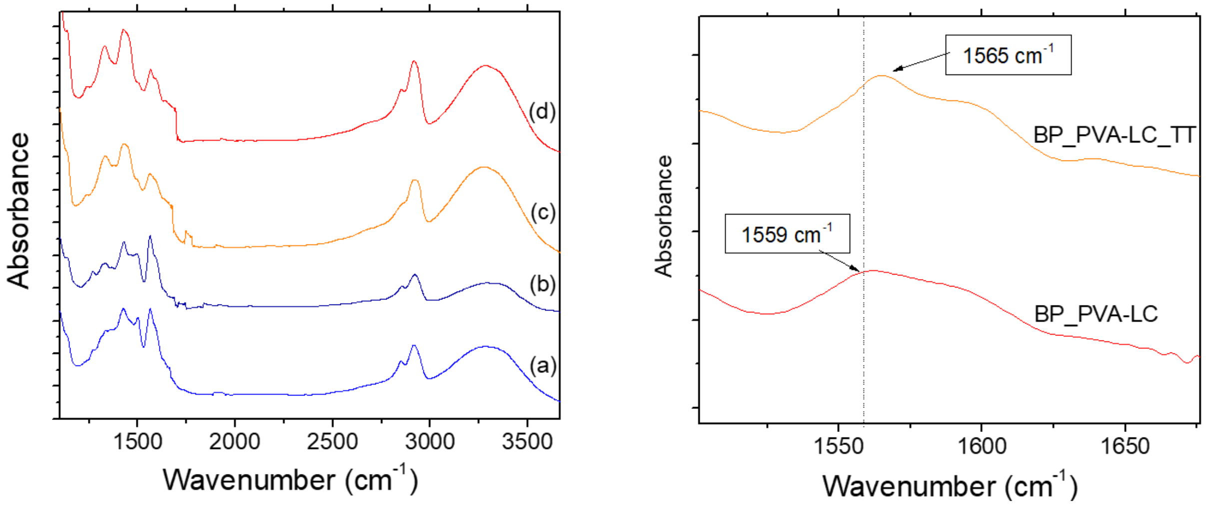

Figure 6.6 (Left) FTIR spectra of (a) BP_PVA, (b) BP_PVA_TT, (c) BP_PVA-LC, and (d) BP_PVA-LC_T (Right) The N-H bending in PVA-LC shifted from 1559 cm^{-1} to 1565 cm^{-1} with a slight increase in intensity, indicating stronger hydrogen bonding and electrostatic interactions.

Additionally, thermal treatment can increase the crystallinity of PVA and trigger the hornification of TCNF [167], a process commonly attributed to forming new hydrogen bonds among adjacent cellulose fibrils and hydrophobic interactions [247]. We measured the crystallinity of PVA and PVA-LC coatings before and after thermal treatment through FTIR using equation 6.1. The crystallinity values were 58.5%, 60%, 59.3%, and 59% for PVA, PVA_TT, PVA-LC, and PVA-LC_TT coatings, respectively. Although thermal treatment resulted in a slight increase in crystallinity in PVA, the change was not significant. These results suggest that thermal treatment primarily improved the hydrogen bonding, electrostatic, and hydrophobic interactions, which contributed to reducing the free volume in the network structure[44].

6.3.5 Gas barrier properties and reinforcing mechanism

Table 6.2 shows the OTR value of PVA and PVA/LDH-CNF coatings. BP showed no barrier against oxygen; OTR value exceeded 77,000 cc/m^{2}day. Applying a PVA coating of 6.2 gsm on BP reduced the OTR values to 341 cc/m^{2}day at 0% RH by effectively covering the surface (see Figure 6.4). Incorporating 1 wt% LDH-CNF hybrids into PVA further reduced the OTR to 10.1 cc/m^{2}day. Nanoparticles improve gas permeability in polymers by creating a tortuous pathway that slows gas diffusion through the polymer film [196]. Our previous results showed that this tortuosity can be maximized by combining positively charged LDH and negatively charged TCNF, further improving oxygen gas barrier properties (Chapter 5). In the current study, using an IR dryer for fast drying could help maintain the alignment of LDH and TCNF after coating application while reducing coating penetration into the paper. These factors further reduced the oxygen permeability of the PVA-LC coating. Applying thermal treatment further reduced the OTR to 3.8 cc/m²day in PVA-LC coatings due to improved hydrogen bonds and electrostatic interactions.

Table 6.2 Coating weight, total thickness, and gas barrier properties of coatings

Sample	**Coating weight (g/m^2)**	**Total thickness (μm)**	**OTR (cc/m^2 day)**			**WVTR (g/m^2day)**
			0% RH	**50%RH**	**90% RH**	
BP	-	83.3 ± 1.7	no barrier	no barrier	no barrier	39
BP_PVA	6.4 ± 0.6	87.1 ± 2.1	341 ± 183	535 ± 223	n/a	23.1
BP_PVA-LC	5.2 ± 1.2	87.2 ± 4.2	10.1 ± 2.3	31 ± 28	n/a	17.7
BP_PVA_TT	6.4 ± 0.6	87.1 ± 2.1	219 ± 210	255 ± 205	>2500	19
BP_PVA-LC_TT	5.2 ± 1.2	87.2 ± 4.2	3.8 ± 3.5	9.5 ± 4.5	811 ± 24	10.4

Moisture negatively affects the oxygen barrier performance of PVA due to its plasticizing effect, which leads to swelling and relaxation of polymer chains. This effect increased the OTR of PVA coated paper to 535 cc/m²day at 50% RH. Incorporating LDH-TCNF reduced this detrimental effect by forming a stiff interlocked structure that restricts segmental flexibility and lowers dynamic free volume [206, 207, 248]. As a result, the OTR reduced to 31 ± 28 cc at %50 RH in PVA-LC.

After thermal treatment, PVA and PVA-LC coated paper exhibited lower OTR of 219 ± 210 and 9.5 ± 4.5 cc/m²day at %50 RH, respectively. At 90% RH, the PVA-coated paper lost its oxygen barrier performance; the OTR exceeded the instrument's limit. It was reported that the OTR of PVA increases 2500 times when going from 0% to 100% RH [249]. We managed to limit this increase by incorporating LDH-TCNF and thermal treatment; OTR was 811 cc/m²day at 90% RH for PVA-LC_TT. As demonstrated in Section 6.3.4, the thermal treatment promoted stronger hydrogen bonds and electrostatic interactions. Additionally, the hornification of TCNF upon heating likely reduced the free volume of the network structure and enhanced hydrophobicity [47]. These factors contributed to improving the resistance to humidity of thermally treated PVA-LC.

The water vapor permeability performance of coatings was also measured, and the results are listed in Table 6.2. The WVTR of BP was found to be as high as 35 g/(m^2-day) due to some uncovered spots on the paper surface. When PVA was applied, these spots were fully covered, reducing the WVTR to 23 g/(m^2-day). A further reduction to 17 g/(m^2-day) was observed in PVA-LC samples. This improvement is attributed to increased tortuosity, reduced free volume, and decreased segmental mobility within the coating. Also, thermal treatment further reduced the WVTR of both PVA and PVA-LC to 19 and 10.4 g/(m^2-day). Like the improvement in OTR at high RH, the increase in hydrophobicity, along with densifying the structure, helped to reduce the WVTR of thermal-treated coatings.

The coatings developed in this study exhibit comparable or better gas permeability than many high-barrier paper coatings reported in the literature (see Table 6.3). Most studies achieved similar or higher OTR and WVTR values with significantly higher coating weights (e.g., 26-145 g/m^2). A few studies report lower OTR and WVTR values than our PVA-LC coatings, but they use coating weights or thicknesses that are five to ten times higher than ours. Our results also outperform Al_2O_3-coated PE-paper, commonly used in food packaging applications [250].

Table 6.3 Literature overview of the gas barrier of various coatings on paper

Coating mixture	**Coating Thickness (µm)**	**Coating Weight (g/m^2)**	**OTR (cc/m^2 day) 23°C, %50 RH**	**WVTR (g/m^2 day) 23°C, %50 RH**	**Ref.**
PVA-LC	4	5.2	9;5	10.4	This study
Starch-PVA	6.5	9.4	23.9	38	[95]
Starch-glycerol/zein bilayer	100	145	262	299	[96]
Pigment coating-CNC-LDPE	23	26	10	8	[97]
LDPE – precoating and Al_2O_3	-	-	818	4.6	[98]
PVA-SiO_2-polydopamine	77.7	-	0.3	4.1 (37°C, %90RH)	[99]
Chitosan	3.5	5	17 (0 RH)	-	[100]
PVA-maleic acid-mica (Crosslinked)	-	12.2	0.1	162 (37°C, %90RH)	[101]
PVA-MFC-latex	40	15	6 (0 RH)	0.5	[94]
Chitosan	12	25	257	70	[102]

NC: Cellulose nanocrystal, PLA: Polylactic acid, LDPE: Low-density polyethylene, PVA: Polyvinyl alcohol, MFC: microfibrillated cellulose, SA: stearic acid

6.3.6 Mechanical Properties

Figure 6.7 shows the elongation at break and tensile index of the BP and the BP coated with PVA and PVA-LC, both before and after thermal treatment. BP elongated at a break of 3.8 ± 0.8% and a tensile index of 60.8 ± 8.8 Nm/g. The coated papers, BP_PVA and BP_PVA-LC, showed slight increases in elongation at break to 4.3 ± 0.5 and 4.2 ± 0.6%, respectively. Their tensile indices increased to 63.6 ± 8.5 Nm/g and 62.9 ± 8.4 Nm/g, respectively. However, these differences are not statistically significant (p-values > 0.05). All these suggest that the PVA and PVA-LC coatings do not significantly enhance the mechanical properties of base paper. After thermal treatment, elongation at break of both BP_PVA and BP_PVA-LC increased to 7 ± 0.8% and 7.1 ± 1.2%, respectively (p-values < 0.05). This suggests that the thermally treated samples exhibit greater flexibility than their untreated counterparts, allowing them to stretch more before breaking.

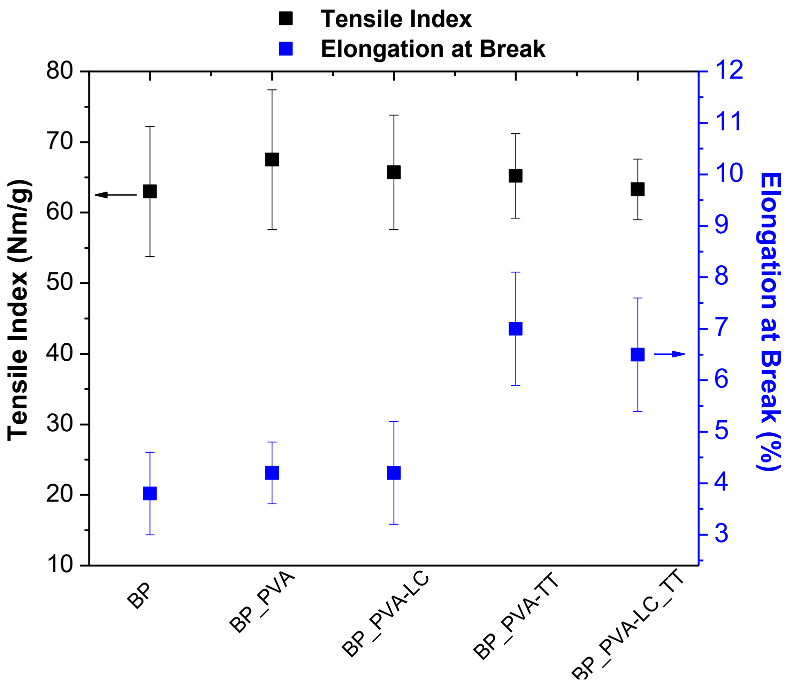

Figure 6.7 Tensile index and elongation at break of BP, BP_PVA, and BP_PVA-LC before and after thermal treatment

6.3.7 Repulpability of coated papers

The repulpability of coated papers is an essential factor in assessing their recyclability because it determines how effectively the paper fibers can be recovered. Figure 6.8a shows the repulpability rates of PVA and PVA-LC coated papers. Applying an LDPE coating yielded 82.5% recovery of pulp. PVA and PVA-LC coatings did not negatively affect the repulpability of BP and exhibited high repulpability rates of 82% and 83.4%, respectively. Thermally treated PVA and PVA-LC samples also maintained high repulpability rates of %82.1 and %82.4, respectively. These results suggest that both PVA and PVA-LC coatings are easily removed during the repulping process. Two main factors contribute to these findings: the water solubility of the PVA-based coatings and their relatively low coating weight. Since PVA and PVA-LC can dissolve in water, the coatings break down easily during repulping, preventing the formation of insoluble residues that could hinder fiber recovery. Their low coating weights limit significant penetration into the paper, reducing the risk of forming stickies. This facilitated easier fiber separation during repulping.

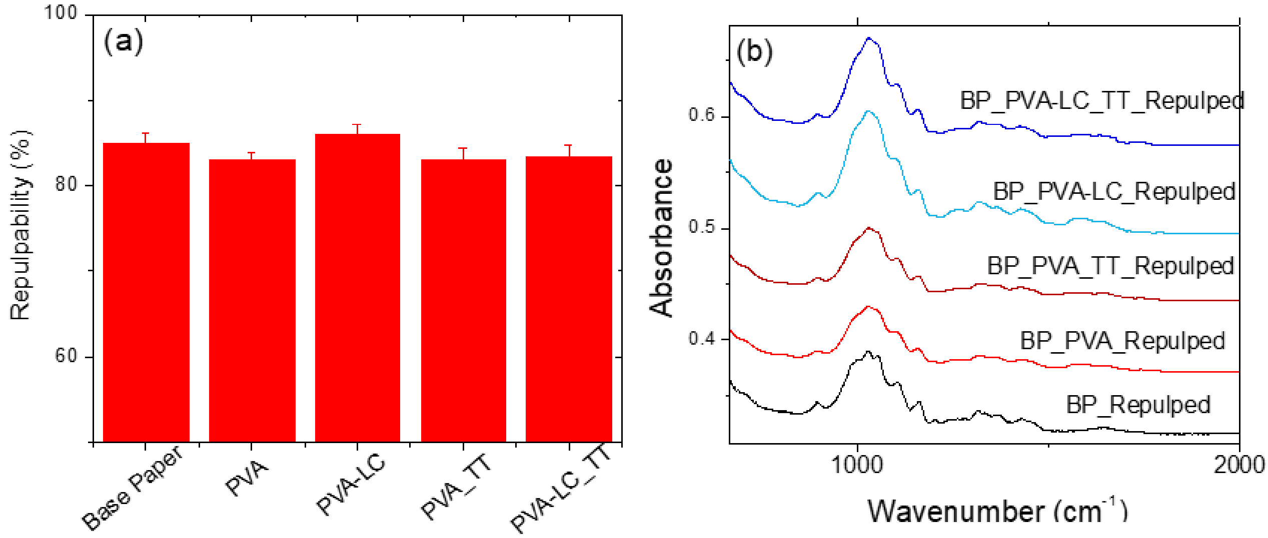

Figure 6.8 Repulpability rates of base paper (BP), PVA, and PVA-LC coated BP after and before thermal treatment (TT) at 130°C for 90 minutes. (b) FTIR spectrum of repulped base paper, PVA, and PVA-LC coated papers after and before thermal treatment at 130 C for 90 minutes. Both base and coated papers show a similar FTIR spectrum after repulping, confirming that coatings were removed during the repulping process.

Further evidence of the removal of PVA and PVA-LC from the paper was provided by FTIR analysis. The spectra of the recycled pulp showed the absence of peaks associated with PVA (e.g., C–O stretching of alcohol groups at 1085–1145 cm^{-1}, O–H bending at 1423 cm^{-1}, C=O stretching at 1560-1600 cm^{-1}), and PVA-LC (e.g., M–O Stretching: at 716 m^{-1}, C–O stretching of alcohol groups at 1085–1145 cm^{-1}, O–H bending at 1423 cm^{-1}, C=O stretching at 1560-1600 cm^{-1}), confirming that both coatings were successfully removed during the washing process with water.

This indicates that the PVA and PVA-LC coatings can be removed entirely from the pulp after repulping.

6.4 Conclusion

In this study, we combined positively charged LDH and negatively charged TNCF inside PVA to obtain high gas barrier coatings that can be easily recycled. The LDH-TCNF combination increased the viscosity of the PVA, which contributed to a reduction in penetration into the paper substrate. The water retention properties of TCNF and interactions between LDH-TCNF and the paper substrate also minimize coating penetration into paper. We also observed no blistering in PVA-LDH-TCNF, which occurred in some spots when we applied PVA alone.

OTR was reduced to 10.1 cc/m²day at 0% RH and 31.8 cc/m²day at 50% relative humidity. These improvements were due to the increased tortuosity, reduced free volume, and restricted segmental mobility within the coating with the introduction of the LDH-TCNF hybrid. Thermal treatment further improved barrier performance at 0%, 50%, and 90% RH, suggesting that heat treatment can optimize the structure of the LDH-TCNF system. The lowest OTR value of 3.78 cc/m²/day at 0% RH was achieved in the PVA-LDH-TCNF coating after thermal treatment at 130°C for 90 minutes. Coated papers show high repulpability rates of %82 and %83. This study provides valuable insights into the design of high-barrier, recyclable coatings for flexible paper packaging, offering a promising solution for improved packaging sustainability.

6.5 Acknowledgments

The authors gratefully acknowledge the financial support of 3SPack NSERC Industrial Research Chair by the Natural Science and Engineering Council of Canada (NSERC) and ProAmpac Inc. Compa.

CHAPTER 7 GENERAL DISCUSSIONS

Recyclable paper packaging has become popular due to environmental concerns. However, current solutions such as multilayer packaging, metallization, aluminum foils, or waxes represent recyclability challenges in paper packaging. Water-based barrier coatings (WBBC) are a promising solution for producing high-barrier recyclable packaging for paper and plastic substrates. WBBC consists of micro or nanoparticles (i.e., filler or pigment), binder (mostly water-soluble or water-dispersible polymers), rheology modifiers, stabilizers, and other additives. In this work, we synthesized a new type of synthetic high aspect ratio nanoparticle (or pigment), namely LDH, for WBBC applications. We later combined synthesized LDH with TCNF inside PVA. TCNF had multiple roles; it reinforced the gas barrier properties and acted as a rheology modifier, stabilizer, and water retention aid.

In the field of LDH synthesis, much attention was paid to the effect of synthesis parameters on the morphology or lateral sizes of LDH, especially when using co-precipitation methods. Herein, we used a calcination-rehydration approach through hydrothermal treatment. This approach has been used to synthesize various nanoparticles such as graphene, carbon nanotube, and metallic nanoparticles. However, systematic investigation of the effects of hydrothermal conditions (e.g., pH, temperature, and time) has not been focused on the aspect ratio of LDH. We chose the calcination-reconstruction approach, as using metal oxides as an LDH precursor can be studied from a green chemistry approach, as the lower amount of chemicals and the desired interlayer anion can be used compared to the co-precipitation method.

We have shown that optimizing the hydrothermal conditions is essential to obtain high aspect ratio LDHs in the presence of glycine. We revealed that hydrothermal treatments may affect the aspect ratio of LDH in two ways: influencing glycine-LDH (or pre-LDH particles) interactions and affecting the recrystallization and dissolution of LDHs. High concentrations of glycine were used as the dielectric constant of water-glycine solution scales with amino acid concentrations. We chose pH 6 and pH 9.5 because glycine has different charges at those pH values which could affect the interactions with LDH sheets. The best conditions for obtaining a high aspect ratio LDH were pH ~6, temperature 100 °C, and 5 days of reconstruction time.

However, obtaining ultra-high aspect ratio (e.g., higher than 500) LDHs was challenging even in optimized conditions. The reason can be the morphology and size of the precursor (i.e., metal oxides), which might result in smaller diameter LDHs or re-stacking of LDH during the sample preparation of LDHs for aspect ratio measurements. It’s also been reported that ultra-high aspect ratio can be obtained way longer times (e.g., 100 days) than the reconstruction times we studied.

However, we still obtained low oxygen permeability when we applied various aspect ratio LDHs on negatively charged PET. The oxygen barrier was comparable to high-barrier polymers such as EVOH when the highest aspect ratio LDH was applied on PET. Therefore, we showed another exciting aspect of applying glycine intercalated-LDH in coatings: their ability to arrange themselves in the form of thin films on a PET film. The oxygen barrier performance of LDH coatings on PET was comparable to commercial high-barrier polymers. On the other hand, LDH coatings alone may be sensitive to mechanical stress and might suffer from poor sealibility like most other nanoparticle coatings. In this context, PVA and TCNF introduced the coating mixture in the following parts of the project.

To prepare WBBC, we mixed the high aspect ratio LDH with oppositely charged TCNF inside PVA. The purpose was to benefit from electrostatic interactions while bringing extra functionality to coating formulation, such as modifying rheology or stabilizing LDHs in an aqueous coating mixture. We observed that TCNF and PVA prevented the long-term sedimentation inside water through electro-steric stabilization. TCNF, however, still did not help to obtain thoroughly exfoliated LDH inside PVA. In various hybrid nanoparticle systems, it has been reported that one nanoparticle might help to exfoliate the other one. Although we applied optimal conditions for ultrasonication, we obtained a slight change in the d-spacing of LDH after adding either PVA or TCNF. Using different types of mixing methods, such as high-pressure homogenizer for coating mixture preparation, might help to increase the efficiency of exfoliation; but we could also be beyond the concentration (concentrations of LDH were wt.% 10 and wt.% 20 with respect to PVA) of obtaining highly exfoliated structure.

It should also be noted that although XRD is useful for determining the spacing between nanoclay layers, it provides limited information about the distribution of nanoparticles or any structural irregularities. Therefore, although a thoroughly exfoliated LDH structure could not be achieved, the spatial distribution of LDH might be affected by TCNF, and this distribution change can affect the final barrier performance. However, we could not investigate this due to the project's time limitations.

Characterizing the LDH orientation sheds light on the effect of TCNF and electrostatic interaction on the nanoclay orientation. The orientation of LDH inside PVA slightly improved with the addition of TCNF. Higher viscosity and electrostatic interactions in PVA/LDH-TCNF might help keep LDH in a highly orientated state during coating application on PET. We need to mention that the stabilization, dispersion, and orientation of TCNF would also be affected by the presence of LDH. However, it was not the focus of the project. We also believe it would have less effect on barrier performance than LDH.

In the last chapter, we apply PVA and PVA-LDH-TCNF on paper substrates. In the paper coating process, the drying of the coating mixture (fast drying through IR) and substrate structure (porosity, roughness, surface chemistry, etc.) differed from the second part of the study, where PET was used as a substrate, and drying took place at room temperature. These parameters could significantly change the film formation, coating structure, and final performance of coatings. We aimed to understand how each component (LDH, PVA, TCNF) functions and the synergistic effect of combining these oppositely charged particles on the paper coating process and characteristics. We showed that TCNF-LDH hybrids function as rheology modifiers and water retention agents due to their intrinsic characteristics and their network structure.

Coating with the polymer solution aims to achieve a homogenous layer of constant thickness with a closed surface. The layer thickness of PVA must be sufficient to exceed the roughness of the paper substrate. On the other hand, low coating weights are necessary for easier recyclability and to reduce the cost of final paper packaging. When we applied low coating weights of 2-3 g/m^2, we measured unstable OTR values of ~220 and ~15.000 cc/day (not reported in articles). Any uncovered spot or variety in coating thickness in the paper coating can cause a significant increase in OTR values. Therefore, we increased the coating weight to 5-6 g/m^2 to cover the paper surface fully. These coating weights were still low compared to many studies on paper coatings.

Defects and blistering are the main problems in paper coatings due to the fast drying and rough surface of the paper. If the viscosity of coating dispersion is too high, trapped air or gases cannot escape easily, and blister occurs. If the viscosity of coating dispersion is too low, it may not adequately encapsulate and hold the gases until they dissipate, and blistering occurs. The presence of LDH-CNF nanoparticles increased the viscosity of PVA (to the optimum value for paper coatings) and cohesive strength at elevated temperatures (during drying), which helped us to prevent blistering formation.

When the coating is applied to paper, it must immobilize quickly to prevent penetration into the porous substrate. Faster drying leads to a more uniform surface film. The solid content of the solution, which affects viscosity, must also be optimized as it impacts coating penetration. Although increasing solid content can reduce penetration, it may also alter the particle interactions, stability, and dispersion. However, studying the effects of solid content was beyond this project's scope.

Water retention is often forgotten or ignored in paper coating studies. It refers to the coating's ability to control water absorption into the substrate during application and drying. TCNF has a very high capacity for water retention due to its large surface area and abundant hydroxyl groups. The TEMPO-oxidation introduces carboxyl groups on the cellulose structure and thus enhances its water retention capacity. Higher water retention can allow the wet coating layer to reorganize and form a more uniform, improving the overall quality. It can also reduce the penetration of the coating into paper. However, it also prolongs drying times and reduces machine speed in industrial applications. Thus, the water retention of our PVA-LC coating may need to be re-evaluated and adjusted during the upscaling of this formulation.

On the other hand, lower water retention of PVA —compared to PVA-LC— could cause rapid water evaporation and penetration into paper. This can lead to coating inconsistencies, defects, and, in some cases, reduced wet strength of the paper substrate. Rapid water loss causes runnability issues, especially during high-speed coating processes in industrial applications.

Permeability tests were the main experiments in this project. Both oxygen and water vapor permeability tests take several days. The MOCON device tested two films simultaneously, but maintaining the relative humidity at the same value is very important, as slight variations impacted the results. Testing low oxygen permeability involved a two-phase process: nitrogen first, then oxygen, requiring at least two days for accurate data. We had additional challenges, including ensuring proper sealing, preventing leakage, and avoiding defects like pinholes, especially when the paper coating was used as a sample. All of those could affect the accuracy of the tests. This extended testing time and ensuring properly coated sample and test conditions were the most time-consuming steps of this work.

CHAPTER 8 CONCLUSIONS AND RECOMMENDATIONS

8.1 Conclusions

In this dissertation, we developed a high water-based barrier LDH-based coatings for PET and paper substrates. The focus was on the synthesis mechanism of LDH, the synergistic effect of combining LDH and TCNF in PVA, and their application on PET and paper. The choice of LDH was mainly based on its easy and green synthesis with a high aspect ratio, non-toxicity, and rigid structure that limits its bending, folding, and defects.

We clearly showed the importance of the state of glycine anion as well as the time, temperature, and pH of the synthesis method in developing high aspect ratio LDH. The nanosheet thickness decreases, and diameter increases with increasing reconstruction time from 1 day to 5 days. We observe a limiting nanosheet aspect ratio of ca. 200 ± 22. These LDH-glycine gels can be used directly or dispersed in PVA to give a water-based dispersion that can be used to coat flexible polymeric films. We observed a similar trend in the OTR of PVA filled with various aspect ratio LDHs (not shown in articles) when we applied pure LDH-glycine gels to PET; the higher the aspect ratio, the lower the oxygen permeability.

The coatings we developed in the second objective were based on PVA-LDH, PVA-TCNF, and PVA-LDH-TCNF. The focus was the effect of electrostatic interactions between LDH-TCNF on the final morphology and structure of coatings. PVA was chosen due to its good film-forming, heat sealability, high oxygen barrier, and water solubility. It is easier to wash out these kinds of coatings from any substrate, which makes recyclability more practical than any other material and approach. We expected that negatively charged TCNF would improve the gas barrier performance through electrostatic interactions and interlocked network structure. Using negatively charged TCNF helped improve the stability of LDH in PVA. These three components formed an interlocked network structure, which led to higher complex viscosity and storage modulus at lower angular frequency in rheology measurements. We have shown that LDH-TCNF had a synergistic effect on oxygen permeability at 0 and 60% RH. They were also more durable after being flexed by using the Gelbo flex instrument. They exhibited more excellent mechanical resistance compared to the commercially available metalized package (18.15 ± 4.5 $cc \cdot m^{-2} \cdot day^{-1}$ with 46 µm thickness).

We further showed that these hybrids can be successfully applied to a paper substrate. Adding LDH-TCNF to PVA modified the water retention and rheology, hindering the blister and overpenetration of the coating into paper. These are fundamental features a barrier coating for paper is supposed to have. We obtained low oxygen permeability and water vapor permeability with these hybrid coatings and thermal treatment further improved their barrier performance.

One of the biggest challenges in current barrier coating systems such as metallization, wax, latex, or multilayer lamination is the separation of paper pulp from the coating materials. WBBC can reduce these problems as they can be applied with lower coating weights and washed-out during recycling due to their water solubility. In the last part of this study, we found that developed PVA-LDH-TCNF coatings can be removed from paper. Limited penetration into paper and their low coating weights helped us remove them from the paper.

PVA-LDH-TCNF coatings on PET (red star) and paper (yellow start) have shown comparable barrier performance to current barrier polymers such as PA and EVOH, as shown in Figure 8.1. They can be used for most food packaging applications requiring low gas permeability, such as nuts and snacks, meat, and coffee.

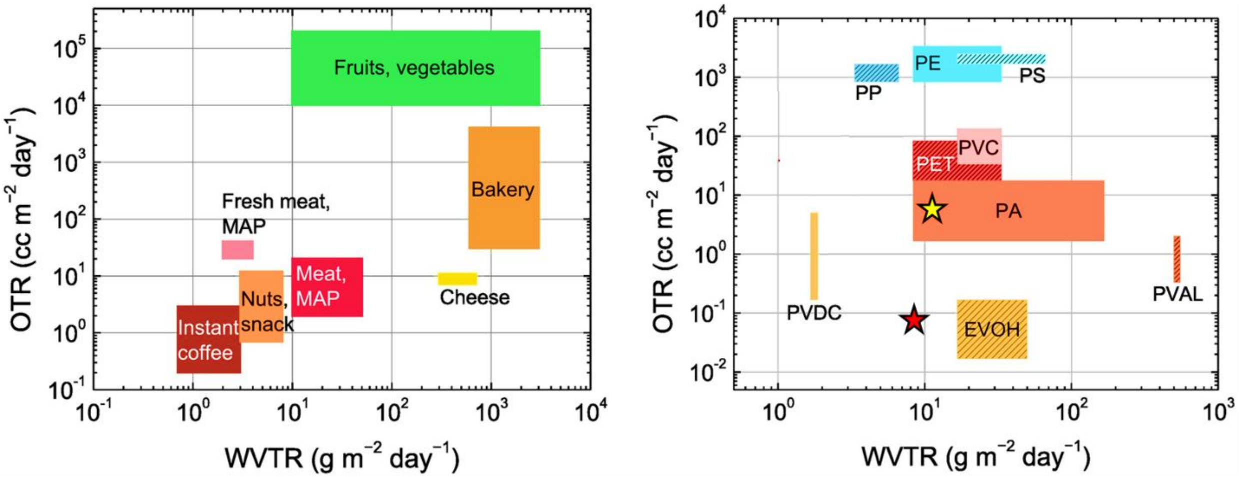

Figure 8.1 High barrier applications and commonly used polymers. The red star represents PVA-LDH-TCNF coating on PET, and the yellow star represents PVA-LDH-TCNF coating on paper. [218]

This work provides a fundamental understanding of high aspect ratio LDH synthesis and the application of TCNF-LDH hybrids in water-based coatings. It can be an important guideline for designing novel coating formulations for paper packaging.

8.2 Original Contributions

Several significant scientific contributions of this work are listed below.

In the first part of this research study:

- We demonstrate how the hydrothermal treatment conditions, such as pH, reconstruction time, and temperature, can impact the interactions between interlayer anions (specifically glycine) and LDH using rheology, FTIR, and XRD techniques.
- The mechanism of forming high-aspect-ratio LDH in the presence of glycine was systematically uncovered.
- We successfully developed high-barrier coatings using high-aspect-ratio LDH on PET substrates, marking the first instance of such coatings being applied.

In the second part of this study:

- A systematic study investigated the electrostatic interactions of oppositely charged LDH-TCNF through sedimentation, rheological, and X-ray diffraction methods.
- The reinforcement mechanism of PVA-LDH-TCNF composites was revealed, mainly focusing on their enhanced gas barrier properties at different conditions
- For the first time, TCNF-LDH-PVA coatings were developed on PET substrates, achieving exceptional barrier properties.

In the third part of this study:

- We uncovered the critical role of LDH and TCNF in influencing the penetration behavior into paper substrates
- It was demonstrated that LDH-TCNF can hinder blister formation
- High oxygen and water vapor barrier at low coating weight while maintaining the repulpability were demonstrated for the first time
- For the first time, hornification in cellulose/nanocellulose systems was applied in a nanoparticle formulation, opening new possibilities for coating technology.

8.3 Recommendation

The previous section briefly described the accomplished work during this thesis and summarized the main achievements. For future research and as a continuation of this work, the following subjects are recommended:

- Using a solvent mixture (such as water with ethanol or another compatible co-solvent) to improve the interaction between the LDH, glycine, and PVA, TCNF. Solvents can help weaken the interaction between the LDH layers and promote exfoliation.
- Longer reconstruction times for LDH synthesis can increase the aspect ratio, which would be beneficial for high-barrier applications.
- Modifying the hydrothermal treatment with an additional mixing step would improve the more homogenous crystallization of layered metal oxides into high-aspect-ratio LDHs.
- The concept of creating an electrostatically interlocked structure for barrier coatings can be applied to other hybrid nanoparticle systems, such as LDH with other cellulose derivatives or negatively charged particles. It would be interesting to demonstrate this idea and study how this research may be adapted to them.
- Using modified (or developed new) permeability models that consider interfacial and electrostatic interactions, crystallinity, and morphological changes and comparing them with existing permeability models would be an excellent study to justify the importance of these features.
- Exploring crosslinkers with various crosslinking densities and correlating this with the recyclability of coatings would be important to know.
- It would be interesting to study our approach compared with the LbL approach, which has a few layers of LDH and TCNF on top of PVA. Applying these coatings through a roll-to-roll approach would also improve the coating quality and final barrier performance.
- Increasing the solid content of prepared water-based coatings would be interesting to study as it can directly affect the viscosity, penetration, defects, and coating quality. It would also be worth exploring the possibility of using concentrated coatings by reducing their viscosity, e.g., using a surfactant or plasticizer.
- Studying other recyclability standards and assessing biodegradability combined with life cycle analysis would be interesting in showing the sustainability of these coatings.
- The folding effect on the barrier performance can be systematically investigated for paper-based coatings.

REFERENCES

1. Deshwal, G.K., N.R. Panjagari, and T. Alam, *An overview of paper and paper based food packaging materials: health safety and environmental concerns.* Journal of food science and technology, 2019. **56**: p. 4391-4403.
2. Stöter, M., et al., *Nanoplatelets of sodium hectorite showing aspect ratios of≈ 20 000 and superior purity.* Langmuir, 2013. **29**(4): p. 1280-1285.
3. Sun, L., et al., *Preparation of exfoliated epoxy/α-zirconium phosphate nanocomposites containing high aspect ratio nanoplatelets.* Chemistry of Materials, 2007. **19**(7): p. 1749-1754.
4. Morgan, A.B., L.L. Chu, and J.D. Harris, *A flammability performance comparison between synthetic and natural clays in polystyrene nanocomposites.* Fire and Materials: An International Journal, 2005. **29**(4): p. 213-229.
5. Coltelli, M.-B., et al., *State of the art in the development and properties of protein-based films and coatings and their applicability to cellulose based products: An extensive review.* Coatings, 2016. **6**(1): p. 1.
6. Kirwan, M.J., *Paper and paperboard packaging.* Food packaging technology, 2003. **241**.
7. Samyn, P., *Wetting and hydrophobic modification of cellulose surfaces for paper applications.* Journal of Materials Science, 2013. **48**(19): p. 6455-6498.
8. Nyström, D., et al., *Superhydrophobic and Self-Cleaning Bio-Fiber Surfaces via ATRP and Subsequent Postfunctionalization.* ACS Applied Materials & Interfaces, 2009. **1**(4): p. 816-823.
9. Balu, B., V. Breedveld, and D.W. Hess, *Fabrication of "Roll-off" and "Sticky" Superhydrophobic Cellulose Surfaces via Plasma Processing.* Langmuir, 2008. **24**(9): p. 4785-4790.
10. Lee, D.I., *Latex applications in paper coating*, in *Polymeric Dispersions: Principles and Applications*. 1997, Springer. p. 497-513.
11. Rabnawaz, M., et al., *A roadmap towards green packaging: the current status and future outlook for polyesters in the packaging industry.* Green Chemistry, 2017. **19**(20): p. 4737-4753.
12. Hamdani, S.S., et al., *Zein and PVOH-Based Bilayer Approach for Plastic-Free, Repulpable and Biodegradable Oil-and Water-Resistant Paper as a Replacement for Single-Use Plastics.* Industrial & Engineering Chemistry Research, 2020. **59**(40): p. 17856-17866.
13. Stevens, B.E., *Layer-By-Layer Assembly of Thin Platelet-Polymer Conductive Barrier Films*. 2015.
14. Millington, R., *Gas diffusion in porous media.* Science, 1959. **130**(3367): p. 100-102.

15. Ben Dhieb, F., et al., *Comparison of Crosslinking Efficiency in Dip and Roll-Deposited Coatings on Their Oxygen Barrier.* ACS Omega, 2019. **4**(14): p. 15772-15779.
16. Dhieb, F.B., et al., *Effect of nanoclay orientation on oxygen barrier properties of LbL nanocomposite coated films.* RSC advances, 2019. **9**(3): p. 1632-1641.
17. Bhunia, K., S. Dhawan, and S.S. Sablani, *Modeling the Oxygen Diffusion of Nanocomposite-based Food Packaging Films.* Journal of food science, 2012. **77**(7): p. N29-N38.
18. Sekelik, D., et al., *Oxygen barrier properties of crystallized and talc-filled poly (ethylene terephthalate).* Journal of Polymer Science Part B: Polymer Physics, 1999. **37**(8): p. 847-857.
19. Soltani, I., *Using Layer-by-Layer Coating and Nanocomposite Technologies to Improve the Barrier Properties of Polymeric Materials.* 2015.
20. Kumar, V., et al., *Roll-to-Roll Processed Cellulose Nanofiber Coatings.* Industrial & Engineering Chemistry Research, 2016. **55**(12): p. 3603-3613.
21. Huang, H.-D., et al., *High barrier graphene oxide nanosheet/poly(vinyl alcohol) nanocomposite films.* Journal of Membrane Science, 2012. **409-410**: p. 156-163.
22. Unalan, I.U., et al., *Exceptional oxygen barrier performance of pullulan nanocomposites with ultra-low loading of graphene oxide.* Nanotechnology, 2015. **26**(27): p. 275703.
23. Nguyen, H.L., et al., *Sustainable Boron Nitride Nanosheet-Reinforced Cellulose Nanofiber Composite Film with Oxygen Barrier without the Cost of Color and Cytotoxicity.* Polymers (Basel), 2018. **10**(5): p. 501.
24. Ren, F., et al., *Ultra-low gas permeable cellulose nano fi ber nanocomposite fi lms fi lled with highly oriented graphene oxide nanosheets induced by shear field.* Carbohydr Polym, 2019. **209**: p. 310-319.
25. Spoljaric, S., et al., *Nanofibrillated Cellulose, Poly(vinyl alcohol), Montmorillonite Clay Hybrid Nanocomposites With Superior Barrier and Thermomechanical Properties.* Polymer Composites, 2014. **35**(6): p. 1117-1131.
26. Ferrer, A., L. Pal, and M. Hubbe, *Nanocellulose in packaging: Advances in barrier layer technologies.* Industrial Crops and Products, 2017. **95**: p. 574-582.
27. Fukuzumi, H., et al., *Transparent and High Gas Barrier Films of Cellulose Nanofibers Prepared by TEMPO-Mediated Oxidation.* Biomacromolecules, 2009. **10**(1): p. 162-165.
28. Dou, Y.B., et al., *Transparent, Flexible Films Based on Layered Double Hydroxide/Cellulose Acetate with Excellent Oxygen Barrier Property.* Advanced Functional Materials, 2014. **24**(4): p. 514-521.
29. Kim, S.J., et al., *Fabrication of graphene oxide/montmorillonite nanocomposite flexible thin films with improved gas-barrier properties.* RSC Advances, 2018. **8**(68): p. 39083-39089.
30. Olsson, E., et al., *Montmorillonite for starch-based barrier dispersion coating — Part 2: Pilot trials and PE-lamination.* Applied Clay Science, 2014. **97-98**: p. 167-173.

31. Priolo, M.A., et al., *Super Gas Barrier of Transparent Polymer−Clay Multilayer Ultrathin Films.* Nano Letters, 2010. **10**(12): p. 4970-4974.

32. Svagan, A.J., et al., *Transparent Films Based on PLA and Montmorillonite with Tunable Oxygen Barrier Properties.* Biomacromolecules, 2012. **13**(2): p. 397-405.

33. Yu, J., J.C. Buffet, and D. O'Hare, *Aspect Ratio Control of Layered Double Hydroxide Nanosheets and Their Application for High Oxygen Barrier Coating in Flexible Food Packaging.* ACS Appl Mater Interfaces, 2020. **12**(9): p. 10973-10982.

34. Guo, F., et al., *A review of the synthesis and applications of polymer–nanoclay composites.* Applied Sciences, 2018. **8**(9): p. 1696.

35. Yu, J., et al., *Synthesis of Layered Double Hydroxide Single-Layer Nanosheets in Formamide.* Inorganic Chemistry, 2016. **55**(22): p. 12036-12041.

36. Introzzi, L., et al., *Ultrasound-assisted pullulan/montmorillonite bionanocomposite coating with high oxygen barrier properties.* Langmuir, 2012. **28**(30): p. 11206-14.

37. Lam, C.-k., et al., *Effect of ultrasound sonication in nanoclay clusters of nanoclay/epoxy composites.* Materials Letters, 2005. **59**(11): p. 1369-1372.

38. Park, J. and S.C. Jana, *Effect of Plasticization of Epoxy Networks by Organic Modifier on Exfoliation of Nanoclay.* Macromolecules, 2003. **36**(22): p. 8391-8397.

39. Adachi-Pagano, M., C. Forano, and J.-P. Besse, *Delamination of layered double hydroxides by use of surfactants.* Chemical Communications, 2000(1): p. 91-92.

40. Yu, J., et al., *Preparation of two dimensional layered double hydroxide nanosheets and their applications.* Chemical Society Reviews, 2017. **46**(19): p. 5950-5974.

41. Li, X.Y., et al., *Two-dimensional materials modified layered double hydroxides: A series of fillers for improving gas barrier and permselectivity of poly(vinyl alcohol).* Composites Part B-Engineering, 2021. **207**: p. 108568.

42. Wang, J., et al., *Moisture-Permeable, Humidity-Enhanced Gas Barrier Films Based on Organic/Inorganic Multilayers.* ACS Applied Materials & Interfaces, 2018. **10**(33): p. 28130-28138.

43. Larocca, N., R. Filho, and L. Pessan, *Influence of layer-by-layer deposition techniques and incorporation of layered double hydroxides (LDH) on the morphology and gas barrier properties of polyelectrolytes multilayer thin films.* Surface and Coatings Technology, 2018. **349**.

44. Kim, T., et al., *Crab-on-a-Tree: All Biorenewable, Optical and Radio Frequency Transparent Barrier Nanocoating for Food Packaging.* ACS Nano, 2019. **13**(4): p. 3796-3805.

45. Ren, F., et al., *Ultra-low gas permeable cellulose nanofiber nanocomposite films filled with highly oriented graphene oxide nanosheets induced by shear field.* Carbohydrate Polymers, 2019. **209**: p. 310-319.

46. Bardet, R., et al., *Substitution of nanoclay in high gas barrier films of cellulose nanofibrils with cellulose nanocrystals and thermal treatment.* Cellulose, 2015. **22**(2): p. 1227-1241.

47. Sharma, S., et al., *Thermally enhanced high performance cellulose nano fibril barrier membranes.* RSC Advances, 2014. **4**(85): p. 45136-45142.

48. Huang, H.-D., et al., *Ultra-low gas permeability and efficient reinforcement of cellulose nanocomposite films by well-aligned graphene oxide nanosheets.* Journal of Materials Chemistry A, 2014. **2**(38): p. 15853-15863.

49. Xu, P.-P., et al., *Highly Efficient Three-Dimensional Gas Barrier Network for Biodegradable Nanocomposite Films at Extremely Low Loading Levels of Graphene Oxide Nanosheets.* Industrial & Engineering Chemistry Research, 2020. **59**(13): p. 5818-5827.

50. Abdullah, Z.W., et al., *Water and gas barrier properties of polyvinyl alcohol (PVA)/starch (ST)/ glycerol (GL)/halloysite nanotube (HNT) bionanocomposite films: Experimental characterisation and modelling approach.* Composites Part B: Engineering, 2019. **174**: p. 107033.

51. Goh, K., et al., *Sandwich-Architectured Poly(lactic acid)-Graphene Composite Food Packaging Films.* ACS Appl Mater Interfaces, 2016. **8**(15): p. 9994-10004.

52. Thuy, V.T.T., et al., *Sustainable, self-cleaning, transparent, and moisture/oxygen-barrier coating films for food packaging.* Green Chemistry, 2021. **23**(7): p. 2658-2667.

53. Chen, J.-T., et al., *Enhancing polymer/graphene oxide gas barrier film properties by introducing new crystals.* Carbon, 2014. **75**: p. 443-451.

54. Uysal Unalan, I., et al., *Graphene Oxide Bionanocomposite Coatings with High Oxygen Barrier Properties.* Nanomaterials (Basel, Switzerland), 2016. **6**(12): p. 244.

55. Lim, M., et al., *Highly-enhanced water resistant and oxygen barrier properties of cross-linked poly(vinyl alcohol) hybrid films for packaging applications.* Progress in Organic Coatings, 2015. **85**: p. 68-75.

56. Yeun, J.-H., et al., *Poly(vinyl alcohol) nanocomposite films: Thermooptical properties, morphology, and gas permeability.* Journal of Applied Polymer Science, 2006. **101**(1): p. 591-596.

57. Yang, Y.-H., et al., *Super Gas Barrier and Selectivity of Graphene Oxide-Polymer Multilayer Thin Films.* Advanced Materials, 2013. **25**(4): p. 503-508.

58. Dou, Y., et al., *Transparent, Ultrahigh-Gas-Barrier Films with a Brick-Mortar-Sand Structure.* Angew Chem Int Ed Engl, 2015. **54**(33): p. 9673-8.

59. Maxwell, J.C., *A treatise on electricity and magnetism*. Vol. 1. 1873: Clarendon press.

60. Rayleigh, L., *LVI. On the influence of obstacles arranged in rectangular order upon the properties of a medium.* The London, Edinburgh, and Dublin Philosophical Magazine and Journal of Science, 1892. **34**(211): p. 481-502.

61. Cussler, E., et al., *Barrier membranes.* Journal of membrane science, 1988. **38**(2): p. 161-174.

62. Nielsen, L.E., *Models for the Permeability of Filled Polymer Systems.* Journal of Macromolecular Science: Part A - Chemistry, 1967. **1**(5): p. 929-942.

63. Bharadwaj, R.K., *Modeling the barrier properties of polymer-layered silicate nanocomposites.* Macromolecules, 2001. **34**(26): p. 9189-9192.

64. Chatterjee, A., P. Bharadiya, and D. Hansora, *Layered double hydroxide based bionanocomposites.* Applied Clay Science, 2019. **177**: p. 19-36.

65. Benito, P., et al., *Effect of post-synthesis microwave–hydrothermal treatment on the properties of layered double hydroxides and related materials.* Applied Clay Science, 2010. **48**(1): p. 218-227.

66. Xu, Z.P., et al., *Dispersion and Size Control of Layered Double Hydroxide Nanoparticles in Aqueous Solutions.* The Journal of Physical Chemistry B, 2006. **110**(34): p. 16923-16929.

67. Darr, J.A., et al., *Continuous hydrothermal synthesis of inorganic nanoparticles: applications and future directions.* Chemical reviews, 2017. **117**(17): p. 11125-11238.

68. Kumar, P. and R. Kumar, *6 - Synthesis process of functionalized ZnO nanostructure for additive manufacturing: a state-of-the-art review*, in *Additive Manufacturing with Functionalized Nanomaterials*, S. Singh and C.M. Hussain, Editors. 2021, Elsevier. p. 135-153.

69. Yu, J., et al., *High gas barrier coating using non-toxic nanosheet dispersions for flexible food packaging film.* Nat Commun, 2019. **10**(1): p. 2398.

70. Xu, Z.P. and G.Q. Lu, *Hydrothermal synthesis of layered double hydroxides (LDHs) from mixed MgO and Al2O3: LDH formation mechanism.* Chemistry of materials, 2005. **17**(5): p. 1055-1062.

71. Liu, Z., et al., *Synthesis, Anion Exchange, and Delamination of Co−Al Layered Double Hydroxide: Assembly of the Exfoliated Nanosheet/Polyanion Composite Films and Magneto-Optical Studies.* Journal of the American Chemical Society, 2006. **128**(14): p. 4872-4880.

72. Kang, H.L., et al., *Coassembly of Inorganic Macromolecule of Exfoliated LDH Nanosheets with Cellulose.* Journal of Physical Chemistry C, 2009. **113**(21): p. 9157-9163.

73. Kang, H., et al., *An effect of alginate on the stability of LDH nanosheets in aqueous solution and preparation of alginate/LDH nanocomposites.* Carbohydrate polymers, 2014. **100**: p. 158-165.

74. Privas, E., F. Leroux, and P. Navard, *Preparation and properties of blends composed of lignosulfonated layered double hydroxide/plasticized starch and thermoplastics.* Carbohydrate polymers, 2013. **96**(1): p. 91-100.

75. Mao, L., et al., *Poly (ε-caprolactone) filled with polydopamine-coated high aspect ratio layered double hydroxide: Simultaneous enhancement of mechanical and barrier properties.* Applied Clay Science, 2017. **150**: p. 202-209.

76. Demirkaya, Z.D., et al., *Comprehensive characterization of polylactide-layered double hydroxides nanocomposites as packaging materials.* Journal of Polymer Research, 2015. **22**(7): p. 1-13.

77. Pan, T., et al., *Remarkable oxygen barrier films based on a layered double hydroxide/chitosan hierarchical structure.* Journal of Materials Chemistry A, 2015. **3**(23): p. 12350-12356.

78. Ruengkajorn, K., et al., *Non-toxic layered double hydroxide nanoplatelet dispersions for gas barrier coatings on flexible packaging.* Materials Advances, 2021. **2**(8): p. 2626-2635.

79. Wang, L., et al., *Layer-by-layer assembly of layered double hydroxide/rubber multilayer films with excellent gas barrier property.* Composites Part A: Applied Science and Manufacturing, 2017. **102**: p. 314-321.

80. Wang, J., et al., *Hybrid films with excellent oxygen and water vapor barrier properties as efficient anticorrosive coatings.* RSC advances, 2018. **8**(38): p. 21651-21657.

81. Dou, Y., et al., *Humidity-triggered self-healing films with excellent oxygen barrier performance.* Chemical Communications, 2014. **50**(54): p. 7136-7138.

82. Yue, L., et al., *Epoxy composites with carbon nanotubes and graphene nanoplatelets – Dispersion and synergy effects.* Carbon, 2014. **78**: p. 268-278.

83. Liu, L. and J.C. Grunlan, *Clay Assisted Dispersion of Carbon Nanotubes in Conductive Epoxy Nanocomposites.* Advanced Functional Materials, 2007. **17**(14): p. 2343-2348.

84. Zuo, L., et al., *Graphene/montmorillonite hybrid synergistically reinforced polyimide composite aerogels with enhanced flame-retardant performance.* Composites Science and Technology, 2016. **139**.

85. Bhattacharya, M., et al., *Influence of the nanofiller type and content on permeation characteristics of multifunctional NR nanocomposites and their modeling.* Polymers for Advanced Technologies, 2012. **23**(3): p. 596-610.

86. Bilotti, E., et al., *Controlling the dynamic percolation of carbon nanotube based conductive polymer composites by addition of secondary nanofillers: The effect on electrical conductivity and tuneable sensing behaviour.* Composites Science and Technology, 2013. **74**: p. 85-90.

87. Sehaqui, H., et al., *Multifunctional Nanoclay Hybrids of High Toughness, Thermal, and Barrier Performances.* ACS Applied Materials & Interfaces, 2013. **5**(15): p. 7613-7620.

88. Song, S.H., *Synergistic Effect of Clay Platelets and Carbon Nanotubes in Styrene–Butadiene Rubber Nanocomposites.* Macromolecular Chemistry and Physics, 2016. **217**(23): p. 2617-2625.

89. Trifol, J., et al., *Hybrid poly (lactic acid)/nanocellulose/nanoclay composites with synergistically enhanced barrier properties and improved thermomechanical resistance.* Polymer International, 2016. **65**(8): p. 988-995.

90. Meng, X., et al., *Fabrication of transparent clay-polymer hybrid coatings on PET film to enhance flame retardancy and oxygen barrier properties.* Progress in Organic Coatings, 2020. **147**: p. 105788.

91. Yoo, J., et al., *Graphene oxide and laponite composite films with high oxygen-barrier properties.* Nanoscale, 2014. **6**(18): p. 10824-10830.

92. Sun, L., et al., *Nanocomposite coating system via one-step co-assembly*. 2022, Google Patents.

93. Schmidt, W., et al., *Receiving Layer for Digital Printing Methods Having Nanofibrillated Cellulose*. 2015, Google Patents.

94. Guezennec, C., *Développement de nouveaux matériaux d'emballage à partir de micro- et nanofibrilles de cellulose.*. 2012, Université de Grenoble.

95. Javed, A., et al., *Study of starch and starch-PVOH blends and effects of plasticizers on mechanical and barrier properties of coated paperboard.* Nordic Pulp & Paper Research Journal, 2016. **31**(3): p. 499-510.

96. Hamdani, S.S., et al., *Barrier and mechanical properties of biodegradable paper bilayer-coated with plasticized starch and zein.* Journal of Applied Polymer Science, 2023. **140**(8): p. e53440.

97. Koppolu, R., et al., *Continuous processing of nanocellulose and polylactic acid into multilayer barrier coatings.* ACS applied materials & interfaces, 2019. **11**(12): p. 11920-11927.

98. Hirvikorpi, T., et al. *Thin inorganic barrier coatings for packaging materials*. in *Proceedings of the PLACE 2010 Conference, Albuquerque, NM, USA*. 2010.

99. Chen, X., et al., *A novel paper-based composite film with enhanced oxygen and water vapor barrier properties.* Progress in Organic Coatings, 2024. **186**: p. 108042.

100. Kjellgren, H., et al., *Barrier and surface properties of chitosan-coated greaseproof paper.* Carbohydrate polymers, 2006. **65**(4): p. 453-460.

101. Jiang, K. and X. Wang, *Preparation and application of maleic acid crosslinked polyvinyl alcohol/mica coating for barrier paper.* Progress in Organic Coatings, 2022. **170**: p. 106937.

102. Ruberto, Y., et al., *Slot-die coating of cellulose nanocrystals and chitosan for improved barrier properties of paper.* Cellulose, 2024. **31**(6): p. 3589-3606.

103. Jiang, X., et al., *Preparation and characterization of degradable cellulose− based paper with superhydrophobic, antibacterial, and barrier properties for food packaging.* International Journal of Molecular Sciences, 2022. **23**(19): p. 11158.

104. Al-Gharrawi, M.Z., J. Wang, and D.W. Bousfield, *Improving Recycling of Polyethylene-Coated Paperboard with a Nanofibrillated Cellulose Layer.* BioResources, 2021. **16**(2).

105. Guest, D., *Recycling surface treated paper products*, in *Surface Application of Paper Chemicals*, J. Brander and I. Thorn, Editors. 1997, Springer Netherlands: Dordrecht. p. 229-257.

106. Popil, R.E. and M. Schaepe, *Comparative evaluation of the potential for wax-alternative packaging coatings.* Tappi journal, 2005. **4**(8): p. 25.

107. Bideau, B., E. Loranger, and C. Daneault, *Nanocellulose-polypyrrole-coated paperboard for food packaging application.* Progress in Organic Coatings, 2018. **123**: p. 128-133.

108. Parvathy, P. and S.K. Sahoo, *Hydrophobic, moisture resistant and biorenewable paper coating derived from castor oil based epoxy methyl ricinoleate with repulpable potential.* Progress in Organic Coatings, 2021. **158**: p. 106347.

109. Parris, N., et al., *Recyclable zein-coated kraft paper and linerboard.* Progress in paper recycling. Vol. 11, no. 3 (May 2002): Pages 24-29, 2002.

110. Kansal, D., et al., *Food-safe chitosan–zein dual-layer coating for water-and oil-repellent paper substrates.* ACS Sustainable Chemistry & Engineering, 2020. **8**(17): p. 6887-6897.

111. Zhang, H., et al., *PLA coated paper containing active inorganic nanoparticles: Material characterization and fate of nanoparticles in the paper recycling process.* Waste management, 2016. **52**: p. 339-345.

112. Song, H.G. and J. Han, *Hybrid organic-inorganic coating with enhanced oxygen- and UV-barrier performance: Polyelectrolyte complex based on sodium alginate, poly (vinyl alcohol), and reconstructed layered double hydroxide.* Int J Biol Macromol, 2024. **260**(Pt 1): p. 129335.

113. Xu, Z.P., et al., *Stable suspension of layered double hydroxide nanoparticles in aqueous solution.* Journal of the American Chemical Society, 2006. **128**(1): p. 36-37.

114. Bukhtiyarova, M.V., *A review on effect of synthesis conditions on the formation of layered double hydroxides.* Journal of Solid State Chemistry, 2019. **269**: p. 494-506.

115. Berber, M.R., et al., *Uniform nanoparticles of hydrotalcite-like materials and their textural properties at optimized conditions of urea hydrothermal treatment.* Journal of Molecular Structure, 2013. **1033**: p. 104-112.

116. Shi, R., et al., *Fabrication of porous microspheres and network arrays of Zn–Al hydrotalcite-like compounds on Al substrate via facile hydrothermal method.* Ceramics International, 2014. **40**(5): p. 6855-6863.

117. Zhang, Z., G. Chen, and K. Xu, *One-pot green hydrothermal synthesis of stearate-intercalated MgAl layered double hydroxides.* Applied Clay Science, 2013. **72**: p. 206-210.

118. Zadaviciute, S., K. Baltakys, and A. Bankauskaite, *The effect of microwave and hydrothermal treatments on the properties of hydrotalcite: A comparative study.* Journal of Thermal Analysis and Calorimetry, 2017. **127**: p. 189-196.

119. Matijevic, E., *Uniform inorganic colloid dispersions. Achievements and challenges.* langmuir, 1994. **10**(1): p. 8-16.

120. Albiston, L., et al., *Rheology and microstructure of aqueous layered double hydroxide dispersions.* Journal of Materials Chemistry, 1996. **6**(5): p. 871-877.

121. Joy, M., et al., *Layered double hydroxide using hydrothermal treatment: morphology evolution, intercalation and release kinetics of diclofenac sodium.* Frontiers of Materials Science, 2017. **11**: p. 395-408.

122. Gu, Z., et al., *Influence of hydrothermal treatment on physicochemical properties and drug release of anti-inflammatory drugs of intercalated layered double hydroxide nanoparticles.* Pharmaceutics, 2014. **6**(2): p. 235-248.

123. Cermelj, K., et al., *Layered double hydroxide nanosheets via solvothermal delamination.* Journal of Energy Chemistry, 2019. **35**: p. 88-94.

124. Zhao, Y., et al., *NiTi-layered double hydroxides nanosheets as efficient photocatalysts for oxygen evolution from water using visible light.* Chemical Science, 2014. **5**(3): p. 951-958.

125. Nakayama, H., N. Wada, and M. Tsuhako, *Intercalation of amino acids and peptides into Mg–Al layered double hydroxide by reconstruction method.* International journal of pharmaceutics, 2004. **269**(2): p. 469-478.

126. Iyi, N., et al., *Swelling and gel/sol formation of perchlorate-type layered double hydroxides in concentrated aqueous solutions of amino acid-related zwitterionic compounds.* Langmuir, 2013. **29**(8): p. 2562-2571.

127. Jobbagy, M. and N. Iyi, *Interplay of charge density and relative humidity on the structure of nitrate layered double hydroxides.* The Journal of Physical Chemistry C, 2010. **114**(42): p. 18153-18158.

128. Ma, R. and T. Sasaki, *Nanosheets of oxides and hydroxides: ultimate 2D charge-bearing functional crystallites.* Advanced materials, 2010. **22**(45): p. 5082-5104.

129. Li, B.-g., Y. Hu, and Z.-y. Chen, *Hydrothermal synthesis of exfoliative LDH in the presence of glycine.* Chinese Journal of Chemical Physics, 2006. **19**(3): p. 253.

130. Kloprogge, J.T., L. Hickey, and R.L. Frost, *The effects of synthesis pH and hydrothermal treatment on the formation of zinc aluminum hydrotalcites.* Journal of Solid State Chemistry, 2004. **177**(11): p. 4047-4057.

131. Ashok Kumar, R., et al., *Crystal growth, optical and thermal studies of nonlinear optical γ-glycine single crystal grown from lithium nitrate.* Optik, 2012. **123**(5): p. 409-413.

132. Yu, J., et al., *High gas barrier coating using non-toxic nanosheet dispersions for flexible food packaging film.* Nature communications, 2019. **10**(1): p. 2398.

133. Ellerbrock, R.H. and H.H. Gerke, *FTIR spectral band shifts explained by OM–cation interactions.* Journal of Plant Nutrition and Soil Science, 2021. **184**(3): p. 388-397.

134. Aisawa, S., et al., *Intercalation behavior of amino acids into Zn–Al-layered double hydroxide by calcination–rehydration reaction.* Journal of Solid State Chemistry, 2004. **177**(11): p. 3987-3994.

135. Izatt, R.M., et al., *Effect of temperature and pressure on the protonation of glycine.* Biophysical Journal, 1992. **61**(5): p. 1394-1401.

136. Sun, X. and S.K. Dey, *Insights into the synthesis of layered double hydroxide (LDH) nanoparticles: Part 2. Formation mechanisms of LDH.* Journal of Colloid and Interface Science, 2015. **458**: p. 160-168.

137. Zhao, Y., et al., *Selectivity of crystal growth direction in layered double hydroxides.* Tsinghua Science and Technology, 2004. **9**(6): p. 667-671.

138. Xu, Z.P. and P.S. Braterman, *High affinity of dodecylbenzene sulfonate for layered double hydroxide and resulting morphological changes.* Journal of Materials Chemistry, 2003. **13**(2): p. 268-273.

139. Ye, H., et al., *Regeneration mechanism, modification strategy, and environment application of layered double hydroxides: Insights based on memory effect.* Coordination Chemistry Reviews, 2022. **450**: p. 214253.

140. Nguyen, T., et al. *Effect of pH on the adsorption behaviour of Congo Red Dye on the Mg-Al layered double hydroxide*. in *IOP Conference Series: Materials Science and Engineering*. 2020. IOP Publishing.

141. Duan, X., et al., *Clean method for preparing layered double hydroxides*. 2012, Google Patents.

142. Tao, Q., et al., *Synthesis and characterization of layered double hydroxides with a high aspect ratio.* Journal of Solid State Chemistry, 2006. **179**(3): p. 708-715.

143. Zhuo, K., et al., *Dielectric Constants for Binary Amino Acid−Water Solutions from (278.15 to 313.15) K.* Journal of Chemical & Engineering Data, 2009. **54**(1): p. 137-141.

144. Sun, X., E. Neuperger, and S.K. Dey, *Insights into the synthesis of layered double hydroxide (LDH) nanoparticles: Part 1. Optimization and controlled synthesis of chloride-intercalated LDH.* Journal of colloid and interface science, 2015. **459**: p. 264-272.

145. Idris, A., A. Muntean, and B. Mesic, *A review on predictive tortuosity models for composite films in gas barrier applications.* Journal of Coatings Technology and Research, 2022. **19**(3): p. 699-716.

146. Roso, M., et al., *Experimental methods in chemical engineering: Barrier properties.* The Canadian Journal of Chemical Engineering, 2021. **99**(5): p. 1068-1081.

147. Malinowska, G., *Effect of the corona discharge treatment of polyester fabrics on their adhesive properties.* Fibres Text east eur, 2009. **17**: p. 98-102.

148. Grunlan, J.C., J.K. Choi, and A. Lin, *Antimicrobial behavior of polyelectrolyte multilayer films containing cetrimide and silver.* Biomacromolecules, 2005. **6**(2): p. 1149-1153.

149. Jamieson, E. and A. Windle, *Structure and oxygen-barrier properties of metallized polymer film.* Journal of Materials Science, 1983. **18**: p. 64-80.

150. Ji, Y., et al., *Aqueous-Based Recycling of Cellulose Nanocrystal/Chitin Nanowhisker Barrier Coatings.* ACS Sustainable Chemistry & Engineering, 2023. **11**(29): p. 10874-10883.

151. Li, H., et al., *Pre-grafted group on PE surface by DBD plasma and its influence on the oxygen permeation with coated SiOx.* Molecules, 2019. **24**(4): p. 780.

152. Guerritore, M., et al., *Recyclable-by-design mono-material flexible packaging with high barrier properties realized through graphene hybrid coatings.* Resources, Conservation and Recycling, 2022. **179**: p. 106126.

153. Wu, F., M. Misra, and A.K. Mohanty, *Challenges and new opportunities on barrier performance of biodegradable polymers for sustainable packaging.* Progress in Polymer Science, 2021. **117**: p. 101395.

154. Das, P., et al., *Nacre-mimetics with synthetic nanoclays up to ultrahigh aspect ratios.* Nat Commun, 2015. **6**(1): p. 5967.

155. Koshani, R., M. Tavakolian, and T.G.M. van de Ven, *Cellulose-based dispersants and flocculants.* J Mater Chem B, 2020. **8**(46): p. 10502-10526.

156. Ming, S.Y., et al., *Effective dispersion of aqueous clay suspension using carboxylated nanofibrillated cellulose as dispersant.* Rsc Advances, 2016. **6**(44): p. 37330-37336.

157. Ovaska, S.-S., *Oil and grease barrier properties of converted dispersion-coated paperboards.* 2016.

158. Johansson, C., L. Järnström, and A.-C. Hellgren, *Effects of carboxylation on polymer interdiffusion and water vapour permeability of latexes.* Nordic Pulp Paper Res. J., 17 (1),. 20-28 (2002), 2002.

159. Qi, D., Z. Cao, and U. Ziener, *Recent advances in the preparation of hybrid nanoparticles in miniemulsions.* Adv Colloid Interface Sci, 2014. **211**: p. 47-62.

160. Soares, D.C.F., et al., *Polymer-hybrid nanoparticles: Current advances in biomedical applications.* Biomedicine & Pharmacotherapy, 2020. **131**: p. 110695.

161. Perera, K.Y., S. Jaiswal, and A.K. Jaiswal, *A review on nanomaterials and nanohybrids based bio-nanocomposites for food packaging.* Food Chemistry, 2022. **376**: p. 131912.

162. Shin, J.Y., P.D. Fleming, and H.L. Lee, *Best pigment coating for a dual-purpose coated paper.* Journal of Coatings Technology and Research, 2021. **18**(5): p. 1281-1294.

163. Vatansever, E., et al., *Development of CNC-reinforced PBAT nanocomposites with reduced percolation threshold: a comparative study on the preparation method.* Journal of Materials Science, 2020. **55**: p. 15523-15537.

164. Xu, S.M., et al., *Nanocellulose-assisted dispersion of graphene to fabricate poly(vinyl alcohol)/graphene nanocomposite for humidity sensing.* Composites Science and Technology, 2016. **131**: p. 67-76.

165. Ming, S., et al., *Effective dispersion of aqueous clay suspension using carboxylated nanofibrillated cellulose as dispersant.* Rsc Advances, 2016. **6**(44): p. 37330-37336.

166. Seydibeyoglu, M.O., et al., *Review on Hybrid Reinforced Polymer Matrix Composites with Nanocellulose, Nanomaterials, and Other Fibers.* Polymers (Basel), 2023. **15**(4): p. 984.

167. Idris, A., et al., *Oxygen barrier performance of poly (vinyl alcohol) coating films with different induced crystallinity and model predictions.* Coatings, 2021. **11**(10): p. 1253.

168. Guo, T., et al., *Chitin Nanofibers Enable the Colloidal Dispersion of Carbon Nanomaterials in Aqueous Phase and Hybrid Material Coassembly.* ACS Nano, 2024. **18**(23): p. 14954-14967.

169. Nordenstrom, M., et al., *The structure of cellulose nanofibril networks at low concentrations and their stabilizing action on colloidal particles.* Carbohydr Polym, 2022. **297**: p. 120046.

170. Aguado, R.J., et al., *The role of electrostatic interactions of anionic and cationic cellulose derivatives for industrial applications: A critical review.* Industrial Crops and Products, 2023. **201**: p. 116898.

171. Lu, A., Y. Song, and Y. Boluk, *Electrolyte effect on gelation behavior of oppositely charged nanocrystalline cellulose and polyelectrolyte.* Carbohydr Polym, 2014. **114**: p. 57-64.

172. Östmans, R., et al., *Solidified water at room temperature hosting tailored fluidic channels by using highly anisotropic cellulose nanofibrils.* Materials Today Nano, 2024. **26**: p. 100476.

173. Chi, K., et al., *Electrostatically Complexed Natural Polysaccharides as Aqueous Barrier Coatings for Sustainable and Recyclable Fiber-Based Packaging.* ACS Appl Mater Interfaces, 2023. **15**(9): p. 12248-12260.

174. Chi, K., H. Wang, and J.M. Catchmark, *Sustainable starch-based barrier coatings for packaging applications.* Food Hydrocolloids, 2020. **103**: p. 105696.

175. Benselfelt, T., et al., *The Colloidal Properties of Nanocellulose.* ChemSusChem, 2023. **16**(8): p. e202201955.

176. Sebenik, U., R. Lapasin, and M. Krajnc, *Rheology of aqueous dispersions of Laponite and TEMPO-oxidized nanofibrillated cellulose.* Carbohydr Polym, 2020. **240**: p. 116330.

177. Li, H.Z., S.C. Chen, and Y.Z. Wang, *Preparation and characterization of nanocomposites of polyvinyl alcohol/cellulose nanowhiskers/chitosan.* Composites Science and Technology, 2015. **115**: p. 60-65.

178. Liu, A., L. Medina, and L.A. Berglund, *High-Strength Nanocomposite Aerogels of Ternary Composition: Poly(vinyl alcohol), Clay, and Cellulose Nanofibrils.* ACS Appl Mater Interfaces, 2017. **9**(7): p. 6453-6461.

179. Wang, J., et al., *Synergistic toughening of bioinspired poly(vinyl alcohol)-clay-nanofibrillar cellulose artificial nacre.* ACS Nano, 2014. **8**(3): p. 2739-45.

180. Mianehrow, H., et al., *Strong Reinforcement Effects in 2D Cellulose Nanofibril-Graphene Oxide (CNF-GO) Nanocomposites due to GO-Induced CNF Ordering.* J Mater Chem A Mater, 2020. **8**(34): p. 17608-17620.

181. Li, Y.Y., et al., *Hybridizing wood cellulose and graphene oxide toward high-performance fibers.* Npg Asia Materials, 2015. **7**(1): p. e150-e150.

182. Zhang, J.P., et al., *Preparation and swelling properties of pH-sensitive sodium alginate/layered double hydroxides hybrid beads for controlled release of diclofenac sodium.* Journal of Biomedical Materials Research Part B: Applied Biomaterials: An Official Journal of The Society for Biomaterials, The Japanese Society for Biomaterials, and The Australian Society for Biomaterials and the Korean Society for Biomaterials, 2010. **92**(1): p. 205-214.

183. Choi, E.H., et al., *Influence of PVA and CMC on the Properties of Pigment Coating Colors and their Effects on Curtain Stability.* Bioresources, 2015. **10**(4): p. 7188-7202.

184. Jipa, I.M., et al., *Potassium sorbate release from poly(vinyl alcohol)-bacterial cellulose films.* Chemical Papers, 2012. **66**(2): p. 138-143.

185. Peppas, N.A., *Infrared spectroscopy of semicrystalline poly(vinyl alcohol) networks.* Die Makromolekulare Chemie, 2003. **178**(2): p. 595-601.

186. Grande, R., et al., *Continuous microfiber drawing by interfacial charge complexation between anionic cellulose nanofibers and cationic chitosan.* Journal of Materials Chemistry A, 2017. **5**(25): p. 13098-13103.

187. Rosca, C., et al., *Interaction of chitosan with natural or synthetic anionic polyelectrolytes. 1. The chitosan–carboxymethylcellulose complex.* Carbohydrate polymers, 2005. **62**(1): p. 35-41.

188. Liu, A., et al., *Clay nanopaper with tough cellulose nanofiber matrix for fire retardancy and gas barrier functions.* Biomacromolecules, 2011. **12**(3): p. 633-41.

189. Vaezi, K., G. Asadpour, and S.H. Sharifi, *Bio nanocomposites based on cationic starch reinforced with montmorillonite and cellulose nanocrystals: Fundamental properties and biodegradability study.* Int J Biol Macromol, 2020. **146**: p. 374-386.

190. Almasi, H., B. Ghanbarzadeh, and A.A. Entezami, *Physicochemical properties of starch-CMC-nanoclay biodegradable films.* Int J Biol Macromol, 2010. **46**(1): p. 1-5.

191. Vaezi, K., G. Asadpour, and H. Sharifi, *Effect of ZnO nanoparticles on the mechanical, barrier and optical properties of thermoplastic cationic starch/montmorillonite biodegradable films.* Int J Biol Macromol, 2019. **124**: p. 519-529.

192. Lee, D., et al., *Structural changes of polyaniline/montmorillonite nanocomposites and their effects on physical properties.* Journal of Materials Chemistry, 2003. **13**(12): p. 2942-2947.

193. Nguyen, H.L., et al., *Biorenewable, transparent, and oxygen/moisture barrier nanocellulose/nanochitin-based coating on polypropylene for food packaging applications.* Carbohydr Polym, 2021. **271**: p. 118421.

194. Vatansever, E., D. Arslan, and M. Nofar, *Polylactide cellulose-based nanocomposites.* Int J Biol Macromol, 2019. **137**: p. 912-938.

195. LaChance, A.M., et al., *Polyolefin films with outstanding barrier properties based on one-step coassembled nanocoatings.* Advanced Composites and Hybrid Materials, 2022. **5**(2): p. 1067-1077.

196. Huang, H.D., et al., *Promising strategies and new opportunities for high barrier polymer packaging films.* Progress in Polymer Science, 2023. **144**: p. 101722.

197. Adame, D. and G.W. Beall, *Direct measurement of the constrained polymer region in polyamide/clay nanocomposites and the implications for gas diffusion.* Applied Clay Science, 2009. **42**(3-4): p. 545-552.

198. Wolf, C., et al., *How the shape of fillers affects the barrier properties of polymer/non-porous particles nanocomposites: A review.* Journal of Membrane Science, 2018. **556**: p. 393-418.

199. Li, J., et al., *Single-Step Application of Polyelectrolyte Complex Films as Oxygen Barrier Coatings.* ACS Applied Materials & Interfaces, 2021. **13**(18): p. 21844-21853.

200. Ma, H.Y., et al., *Synergistic effect of carbon nanotube and clay for improving the flame retardancy of ABS resin.* Nanotechnology, 2007. **18**(37): p. 375602.

201. Noshirvani, N., et al., *Study of cellulose nanocrystal doped starch-polyvinyl alcohol bionanocomposite films.* Int J Biol Macromol, 2018. **107**(Pt B): p. 2065-2074.

202. Ge, C., et al., *Effects of flexing, optical density, and lamination on barrier and mechanical properties of metallized films and aluminum foil centered laminates prepared with polyethylene terephthalate and linear low density polyethylene.* Journal of Plastic Film & Sheeting, 2021. **37**(2): p. 205-225.

203. Compton, O.C., et al., *Crumpled graphene nanosheets as highly effective barrier property enhancers.* Adv Mater, 2010. **22**(42): p. 4759-63.

204. Li, J.Y., et al., *Single-Step Application of Polyelectrolyte Complex Films as Oxygen Barrier Coatings.* Acs Applied Materials & Interfaces, 2021. **13**(18): p. 21844-21853.

205. Chi, K. and J.M. Catchmark, *Improved eco-friendly barrier materials based on crystalline nanocellulose/chitosan/carboxymethyl cellulose polyelectrolyte complexes.* Food Hydrocolloids, 2018. **80**: p. 195-205.

206. Jung, B.N., et al., *Synergistic Effect of Cellulose Nanofiber and Nanoclay as Distributed Phase in a Polypropylene Based Nanocomposite System.* Polymers, 2020. **12**(10): p. 2399.

207. Alexandre, B., et al., *Water barrier properties of polyamide 12/montmorillonite nanocomposite membranes: Structure and volume fraction effects.* Journal of Membrane Science, 2009. **328**(1-2): p. 186-204.

208. Chen, H.Y., et al., *In situ microstructure control of oriented layered double hydroxide monolayer films with curved hexagonal crystals as superhydrophobic materials.* Advanced Materials, 2006. **18**(23): p. 3089-+.

209. Schuman, T., et al., *Characteristics of pigment-filled polymer coatings on paperboard.* Progress in Organic Coatings, 2005. **54**(4): p. 360-371.

210. Yang, Y.H., et al., *Super Gas Barrier of All-Polymer Multilayer Thin Films.* Macromolecules, 2011. **44**(6): p. 1450-1459.

211. Allusse, G., et al. *Influence of fiber/matrix interface on gas permeability properties of CF/TP composites*. in *ECCM20-Proceedings of the 20th European Conference on Composite Materials*. 2022.

212. Priolo, M.A., D. Gamboa, and J.C. Grunlan, *Transparent Clay−Polymer Nano Brick Wall Assemblies with Tailorable Oxygen Barrier.* ACS Applied Materials & Interfaces, 2010. **2**(1): p. 312-320.

213. Nielsen, L.E., *Models for the permeability of filled polymer systems.* Journal of Macromolecular Science—Chemistry, 1967. **1**(5): p. 929-942.

214. Moggridge, G.D., et al., *Barrier films using flakes and reactive additives.* Progress in Organic Coatings, 2003. **46**(4): p. 231-240.

215. Gusev, A.A. and H.R. Lusti, *Rational design of nanocomposites for barrier applications.* Advanced Materials, 2001. **13**(21): p. 1641-+.

216. Fredrickson, G.H. and J. Bicerano, *Barrier properties of oriented disk composites.* Journal of Chemical Physics, 1999. **110**(4): p. 2181-2188.

217. Rovera, C., M. Ghaani, and S. Farris, *Nano-inspired oxygen barrier coatings for food packaging applications: An overview.* Trends in Food Science & Technology, 2020. **97**: p. 210-220.

218. Stocchetti, G., *Technology that bridges the gap.* Packaging Films, 2012. **3**(1): p. 16-18.

219. Rastogi, V.K. and P. Samyn, *Bio-based coatings for paper applications.* Coatings, 2015. **5**(4): p. 887-930.

220. Lepoutre, P., *The structure of paper coatings: an update.* Progress in Organic Coatings, 1989. **17**(2): p. 89-106.

221. Adibi, A., B.M. Trinh, and T.H. Mekonnen, *Recent progress in sustainable barrier paper coating for food packaging applications.* Progress in Organic Coatings, 2023. **181**: p. 107566.

222. Nechita, P. and M. Roman, *Review on polysaccharides used in coatings for food packaging papers.* Coatings, 2020. **10**(6): p. 566.

223. Christophliemk, H., et al., *Surface analyses of thin multiple layer barrier coatings of poly (vinyl alcohol) for paperboard.* Coatings, 2023. **13**(9): p. 1489.

224. Michelman, J. and D. Capella, *Repulpability of coated corrugated paperboard.* Tappi journal, 1991. **74**(10): p. 79-82.

225. Herrera, M.A., A.P. Mathew, and K. Oksman, *Barrier and mechanical properties of plasticized and cross-linked nanocellulose coatings for paper packaging applications.* Cellulose, 2017. **24**: p. 3969-3980.

226. Kumaki, Y., et al. *Enhanced polyvinyl alcohol as a barrier paper coating for food packaging*. in *Proceedings of the TAPPI Paper Conference and Trade Show PaperCon, Nashville, TN, USA*. 2014.

227. Vatansever, E., A. Ajji, and A. Saffar, *Electrostatically Complexed Polyvinyl Alcohol-Layered Double Hydroxides-TEMPO-Oxidized Cellulose Nanofibers Gas Barrier Coatings.* Advanced Composites and Hybrid Materials, Submitted.

228. Alves, L., et al., *Rheology of Suspensions of TEMPO-Oxidised and Cationic Cellulose Nanofibrils—The Effect of Chemical Pre-Treatment.* Gels, 2024. **10**(6): p. 367.

229. Zhou, M., et al., *Investigating the impact of cellulose microgel nanofabrication on the rheological properties of this binary rheology modifier.* International Journal of Biological Macromolecules, 2024: p. 132966.

230. Shabani, S., M. Valizadeh, and A. Khavandi, *Evaluation of the sensitivity of the rheology characteristics of bitumen and slurry seal modified with cellulose nanofiber solution.* Construction and Building Materials, 2024. **422**: p. 135318.

231. Liu, C., et al., *Properties of nanocelluloses and their application as rheology modifier in paper coating.* Industrial & Engineering Chemistry Research, 2017. **56**(29): p. 8264-8273.

232. Xu, S., et al., *Nanocellulose-assisted dispersion of graphene to fabricate poly (vinyl alcohol)/graphene nanocomposite for humidity sensing.* Composites Science and Technology, 2016. **131**: p. 67-76.

233. Seydibeyoğlu, M.Ö., et al., *Review on hybrid reinforced polymer matrix composites with nanocellulose, nanomaterials, and other fibers.* Polymers, 2023. **15**(4): p. 984.

234. Silva, C.E., J.S. Bernardes, and W. Loh, *Stabilizing both oil droplets and titanium dioxide nanoparticles in aqueous dispersion with nanofibrillated cellulose.* Carbohydrate Polymers, 2023. **302**: p. 120354.

235. Grüneberger, F., et al., *Nanofibrillated cellulose in wood coatings: mechanical properties of free composite films.* Journal of Materials Science, 2014. **49**: p. 6437-6448.

236. Li, F., et al., *Multi-functional coating of cellulose nanocrystals for flexible packaging applications.* Cellulose, 2013. **20**: p. 2491-2504.

237. Arslan, D., E. Vatansever, and M. Nofar, *Nanocellulose Polylactide-Based Composite Films for Packaging Applications.* Bio-based Packaging: Material, Environmental and Economic Aspects, 2021: p. 165-191.

238. Jin, K., et al., *Nanofibrillated cellulose as coating agent for food packaging paper.* International Journal of Biological Macromolecules, 2021. **168**: p. 331-338.

239. Youn, H.J. and H.L. Lee, *Influence of pigment and binder composition on the dynamic water penetration and dried structure of precoating layers for double-coated paper.* Journal of Coatings Technology and Research, 2022. **19**(3): p. 931-938.

240. Chi, K., et al., *Electrostatically complexed natural polysaccharides as aqueous barrier coatings for sustainable and recyclable fiber-based packaging.* ACS Applied Materials & Interfaces, 2023. **15**(9): p. 12248-12260.

241. Arbatan, T., et al., *Cellulose nanofibers as binder for fabrication of superhydrophobic paper.* Chemical engineering journal, 2012. **210**: p. 74-79.

242. Seo, M., H. Youn, and H. Lee, *Penetration control of surface sizing starch using cationic PAM and its effect on the bending stiffness of paper.* BioResources, 2020. **15**(3): p. 5489.

243. Lee, H.L., et al., *Surface sizing with cationic starch: Its effect on paper quality and papermaking process.* Tappi J, 2002. **1**(1): p. 34-40.

244. Dimic-Misic, K., et al., *The role of MFC/NFC swelling in the rheological behavior and dewatering of high consistency furnishes.* Cellulose, 2013. **20**: p. 2847-2861.

245. Chen, H., et al., *Importance of cellulosic fines relative to the dewatering rates of fiber suspensions.* Industrial & engineering chemistry research, 2009. **48**(20): p. 9106-9112.

246. Rautkoski, H., et al., *Use of cellulose nanofibrils (CNF) in coating colors.* Nordic Pulp & Paper Research Journal, 2015. **30**(3): p. 511-518.

247. Solhi, L., et al., *Understanding nanocellulose–water interactions: Turning a detriment into an asset.* Chemical reviews, 2023. **123**(5): p. 1925-2015.

248. Priolo, M.A., D. Gamboa, and J.C. Grunlan, *Transparent clay− polymer nano brick wall assemblies with tailorable oxygen barrier.* ACS Applied Materials & Interfaces, 2010. **2**(1): p. 312-320.

249. Christophliemk, H., et al., *Oxygen and water vapor transmission rates of starch-poly (vinyl alcohol) barrier coatings for flexible packaging paper.* Progress in Organic Coatings, 2017. **113**: p. 218-224.

250. Hirvikorpi, T., et al., *Atomic layer deposited aluminum oxide barrier coatings for packaging materials.* Thin Solid Films, 2010. **518**(10): p. 2654-2658.

251. Smith, B.C., *The Carbonyl Group, Part V: Carboxylates—Coming Clean.* Spectroscopy, 2018. **33**(5): p. 20–23-20–23.

252. Shi, X., et al., *Zwitterionic glycine modified Fe/Mg-layered double hydroxides for highly selective and efficient removal of oxyanions from polluted water.* Journal of Materials Science & Technology, 2020. **51**: p. 8-15.

253. Gao, Y., et al., *Surface precipitation of highly porous hydrotalcite-like film on Al from a zinc aqueous solution.* Langmuir, 2006. **22**(8): p. 3521-3527.

254. Dutta, K., S. Das, and A. Pramanik, *Concomitant synthesis of highly crystalline Zn–Al layered double hydroxide and ZnO: phase interconversion and enhanced photocatalytic activity*. Journal of colloid and interface science, 2012. **366**(1): p. 28-36.

255. Li, S., G. Zhao, and H. Chen, *Influence of pH on the Formation of Tyr/LDH Nanohybrids*. Journal of dispersion science and technology, 2005. **26**(4): p. 429-433.

256. Boclair, J.W. and P.S. Braterman, *Layered double hydroxide stability. 1. Relative stabilities of layered double hydroxides and their simple counterparts.* Chemistry of Materials, 1999. **11**(2): p. 298-302.

257. Oehman, L.O., *Equilibrium and structural studies of silicon (IV) and aluminum (III) in aqueous solution. 17. Stable and metastable complexes in the system hydrogen (+)-aluminum (3+)-citric acid*. Inorganic Chemistry, 1988. **27**(15): p. 2565-2570.

APPENDIX A SUPPORTING INFORMATION OF THE FIRST ARTICLE

1. FTIR spectra of all samples

FTIR spectra of LDHs prepared through different hydrothermal conditions shows the similar LDH features. The broad bands around 3400 cm^{-1}, with a shoulder around 3100 cm^{-1}, are attributed to the H-bonding stretching vibrations of the OH group (νOH) in the octahedral lattice, interlayer water and physically adsorbed water molecules. The peak 1360 is attributed to CO^{32}- and observed in the FTIR spectra of all LDHs, which may be due to the introduction of small amounts of CO_2 from the air after the preparation process. The sharp bands at 1624 cm^{-1} and 1615 cm^{-1} are associated with the bending vibration of the interlayer water molecules (δH−O−H). When the glycine is used for LDH synthesize, new peaks were observed at 1398 cm−1 and 1572 cm−1, symmetric and asymmetric stretching of COO– group[121, 251]. The peak 1502-15112 $^{-1}$ was symmetric deformation of NH_3^+.

1089.7 cm^{-1} and 1040.6 cm^{-1} peaks also were observed due to the change of M-O bond length caused by the insertion of glycine between layers [252]. The bands in the lower wavenumber region (<850 cm^{-1}) originate from the M-O and O-M-O (M is Mg or Al) lattice vibration modes.

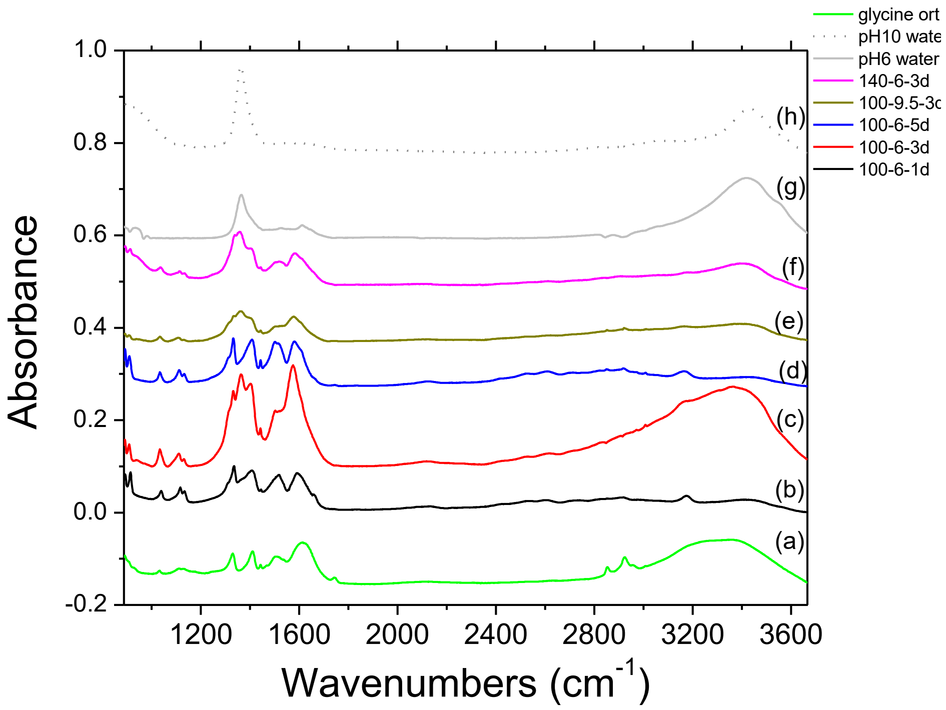

Figure S4.1 FTIR spectra: (a)glycine (b) 6_100_1d, (c) 6_100_3d, (d) 6_100_5d (e) 9.5_100_3d (f) 6_140_3d (g) 6_100_3d_W prepared using only water (no glycine) (h) 9.5_100_3d_W prepared using only water (no glycine)

2. Concentration of different species at different conditions

At pH 6, the concentration of $Mg(OH)_3^-$ is higher and nucleation and growth mostly takes place on the surface of $Mg(OH)_3^-$. At higher 9.5, the concentration of $Al(OH)_4^-$ increases within system ($Al(OH)_3 + OH- \rightleftharpoons Al(OH)_4^-$), so nucleation for LDH crystallization occur on $Al(OH)_4^-$ surface more. Moreover, a large amount of $Al(OH)_4$ may also lead to some irregularity in the LDH morphology in 100_9_3d [253-255].

Table S1: Possible Mg and Al species and their concentrations in different pH conditions

Equilibrium reac	pKsp at 25	Metal ion specie	pH 6	pH 9.5
$Mg(OH)_{2(s)} \rightleftharpoons Mg^{2+}_{(aq)} + 2OH^-_{(aq)}$	10.0 [a]	Mg^{2+}	1.0×10^{6} M	10.0 M
$Al(OH)_{3(s)} \rightleftharpoons Al^{3+}_{(aq)} + 3OH^-_{(aq)}$	31.2 [b]	Al^{3+}	1.0×10^{-6} M	1.08×10^{-8}M
$Al(OH)_{3(s)} + OH^- \rightleftharpoons Al(OH)_4^-$	1.3 [b]	$Al(OH)_4$	8.16×10^{-9} M	1.06×10^{-4} M

a K_{sp} data of fresh $Mg(OH)_2$ and $Al(OH)_3$ were from ref [256]. b The original hydration constants of Al^{3+} were from ref [257]

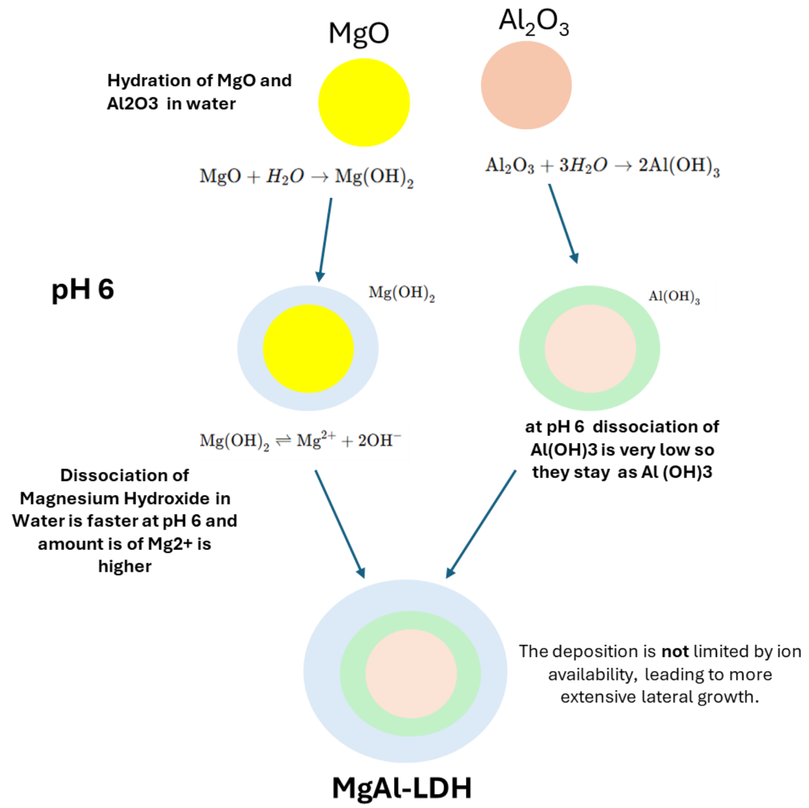

Figure S4.2 LDH hydration, dissociation, deposition mechanism at pH 6, which leads to larger diameter

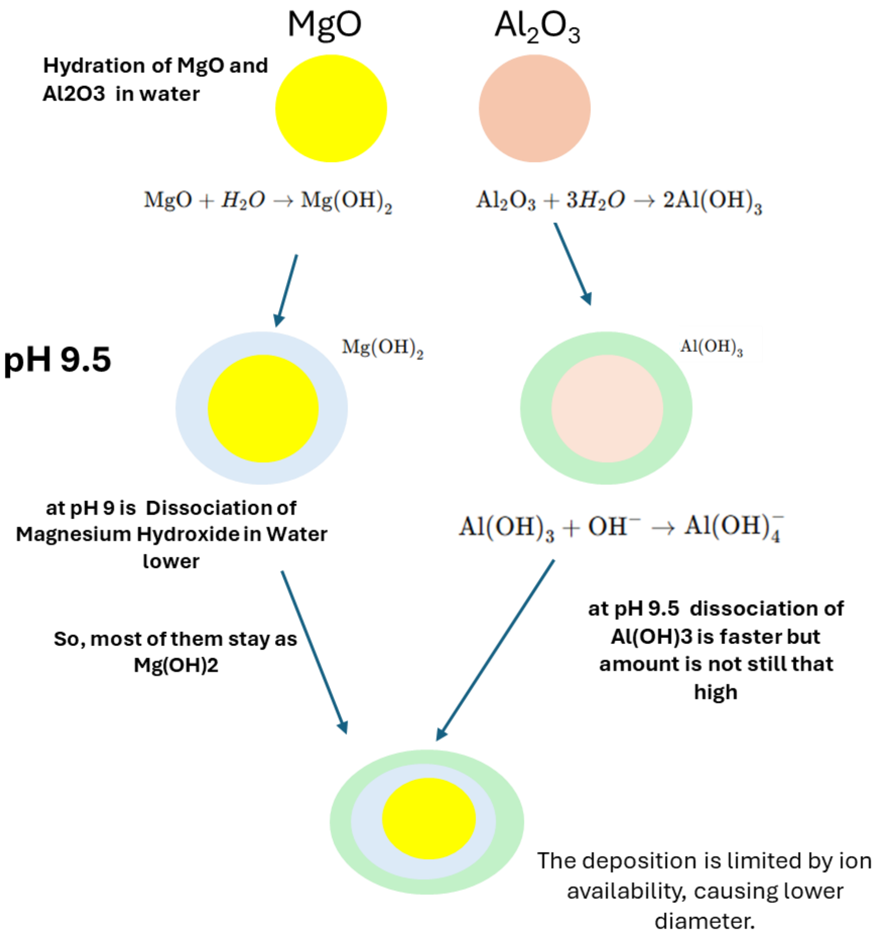

Figure S4.3 LDH hydration, dissociation, deposition mechanism at pH 9.5 which leads to larger diameter

3. XRD graphs and crystal size of LDH sample

Table S4.2: FWHM and uncertainty values of LDHs prepared through different conditions.

Sample	**FWHM**[a] [°]	**Uncertainty FWHM**	**Crystallite size in c axis**[b] **(nm)**
100-9.5-3d	0.62449	0.00385	13.8
100-6-3d	0.63489	0.00451	12.7
140-6-3d	1.06164	0.01149	11.8
100-6-5d	0.95094	0.01563	9.1
100-6-1d	0.423	0.0115	18.8

a Full width half maximum from (003) reflection. **b** Estimation of crystallite sizes calculated from Scherrer equation (Eq. (2)) FWHM values and uncertainty given in Table S2

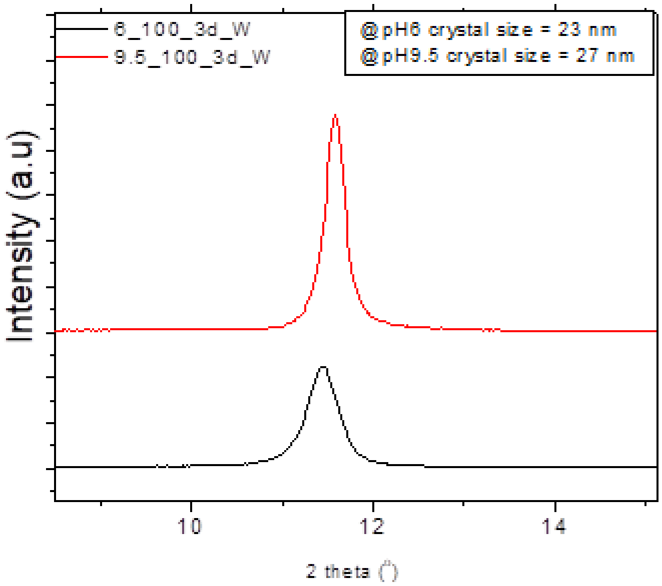

Figure S4.4: XRD graphs of LDHs prepared through only water at two different pH level.

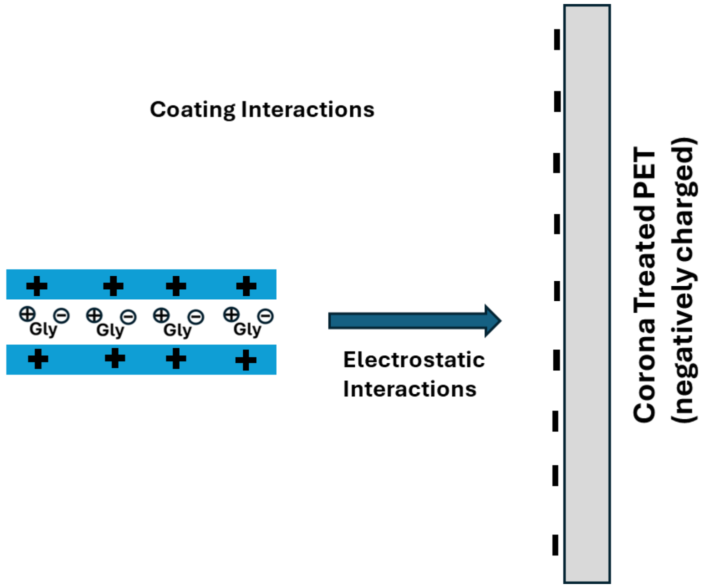

Figure S4.5: Positively charged LDH and electrostatic interactions with negatively charged corona treated PET

APPENDIX B SUPPORTING INFORMATION OF SECOND ARTICLE

Table S1: Coating formulations, zeta potential and hydrodynamic size

Coating formulation	PVA (wt%)	TCNF (wt%)	LDH (wt%)	DI water (wt%)	Zeta Potential (mV)	Hydrodynamic size (nm)
PVA	5	-	-	95	+18	369
PVA/TCNF	4	1	-	95	+3.1	1049
PVA/LDH	4	-	1	95	+18.9	920
PVA/LDH-TCNF	4	0.5	0.5	95	+9.8	1670

Table S2 Surface charge and sizes of LDH and TCNF

Sample	Hydrodynamic size DLS (nm)	Zeta potential (mV)	Diameter or length TEM (nm)	Diameter/Thickness AFM (nm)	Aspect ratio AFM
LDH	517 ± 4	+35	232 ± 71	238 ± 63 / 1.8 ± 0.6	132 ± 35
TCNF	670 ± 330	-49	252 ± 68	-	62.7

Table S3 Coating thicknesses measured through different approaches

Coating formulation	OTR (cc/m2 day)	Coating weight (g/m2)	Total thickness from coating weight (µm)	Total thickness micrometer (µm)	Total thickness SEM (µm)
PET	128 ± 1	-	13	12.8 ± 0.5	13.1 ± 0.3
PET/PVA	0.6 ± 0.15	4 ± 0.1	16.3	14.7 ± 0.4	16.8 ± 0.7
PET/PVA4-TCNF1	0.43± 0.08	3.3 ± 0.1	15.3	14.4 ± 0.3	15.6 ± 1.2
PET/PVA4-LDH1	0.12 ± 0.07	3.4 ± 0.3	15.5	13.7 ± 0.8	14.5 ± 1
PET/PVA4-LDH0.5_TCNF0.5	0.04 ± 0.034	4 ± 0.1	15.8	14.6 ± 0.3	14.4 ± 0.9

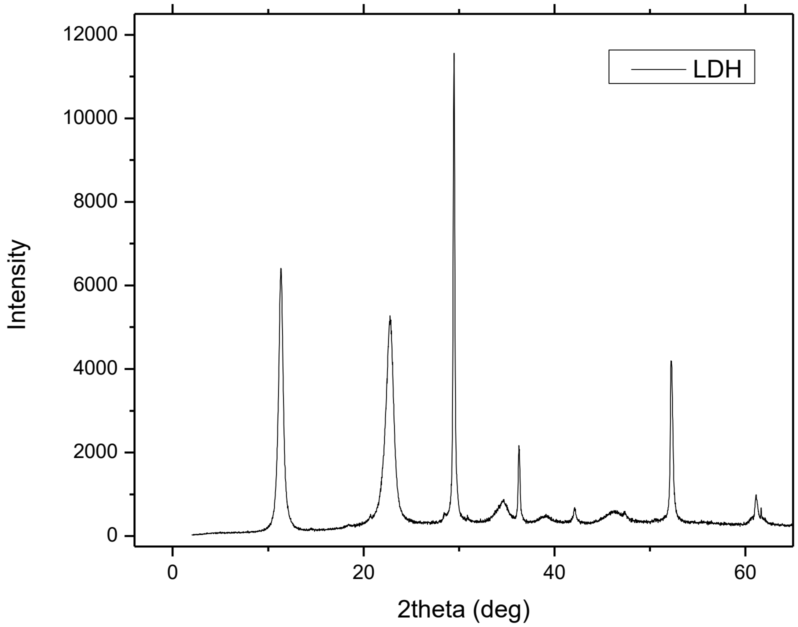

Figure S5.1: XRD graph of high aspect ratio LDH synthesized through calcination-rehydration method

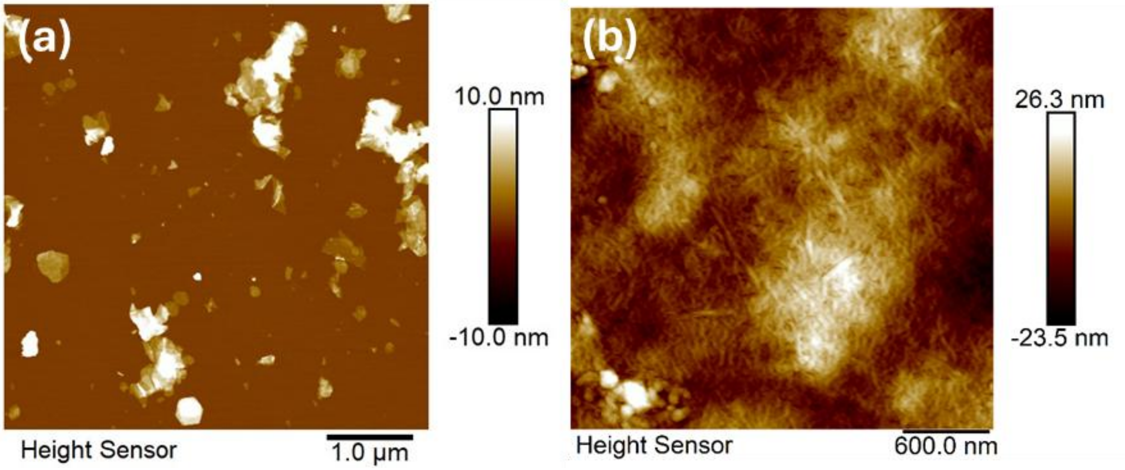

Figure S2: AFM graphs of (a) LDH (scale bar 1 µm) and (b) TCNF (scale bar 600 nm)

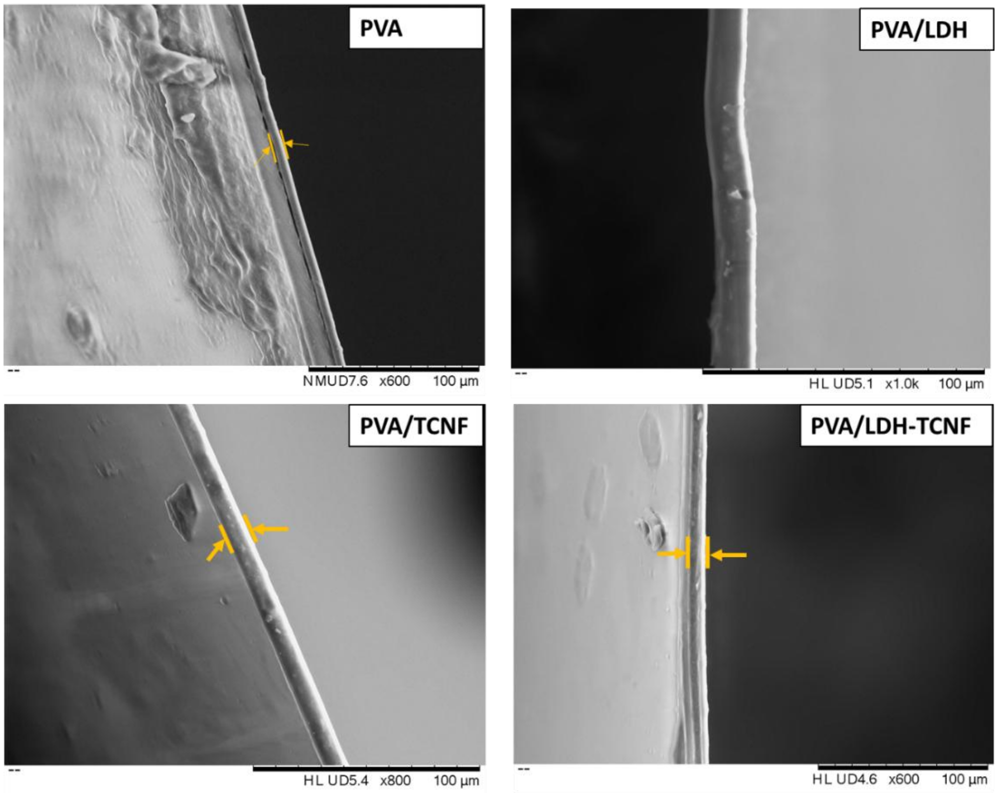

Figure S5.3: Cross section analysis of PVA, PVA/LDH, PVA/TCNF, PVA/LDH-TCNF coatings on PET through SEM (scale bar 100 µm)

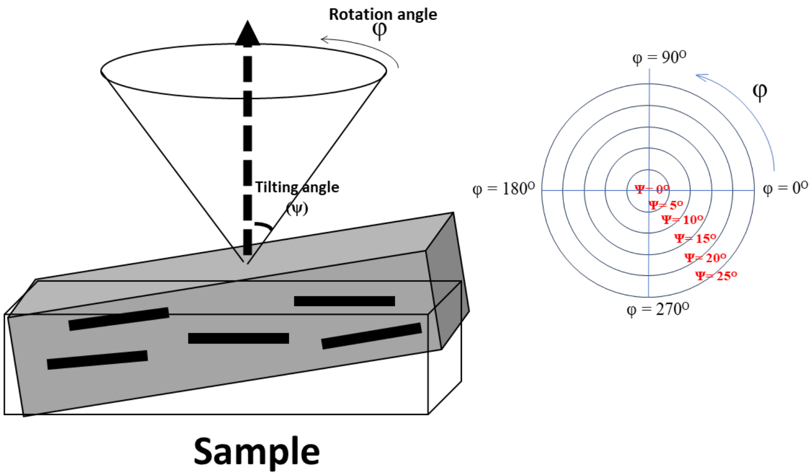

Figure S5.4: Illustration of pole figure measurements: Tilt and rotation angle

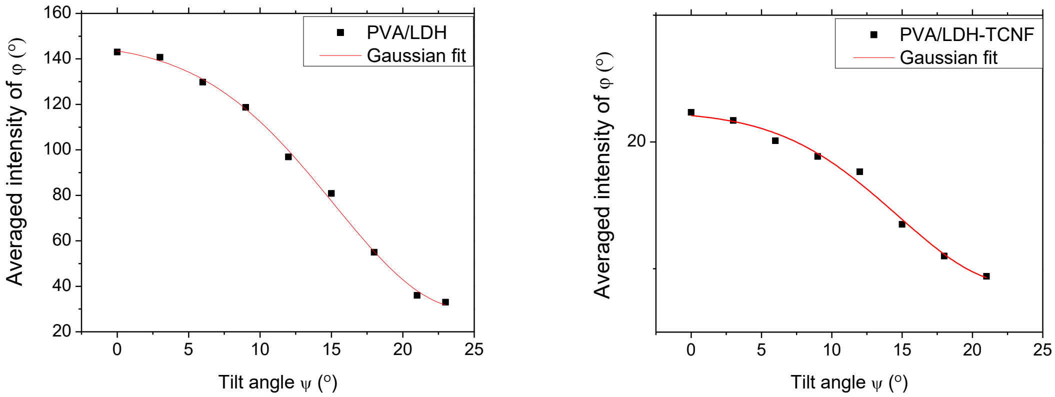

Figure S5.5: FWHM analysis of pole figure measurements, orientation distribution calculated using equation 2

Effective aspect ratio of LDH-TCNF (Aeff):

$$A_{eff} = \frac{\frac{m_{LDH}}{\rho_{LDH}} A_{LDH} + \frac{m_{TCNF}}{\rho_{TCNF}} A_{TCNF}}{\frac{m_{LDH}}{\rho_{LDH}} + \frac{m_{TCNF}}{\rho_{TCNF}}}$$

Where m_{LDH} , ρ_{LDH} , m_{PVA} , ρ_{PVA} , m_{TCNF}, ρ_{TCNF} are weight fraction and density of LDH, PVA, TCNF respectively. The density values are 2.06, 1.27, 1.4 g/cm3 for LDH, PVA, TCNF, respectively. A_{LDH} and A_{TCNF} are aspect ratios of LDH and TCNF measured through AFM or TEM. The effective aspect ratio was calculated as 89.6.

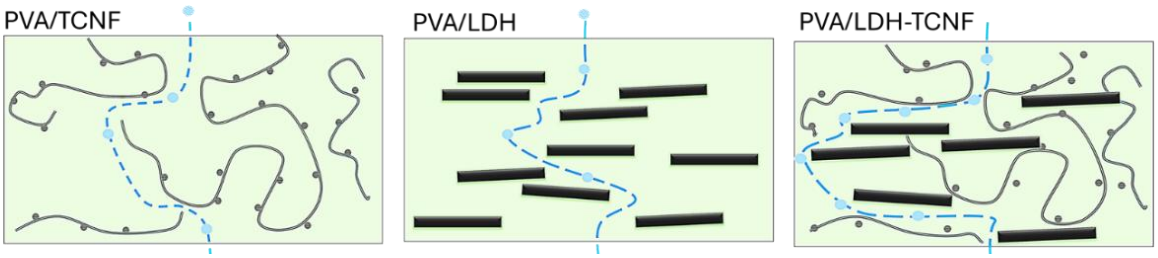

Figure S5.6: Permeability in PVA/TCNF and PVA/LDH is reduced through mostly tortuosity effect of nanoparticles. In PVA/LDH-CNF tortuosity effect is maximized with network among PVA/LDH-CNF, moreover, modification of microstructure, segmental mobility and nanoparticle state may further reduce the oxygen permeability. Higher number of oxygen molecules (blue spherical in the illustration) indicates slower oxygen diffusion due to the (I) and (II). For sake of simplicity, green background in graphs considered as PVA matrix.

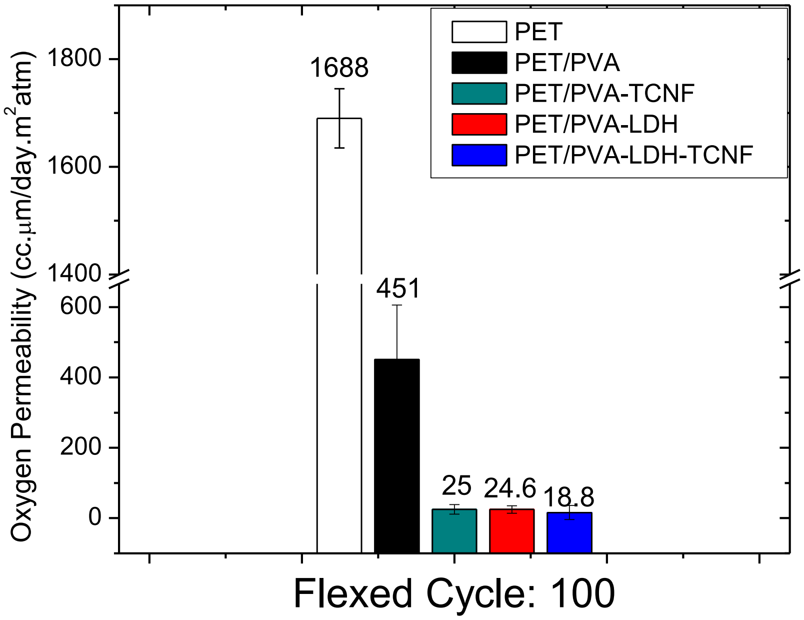

Figure S5.7: Oxygen Permeability of coating before and after flex 100 times.